

Motion manipulation and broadband microwave
spectroscopic studies of molecules with a large
dipole moment.

Dissertation zur Erlangung des Doktorgrades
des Fachbereichs Chemie der Universität Hamburg

Angefertigt am Max-Planck-Institut für
Struktur und Dynamik der Materie
und
Deutsches Elektronen-Synchrotron
Ein Forschungszentrum der Helmholtz-Gemeinschaft
Hamburg

Jack B. Graneek

August 1, 2018

Gutachter der Dissertation:

Prof. Dr. Melanie Schnell

Prof. Dr. Horst Weller

Gutachter der Disputation:

Prof. Dr. Alf Mews

Prof. Dr. Michael Fröba

Prof. Dr. Melanie Schnell

Vorsitzender des Prüfungsausschusses:

Prof. Dr. Alf Mews

Datum der Disputation:

01.06.2018

Friegabe der Dissertation zur Veröffentlichung:

01.06.2018

Publications

1. T. Betz, S. Zinn, J. B. Graneek, and M. Schnell, *Nuclear quadrupole coupling constants of two chemically distinct nitrogen atoms in 4-aminobenzonitrile*, J. Phys. Chem. A. **118**, 5164–5169 (2014).
2. J. B. Graneek, S. Merz, D. Patterson, T. Betz, and M. Schnell, *Simulating spatial microwave manipulation of polyatomic asymmetric-top molecules using a multi-level approach*, ChemPhysChem. **17**, 3624-3630 (2016).
3. J. B. Graneek, C. Pérez, and M. Schnell, *Structural determination and population transfer of 4-nitroanisole by broadband microwave spectroscopy and tailored microwave pulses*, J. Chem. Phys. **147**, 154306 (2017).
4. J. B. Graneek, W. C. Bailey and M. Schnell, *Electron-withdrawing effects on the molecular structure of 2- and 3-nitrobenzonitrile revealed by broadband rotational spectroscopy and their comparison with 4-nitrobenzonitrile*, submitted to Physical Chemistry Chemical Physics.

Abstract

Inspired by the progress made in the development of atom cooling methods, the development of methods for the production of cold molecules offers interesting prospects for future precision and collision experiments. There are several well established approaches, such as laser cooling, Stark and Zeeman deceleration, and buffer-gas cooling, all of which have been employed to produce cold samples for a variety of molecules. For the techniques that utilize an external field (electric, magnetic, or electromagnetic), an extensive knowledge of the molecule under investigation is required, especially as the application of such techniques is generally limited by the size and complexity of the molecule.

Polyatomic, asymmetric molecules generally display a high density of rotational states relative to smaller molecules with higher symmetry. For more complex molecular systems, most rotational states are high-field-seeking at large electric field strengths and are consequently inaccessible to methods such as Stark deceleration. A detailed knowledge of a molecule's energy level structure, which will be provided as part of this thesis, is essential to establish the feasibility of applying techniques that utilise external fields to focus, guide and/or decelerate large polar molecules.

With the use of cylindrically symmetric microwave resonators, tailored microwave fields with true 3D field maxima in free space can be used to manipulate the motion of molecules in high-field-seeking states. To extend microwave manipulation techniques to more complex asymmetric-top molecules, potential candidates (4-aminobenzonitrile, 4-nitroanisole, 2- and 3-nitrobenzonitrile) are thoroughly investigated using chirped-pulse Fourier transform microwave (CP-FTMW) spectroscopy. The high resolution and sensitivity provided by this spectroscopic technique facilitates the determination of molecular structure and provides detailed

information on the rotational energy level structure.

Information obtained using CP-FTMW spectroscopy is incorporated into a numerical approach developed to determine the AC-Stark shifts of molecular rotational energy levels. Simulations use the results of this numerical approach, applied to 4-aminobenzonitrile, to explore the feasibility of extending microwave manipulation techniques to more complex systems. The focusing and guiding of 4-aminobenzonitrile in a high-field-seeking state requires large input powers and/or an already pre-decelerated molecular packet. To acquire a pre-decelerated packet, the possibility of applying the Stark decelerator to a selected rotational state that is still low-field-seeking at relatively large electric field strengths is also investigated using an altered numerical approach and further simulations.

A common issue that arises when decelerating and trapping molecules of a specific rotational state is losses via non-adiabatic transitions. Such losses are difficult to avoid entirely, but by targeting highly populated states losses become less detrimental. Thus, the potential of increasing the population in a rotational state of interest with tailored microwave pulses is investigated. This would be beneficial for most of the manipulation techniques mentioned earlier, especially when they are applied to more complex molecules.

Zusammenfassung

Inspiziert von dem rasant fortschreitenden Gebiet kalten der Atome birgt das Feld der kalten Moleküle interessante Perspektiven zur Entwicklung neuartiger Präzisions- und Stoßexperimente. Einige Methoden, wie zum Beispiel die Laserkühlung oder Stark- oder Zeeman-Abbremsung, konnten bereits erfolgreich auf verschiedene Moleküle angewendet werden. Bei Techniken, die ein externes Feld (elektrisch, magnetisch oder elektromagnetisch) verwenden, ist ein fundamentales Verständnis des untersuchten Moleküls wichtig, besonders da die Anwendbarkeit einer solchen Technik im Allgemeinen durch die Größe und Komplexität der verwendeten Moleküle eingeschränkt ist.

Polyatomare, asymmetrische Moleküle haben generell eine höhere Dichte an Rotationszuständen im Vergleich zu kleineren Molekülen mit hoher Symmetrie. Für komplexere Moleküle sind die meisten Rotationsniveaus bei hoher elektrischer Feldstärke hochfeldsuchend und damit unzugänglich für Methoden wie die Stark-Abbremsung. Ein fundamentales Verständnis der Energieniveaustuktur eines Moleküls, welches im Rahmen anhand dieser Arbeit möglicher Molekül-Kandidaten wird, ist essentiell um die Anwendbarkeit einer Technik, die externe Felder zum Fokussieren, Leiten und/oder Abbremsen von großen polaren Molekülen verwendet, zu untersuchen.

Mit Hilfe zylindersymmetrischer Hohlraumresonatoren können Mikrowellenfelder mit stabilen 3D Feldmaxima im freien Raum generiert werden, welche die Bewegung polarer Moleküle in hochfeldsuchenden Zuständen manipulieren können. Um die Mikrowellenmanipulationstechnik auf komplexere Moleküle (und hier insbesondere asymmetrische Kreisel) erweitern zu können, werden potentielle Kandidaten (4-Aminobenzonitril, 4-Nitroanisol, 2- und 3-Nitrobenzonitril) detailliert mittels *Chirp*-Puls Fourier-transformations-Mikrowellenspektroskopie

(CP-FTMW) untersucht. Die hohe Auflösung und Empfindlichkeit dieser spektroskopischen Methode liefert zudem detaillierte Informationen zu den Rotationsenergieniveaus und ermöglicht die präzise Bestimmung der Molekülstrukturen.

Die mittels CP-FTMW Spektroskopie erhaltenen Informationen werden in einen im Rahmen dieser Arbeit entwickelten numerischen Ansatz eingefügt, der entwickelt wurde um die AC-Stark-Verschiebungen von molekularen Rotationsenergieniveaus zu bestimmen. Die Ergebnisse dieses numerischen Ansatzes werden verwendet, um zu untersuchen, ob die Erweiterung von Mikrowellenmanipulationstechniken auf komplexere Moleküle machbar ist. Dieses wird beispielhaft für 4-Aminobenzonitril durchgeführt. Hieraus folgt, dass Fokussieren und Leiten von 4-Aminobenzonitril in einem hochfeldsuchenden Zustand hohe Eingangsleistungen erfordern und/oder ein bereits abgebremstes Molekülpaket. Um ein abgebremstes Molekülpaket zu erhalten, wird die Möglichkeit untersucht mittels des Stark-Effekts Rotationszustände auszuwählen, die bei relativ hohen elektrischen Feldstärken noch tieffeldsuchend sind. Hierfür werden ein zusätzlicher numerischer Ansatz und weitere Simulationen verwendet.

Ein allgemeines Problem, dass beim Abbremsen und Fangen von Molekülen in bestimmten Rotationsniveaus auftritt, ist der Verlust durch nicht-adiabatische Übergänge. Solche Verluste sind nur schwerig zu vermeiden, aber durch die Auswahl von hochbesetzten Niveaus verlieren sie an Einfluss. Deshalb wird hier untersucht, wie die Besetzung der zu untersuchenden Niveaus mit Mikrowellenpulsen erhöht werden können. Dies wäre für die meisten der vorab beschriebenen Manipulationstechniken von Vorteil, besonders bei der Anwendung auf komplexere Moleküle.

List of abbreviations

4-ABN	4-aminobenzonitrile
AG	Alternating-gradient
AWG	Arbitrary waveform generator
BEC	Bose-Einstein condensate
BN	Benzonitrile
CP-FTMW	Chirped-pulse Fourier transform microwave
DCM	4-Dicyanomethylene-2-methyl-6-p-dimethylaminostyryl-4H-pyran
DMA	Dimethylaniline
DMABN	Dimethylaminobenzonitrile
FID	Free induction decay
FTMW	Fourier transform microwave
FWHM	Full width half maximum
LFP	Linear fast passage
LIF	Laser-induced fluorescence
LNA	Low-noise amplifier
MCP	Micro channel plate
NBN	Nitrobenzonitrile
REMPI	Resonance enhanced multi-photon ionization
RAP	Rapid adiabatic passage
SERS	Surface-enhanced Raman spectroscopy
TE	Transverse electric
TEM	Transverse electromagnetic
TM	Transverse magnetic
TOF	Time-of-flight
TWT	Travelling wave tube

Contents

Abstract	vi
Zusammenfassung	viii
1 Introduction	1
1.1 Cold polar molecules	4
1.2 Cooling techniques	5
1.2.1 Laser cooling	6
1.2.2 Buffer-gas cooling	6
1.2.3 Molecular beams	7
1.2.4 Beam manipulation	10
1.3 Traps for neutral molecules	15
2 Theoretical background of rotational spectroscopy	17
2.1 Rotational Hamiltonian	18
2.1.1 Linear molecules	22
2.1.2 Spherical-top molecules	22
2.1.3 Symmetric-top molecules	22
2.1.4 Asymmetric-top molecules	23
2.1.5 Centrifugal distortion	26
2.2 Nuclear quadrupole splitting	26
2.3 Spectrum analysis and fitting	27
3 Experimental details	29
3.1 Motion manipulation experiments	29

3.1.1	Stark decelerator	31
3.1.2	Microwave resonators	38
3.1.3	Detection	48
3.2	Chirped-pulse Fourier transform microwave spectrometer	51
3.2.1	Methods for structural determination	53
4	Aminobenzonitrile	55
4.1	Structural determination of 4-aminobenzonitrile	56
4.1.1	Experimental	56
4.1.2	Results and discussion	57
4.2	Motion manipulation	66
4.2.1	Numerical approach	67
4.2.2	Microwave manipulation simulations	71
4.2.3	Application of Stark decelerator	77
4.3	Conclusions	81
5	Nitroanisole	85
5.1	Structure determination of 4-nitroanisole	86
5.1.1	Experimental details	87
5.1.2	Results and discussion	87
5.2	Population transfer experiments	100
5.2.1	Experimental details	101
5.2.2	Results and discussion	104
5.3	Conclusions	107
6	Nitrobenzonitrile	109
6.1	Experimental details	110
6.2	Results and discussion	111
6.3	Conclusions	128
7	Summary and Outlook	131
	Bibliography	135
	Acknowledgements	158



Chapter 1

Introduction

To better understand the physical and chemical properties of a molecule a detailed knowledge of its structure and internal dynamics is essential. Rotational spectroscopy has proven to be an effective tool in the determination of molecular structure since its development in the 1940s [1]. As a technique, rotational spectroscopy is only applicable to gas-phase molecular samples with a permanent electric dipole moment. Microwave spectroscopy was born from the progress made in the development of radio detection and ranging equipment during World War II. The first molecule to be thoroughly investigated with this technique was ammonia [2–4]. Ammonia displayed two interesting spectroscopic phenomena in the form of inversion splitting and hyperfine structure due to the nuclear quadrupole moment of the nitrogen atom. Further research on ammonia resulted in the development of the MASER (microwave amplification by stimulated emission) [5, 6], the first experimental demonstration of stimulated emission. This achievement was recognized with a Nobel Prize in physics, awarded to Townes, Basov and Prokhorov in 1964.

Microwave spectrometers have advanced in several ways since the 1940s. New molecular sources and broadband techniques have increased the range and complexity of molecules that are accessible to microwave spectroscopy. Balle and Flygare combined the supersonic expansion technique with emission spectroscopy in the time domain to overcome the negative effects of pressure broadening and low population densities observed in gas-cell spectroscopy [7]. This experimental

set-up was improved further by Grabow et al. introducing a coaxial arrangement of the molecular beam and the microwave field [8]. With the development of laser ablation sources [9], large molecules, such as monosaccharides [10] and amino acids [11, 12], could also be brought into the gas-phase and probed via microwave spectroscopy. Another innovation in the field was made in the Pate group with the development of the chirped pulsed microwave technique [13]. The application of a chirped-pulse allows for the measurement of a broadband microwave spectrum over a range of several GHz in a single chirp, rather than in small steps of only a few MHz using the former cavity-based spectrometers.

Rotational constants obtained from a microwave spectrum relate directly to the structure of a molecule as they only depend upon the molecule's moments of inertia. The increased sensitivity and resolution offered by current chirped-pulse Fourier transform microwave spectrometers enables the observation of singly substituted heavy atom isotopologues in their natural abundance. With this information an experimental molecular structure can be determined via Kraitchman's equations [14] or a least-squares fit approach. In addition to the experimental structure, a microwave spectrum provides detailed information on the rotational energy level structure and the connectivity of these levels. This is particularly advantageous for the motion manipulation experiments discussed throughout this thesis.

Microwave spectroscopic techniques are continually being improved. The advancement of digital electronics has facilitated this. For example, the 'fast frame' approach [15], an option made available by a digital oscilloscope, has been utilised to decrease measuring time as well as sample consumption. Efforts are also being made to combine a microwave spectrometer with a buffer-gas cooled molecular beam source [16], which produces cold and slow molecular samples [17]. Generally, the production of cold samples would be extremely beneficial for high-resolution spectroscopy experiments [18, 19]. Longer interaction times, resulting in an improved resolution, could lead to the observation of energy differences between enantiomers of chiral molecules [20]. This is just one example of why the field of cold molecules has received much attention over the last decades.

The cooling of atoms has led to several major advances in atomic physics. By cooling into the Kelvin regime phenomena such as superconductivity [21] and su-

perfluidity [22] were observed in the early 20th century, each being recognized with a Nobel prize. With the development of laser cooling in the 1980s it was possible to cool atoms into the millikelvin regime. Magnetic trapping and evaporative cooling allowed for further cooling still, and the observation of the Bose-Einstein condensate (BEC) [23, 24]. BECs were actually predicted by Satyendranath Bose and Albert Einstein [25] a total of 71 years before they were achieved experimentally. It was only with the continual development and improvement of cooling techniques that it was possible to take this step.

The progress that has been made in the development of atom cooling methods led to the pursuit of methods suitable for cooling molecules [26]. Molecules are generally more complex than atoms as they possess additional internal degrees of freedom and in most cases electric dipole moments. Atomic species have a total of three degrees of freedom found in three dimensional (x, y, and z) translation space. A molecule made up of N number of atoms has $3N$ degrees of freedom, which are distributed over translation, rotation and vibration. The distribution varies depending on whether the molecule is linear or not. There are two rotational and $3N - 5$ vibrational degrees of freedom for a linear molecule, rather than three rotational and $3N - 6$ vibrational degrees of freedom for a non linear molecule. In thermal equilibrium, the average energy of a molecular sample is distributed equally over all the degrees of freedom.

For molecules in the gas phase the translation temperature of a sample is characterised by the velocity distribution within that sample. Narrow velocity distributions are associated with low temperatures, whereas broad distributions are associated with higher temperatures via the Maxwell-Boltzmann equation, refer to Fig. 1.1. For example, ammonia ($^{14}\text{NH}_3$) has a mass of 17 u and at a temperature of 10 mK the full width half maximum (FWHM) of the velocity distribution is approximately 4 m/s. At room temperature (294 K) the FWHM increases to approximately 540 m/s. The temperature relates to the molecular velocity by the Maxwell-Boltzmann distribution;

$$P(\nu) = 4\pi \left(\frac{m}{2\pi k_B T} \right)^{3/2} \nu^2 e^{-\frac{m\nu^2}{2k_B T}} \quad (1.1)$$

where $P(\nu)$ is the velocity probability, m the mass of the molecule, and the Boltz-

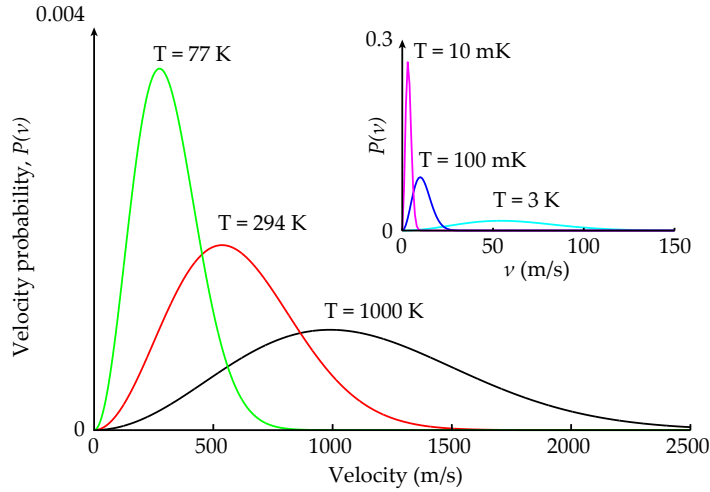


Figure 1.1: Velocity distribution for a molecule with mass 17 u (like ammonia) at varying temperatures. Inset highlights the difference in velocity distribution within the millikelvin regime.

mann constant $k_B = 1.381 \times 10^{-23} \text{ m}^2\text{kg s}^{-2}\text{K}^{-1}$. The reduction of a molecular sample's velocity distribution is essentially equivalent to reducing the sample's translation temperature.

1.1 Cold polar molecules

Potential applications of cold molecules are numerous and cover a variety of areas in both physics and chemistry. Cold molecules are being used to investigate the existence of the electron's electric dipole moment [27–29] and even parity-violating nuclear moments [30, 31]. As mentioned earlier the application of cold molecules would also be beneficial in high-resolution spectroscopy [18, 19], increasing the chance to observe potential energy differences between the enantiomers of chiral molecules [20]. Studies of chemistry at ultracold temperatures [32, 33] or within interstellar clouds [34, 35] also provide exciting possibilities for the field of cold molecules.

Of particular relevance to this thesis is the study of cold polar molecules. Polar molecules aligned in modest external fields (~ 10 kV/cm) can generate large internal electric fields (~ 100 GV/cm), which provides conditions for the observation of

potential spectroscopic signatures of a non-vanishing electric dipole moment of an electron [36, 37]. To gain insight into dynamical processes of chemical reactions, state-controlled reactions of polar molecules at ultracold temperatures have also been studied [32]. In this regime, particles are usually represented by their de Broglie wavelength, which increases at reduced temperatures. Additionally, dipole-dipole interactions and a large manifold of internal states make cold polar molecules interesting from a quantum simulation standpoint [38]. Molecules offer a rich internal landscape of many states with individual properties. For example, the electric dipole moment of some molecules can actually be tuned according to the vibrational level [39]. This is of particular interest for studies that aim to use polar molecules as part of a quantum computer [40].

In order to take full advantage of the range of applications available, there is still much progress that needs to be made in the experimental study of these systems. Chirped-pulse Fourier transform microwave spectroscopy provides a route to begin mapping the rotational energy level landscape of a polar molecule and also determine structure. From the determined molecular structure, information can be gained on the influence of certain substituents on the electronic distribution across a molecule, which directly impacts upon the molecular dipole moment and thus upon dipole-dipole interactions at ultracold temperatures. Knowledge of the rotational energy level structure for a polar molecule is especially helpful when attempting to apply manipulation techniques that rely on the Stark or Zeeman effect (see Section 4.2). These effects are quantum effects and thus rely on the molecular energy level structure. One of the aims of this thesis is to provide more information on such systems to better characterise them as a prerequisite for deceleration and trapping techniques.

1.2 Cooling techniques

As previously discussed, there are a number of areas in research that would benefit from the improvement of current techniques used to cool, trap, and manipulate polar molecules. In the following section, a selection of the techniques used to achieve such control are described in more detail, with particular focus on the methods used to manipulate a molecular beam.

1.2.1 Laser cooling

The most common method for cooling atoms to ultracold temperatures (≤ 1 mK) is laser cooling. Deceleration of sodium atoms in an atomic beam [41] was one of the earliest laser cooling experiments. Such experiments require an exchange of momentum between an atom and an optical field at a certain frequency, usually a frequency that is slightly detuned from atomic resonance in order to account for Doppler shifts. Absorption of well directed light from a laser beam forces an atom into its excited state. Using low light intensities, this atom is more likely to return to the ground state via spontaneous emission rather than stimulated emission. As fluorescence occurs momentum is carried off in a random direction, which means the net momentum transfer is equal to zero and the net force is in the direction of the laser beam. High light intensities increase the rate of absorption and are actually necessary to achieve the maximum deceleration of atoms. However, high light intensities also increase the potential of stimulated emission. Stimulated emission of a photon does not occur in a random direction, instead momentum transferred to the atom via this process is in the opposite direction of the momentum transferred during absorption. This limits the force and the deceleration saturates.

The application of laser cooling to molecules, although it has been achieved in a few rare cases [42, 43], is significantly more complicated than its application to atoms. Generally, the complex molecular energy level structure is what limits this application. Typically a molecule would scatter only a few photons before being pumped into an internal state that can no longer be addressed by the laser. Most techniques discussed within this thesis, when applicable to atoms, suffer complications when applied to molecules instead. However, considering the potential applications of cold molecules, there are still continuing efforts being made to gain more control over the internal and motional degrees of freedom for molecules.

1.2.2 Buffer-gas cooling

Buffer-gas cooling can be used to generate cold, high flux atomic and molecular beams for a variety of species including non polar molecules [44–47]. The buffer gas beam method has a fundamentally different approach to supersonic expansion.

Depending upon the size of the species and the gas that it is seeded with, supersonic expansion generates beams with forward velocities in the laboratory frame that fall between 300 and 1000 m/s (refer to Figure 1.1). In many cases buffer gas beams [17] can improve on this, producing cold and comparatively slow atoms or molecules combined with a high brightness and a large versatility.

To start, molecules or atoms typically at room temperature, normally the species of interest, are mixed with a cold inert gas within a cold cell with dimensions of typically a few centimetres. Cryogenic cells can be cooled by liquid helium evaporation or a closed-cycle pulse tube cooler. The cold, inert gas, the so-called buffer gas, is usually 2-20 K. Potential buffer gases include neon or helium. Buffer-gas cooling relies on the species of interest undergoing elastic collisions with the cold buffer gas atoms. The number density of the buffer gas is an important consideration and is often tuned so that it ranges from $10^{14} - 10^{17} \text{ cm}^{-3}$. Such a large atom number density ensures that enough collisions occur with the species of interest to allow for thermalization before contact with the cell walls, but it is also balanced to prevent cluster formation via three body collision.

A combination of properties, such as a helium-molecule elastic cross section of 10^{-14} cm^2 and a sufficient vapour pressure at temperatures as low as a few hundred millikelvin, allow for the realisation of cold cells of a few cubic centimetres when using helium as a buffer gas [44]. A cold molecular beam can then be formed when the gas mixture escapes the cold cell through an orifice of a few millimetres. Molecules as large as Nile Red ($\text{C}_{20}\text{H}_{18}\text{N}_2\text{O}_2$) were successfully cooled this way in a 7K buffer-gas cell [48].

1.2.3 Molecular beams

By expanding a gas through a small orifice from a high-pressure container into an evacuated chamber a molecular beam is formed, refer to Figure 1.2. The type of beam generated by this process depends upon the pressure within the container and the diameter of the orifice. If the size of this opening is much smaller than the mean free path of the gas (mean distance travelled before successive collisions), molecules will escape the container without undergoing collisions. This case results in an effusive beam. The velocity distribution $P(\nu)$ of the effusive beam then follows

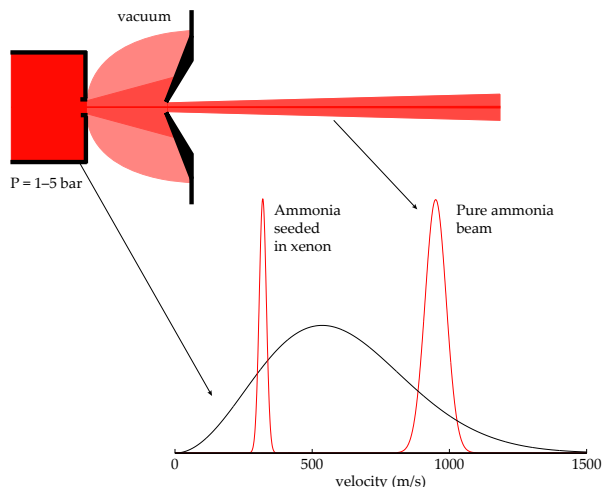


Figure 1.2: Schematic view of a supersonic expansion. The plot compares the velocity distribution for pure ammonia within the container at room temperature and in the supersonic beam. Also plotted is the velocity distribution of a supersonic beam of ammonia seeded with a xenon carrier gas. Figure has been adapted from a similar figure given in Reference [50].

the Maxwell-Boltzmann distribution of the gas within the container (Eq. 1.1).

Increasing the pressure in the container so that the mean free path of the gas is smaller than the orifice results in a supersonic beam. Cooling of the external and internal degrees of freedom within the supersonic regime occurs as the beam expands into the vacuum. The molecules undergo many collisions near the aperture and consequently receive a momentum kick primarily in the forward direction. Adiabatic cooling of all the degrees of freedom occurs as the molecules expand into the vacuum chamber. A gain in forward velocity is a result of the total energy per molecule being converted into kinetic energy. This leads to supersonic beams of internally cold molecules [49]. Depending upon the number of collisions that occur near the aperture, translational temperatures on the millikelvin scale are achievable.

Supersonic expansion is mainly used to generate rotationally and vibrationally cooled samples. Although the cooling efficiency of vibrations is highly dependent upon the vibrational mode structure. For example, polyatomic molecules exhibit more low lying vibrational modes than a diatomic molecule making colli-

sional cooling more effective. A pulsed mode can be used to generate beams with translational temperatures below 1 K at densities of 10^{13} molecules per cm^3 . The rotational temperature is usually comparable to the translational temperature of the beam, whereas the cooling of the vibrational degrees of freedom is noticeably worse. Although, if the energy differences are already large to begin with the population will be primarily in the ground state, even at room temperature. Generally, molecules with smaller energy differences between the internal degrees of freedom cool more efficiently as they require less collisions to transfer internal energy into translation energy. The energy gaps between electronic states are much too large to overcome. However, considering that for most molecules at room temperature only the electronic ground state is populated, the cooling of electronically excited states is of little concern. As the rotational energy level structure produces the smallest energy differences it is the most efficiently cooled. Internally cold molecular samples are especially useful for the application of spectroscopic techniques. Low vibrational or rotational temperatures mean a reduced number of populated energy levels, thus increasing the signal intensity for the populated transitions. In turn, low internal temperatures can simplify a molecular spectrum as less transitions contribute to it.

If a molecule has a sufficient vapour pressure a molecular beam can be easily produced. For liquid or solid samples heating is often needed to increase the vapour pressure. The absolute forward velocities of molecular packets produced via supersonic expansion are very high within the laboratory frame, but as the velocity distribution is narrow the molecular packets are still considered to be cold. The formation of clusters in the supersonic expansion limits the terminal temperature in the beam. To avoid such cluster formation, a rare gas is often used as a seed gas. For a sample expanded in a dilute mixture of rare gas the terminal velocity of the beam is governed by the mass of the carrier gas as well as the temperature and pressure of the source [51]. The mean forward beam velocity for molecules expanded in xenon (131.29 u) from a source at room temperature is approximately 330 m/s. Lighter carrier gas atoms result in faster forward beam velocities, but also a reduction in potential cluster formation. The choice of carrier gas is therefore a compromise between small terminal velocities and cluster formation. Generally, the slower longitudinal velocities of seeded pulsed beams are preferred as starting

points in motion manipulation experiments, such as Stark [52], Zeeman [53] and optical deceleration experiments [54].

1.2.4 Beam manipulation

The manipulation of atomic and molecular beams is almost as old as the field of atomic and molecular beams itself. As early as 1921, Kallmann and Reiche [55] reported calculations for the deflection of a molecular beam of polar molecules with an inhomogeneous electric field and described experiments as ongoing. A year later Stern and Gerlach [56] demonstrated the deflection of a beam of atoms moving through an inhomogeneous magnetic field. For the manipulation of a molecule using external electric, magnetic, or electromagnetic fields, a detailed knowledge of the effect a field has on a molecule's rotational energy level structure is necessary.

Stark and Zeeman effect

In the presence of an electric/magnetic field, the total angular momentum \vec{J} of a molecule is limited to specific discrete orientations in space due to quantization. The magnitude of the vector \vec{J} and its component in the direction of the external field is given by $\hbar(J(J+1))^{1/2}$ and $\hbar M (M = -J, \dots, J)$, respectively. \vec{J} precesses around the direction of the external field at an angle where the cosine is $M/(J(J+1))^{1/2}$. The effect of the external field on the energy of a system's quantum levels depends upon the electric or magnetic field strength and the size of the electric or magnetic dipole moment along the direction of the field. Each effect has been named after the discoverer and recognised with a Nobel prize, the effect of an external electric and magnetic field on such a system is known as the Stark and Zeeman effect, respectively.

To determine the shifting and splitting of rotational energy levels in the presence of an electric/magnetic field quantitatively, it is common to start with an unperturbed rotational Hamiltonian, H_0 . If the rotational energy levels and thus the rotational wave functions are known, a matrix can be built where the rotational energies of the molecule appear on the diagonal and the rotational wave functions are used as a basis set. When the perturbation of the external field, H_{Stark} for an electric field and H_{Zeeman} for a magnetic field, is added to the unperturbed rota-

tional Hamiltonian it introduces off-diagonal matrix elements. The size of these off-diagonal elements, and which rotational levels they couple depend upon the symmetry of the molecule. Once this new matrix has been built it can be diagonalized to yield the energy levels of a molecule in the presence of an external field. This perturbative approach is used throughout this thesis. For more details on this method, relating specifically to the Stark effect, see Section 3.1.1.

Deceleration and acceleration

To manipulate the motion of polar molecules a wide variety of electric and magnetic geometries have been proposed and partly demonstrated [57]. Electric or magnetic deflection is one of the simplest manipulation tools and utilises either the Stark or Zeeman effect to apply a force on a molecule to alter its transverse motion with an inhomogeneous electric or magnetic field. Deflection techniques are often used to determine the electric or magnetic properties for a species of interest [58–60]. Further applications of deflection fields include the separation of individual conformers [61], alignment and orientation studies [62]. With the development of the Stark [52] and Zeeman [53] decelerators, inhomogeneous time-varying electric and magnetic fields were employed, respectively, to change the longitudinal motion of a molecule. For simplicity, and overall relevance to this thesis, the following examples and discussion will focus on Stark deceleration.

Stark deceleration has been successfully applied to a number of different molecules: ND_3 [18, 63], NH_3 [64], NO [65], metastable NH [66, 67], OH [68–72], OD [73], H_2CO [74], SO_2 [75], LiH [76], CaF [77], YbF [78] and SrF [79]. From this list, it is noteworthy to mention that all of the molecules are small with rather simple energy level structures. Techniques that make use of the Stark effect are significantly more effective when applied to molecules that occupy low-field-seeking states, i.e., molecules that increase in potential energy with increasing electric field strength. For techniques that utilise static electric fields, such as the Stark decelerator, molecules in high-field-seeking states are attracted to electrode surfaces, where the electric field is maximum, and therefore lost from a molecular beam.

A Stark decelerator consists of an array of electrode pairs separated by a specific distance (refer to Fig. 1.3). Molecules that approach the plane of the electrodes and

occupy low-field-seeking states will experience a force, due to the inhomogeneous electric field, that opposes its forward motion resulting in a deceleration. As the molecule leaves a region of high electric field the kinetic energy lost would be regained. To avoid this re-acceleration, the electric field is switched off. For the multi-stage set-up of the Stark decelerator, switching succeeding stages between high voltage and ground means that a molecule will continually find itself in front of a decelerating electric field potential as it travels through the decelerator. The switching mechanism is what enables the successful manipulation of a molecular beam's longitudinal motion. For more detailed information regarding the Stark decelerator see Section 3.1.1.

Another approach is travelling-wave deceleration. Here, molecules in low-field-seeking states are confined in a moving electric field minimum that is gradually slowed down in the laboratory frame [80]. For a travelling-wave decelerator a switching scheme is not necessary, which leads to a reduction of losses during the



Figure 1.3: Photograph of Stark decelerator inside a vacuum chamber. For this specific Stark decelerator there are 94 stages, each stage consisting of two steel electrodes with a 3 mm diameter separated by a gap of 2 mm. Adjacent stages are rotated by 90° and separated by 2.5 mm. This forms a square cross-section along the centre of the Stark decelerator through which a molecular beam can travel.

deceleration process. This even enabled the application to diatomic molecules like SrF [79] and YbF [78], whose states are predominantly high-field-seeking, but higher rotational states were identified as low-field-seeking below a certain electric field strength. At typical electric field strengths used in Stark deceleration and trapping experiments (100 kV/cm and more) it is common that larger, more complex molecules occupy high-field-seeking states. Dynamic focusing, such as alternating-gradient (AG) deceleration, can be employed to target high-field-seeking states, but it is experimentally challenging and most of the activities have been discontinued [81–83]. Targeting molecules in high-field-seeking states with static fields alone is limited by Earnshaw’s theorem, which does not allow for high-field maxima in free space. This limitation has, however, led to the development of alternative methods that utilise electromagnetic fields to generate true 3D field maxima in free space.

Manipulation with electromagnetic fields

The manipulation of neutral molecules with large polarizabilities has been achieved with the use of optical fields [54, 84–86]. For experiments that utilise optical fields a permanent dipole moment is unnecessary. Intense laser fields induce a dipole moment that relies on the polarizability of the molecule and the electric field strength, $\vec{\mu}_{ind} \approx \alpha \vec{E}$. The AC-Stark shift ($-\vec{\mu}_{ind} \cdot \vec{E}$) produced by non-resonant radiation creates a potential minimum at a position where the laser intensity is maximum. The force exerted by the electric field gradient is commonly referred to as the optical dipole force. Stapelfeldt et al. [84] employed a pulsed (10 Hz) Nd:YAG laser ($\lambda = 1.06 \mu m$) to observe this effect and redirect a molecular beam of CS₂ seeded with neon. Rapid deceleration and acceleration of a molecular beam of NO and benzene was demonstrated by Fulton et al. in 2006 [54, 87]. In this case, the kinetic energy for a cold beam of NO molecules was reduced by up to 50% and a 75% reduction in kinetic energy was demonstrated for benzene, which is even more impressive considering benzene is a non-polar polyatomic molecule. The polarizable molecules were trapped within the potential wells of a travelling optical lattice, created from the interference pattern of two counter-propagating laser beams. Although effective, the number of molecules this method can be

applied to is limited by the relatively small trap volume determined by the size of the focused laser beam ($\sim \mu\text{m}$).

Microwave fields offer significantly larger manipulation volumes and similarly to optical fields can be applied to a molecule in a high-field-seeking state, which includes its absolute ground state. Due to much smaller electric field gradients, compared to that of a focused laser beam, the application of microwave fields is limited to polar molecules. For polar molecules with rotational constants on the order of a few GHz or less, rotational transitions are typically found within this microwave region providing a large number of molecules to which this technique can be applied to. Microwave manipulation experiments take advantage of the AC-Stark effect to apply a directional force on a molecule in the same way static fields are used in electrostatic traps or decelerators. The strength of this interaction, the AC-Stark effect, is enhanced when the radiation applied is near resonant to a rotational transition frequency. Both the DC and AC-Stark effect are discussed in further detail in Sections 3.1.1 and 3.1.2 .

In 2004, a trap for confining diatomic molecules in high-field-seeking states using microwave fields was proposed [88]. The proposed set-up consisted of an open trap geometry using a Fabry-Perot microwave cavity. Soon thereafter, this concept was adapted for simulating microwave deceleration of polar molecules [89]. Practical application of this approach involved the use of high quality cylindrical microwave resonators and tailored microwave fields to generate field maxima in free space [90]. The $\text{TE}_{1,1,p}$ mode was utilised to demonstrate focusing ($p = 1, 2$) [90, 91], guiding, acceleration and deceleration ($p = 12$) [91, 92] of ammonia molecules in high-field-seeking states. Microwave focusing has also been extended to acetonitrile [93] in a set-up based on a counter-rotating nozzle and a similar microwave resonator. This set-up generates a sample of slow molecules, which are then loaded into a cylindrically symmetric resonator of similar design to those from the previously mentioned microwave studies. Another set-up presented in 2015 investigated the potential of a high-power microwave trap based on an open resonator design [94]. However, as of yet, no experimental demonstration of microwave trapping has been reported.

1.3 Traps for neutral molecules

For molecules that have been decelerated using the techniques discussed in this Chapter, such as Stark and Zeeman deceleration (Sec. 1.2.4), it is possible to confine them in traps for times up to seconds. Traps allow for long interaction times with external probes and can also provide insight into decay processes of quantum states via losses. Generally traps require a potential with a 3D minimum at the centre so that a restoring force can return molecules that diverge from the centre back towards it.

Paramagnetic molecules in low-field-seeking states can be trapped by a field minimum of a static quadrupole magnetic field due to the Zeeman effect. Strong magnetic fields of several Tesla produce traps several Kelvin deep and have been used in combination with the buffer-gas cooling method, for example [95]. Electrostatic traps, which rely on the Stark effect, are very well suited to trapping decelerated polar molecules in low-field-seeking states. The first application of an electrostatic trap was in 2000 with decelerated ND_3 molecules [63]. This design consisted of a ring electrode and two hyperbolic end-caps in quadrupole geometry, a set-up which was originally suggested by Wing for Rydberg atoms [96]. For electrostatic fields different trap geometries can be employed to generate different potentials, such as hexapole traps [97]. Other designs include the electrostatic storage ring, which consists of a hexapole bent into a torus [98, 99]. Decelerated ammonia was detected within the storage ring after 50 round trips, equivalent to a storage time of almost 0.5 s. Another experiment employed 40 straight hexapoles, approximating a hexapole torus design, to store deuterated ammonia for over 13 seconds [100].

The issue with traps based on a single multipole is the zero-field minimum at the centre of the trap. At this position molecules can undergo non-adiabatic transitions into states that experience no restoring force due to a magnetic or electric field, normally these states are high-field-seeking. Such transitions are known to be responsible for major losses of paramagnetic atoms from magnetic traps. This was also confirmed to be a dominant loss channel for electrostatic traps by Kirste et al. [101]. The Ioffe-Pritchard trap can be used to suppress such losses as it applies a constant magnetic/electric field with a specific geometry to

ensure a non-zero minimum at its centre [102].

As with the deceleration/acceleration of molecules in high-field-seeking states, the trapping of such states using static fields alone is again impeded by Earnshaw's theorem. Similar to the AG deceleration method, suitable switching configurations can be employed to target molecules in such states. The AC trapping of $^{15}\text{ND}_3$ molecules was first experimentally demonstrated in 2005 with an electrodynamic trap [103]. Molecules both in low-field- and high-field-seeking states were confined in 3D space by alternating a focusing and defocusing force in each direction. The combination of an inhomogeneous electric multipole field and a homogeneous electric field shaped the overall electric field into a saddle-point potential, which provided a net time-averaged focusing force in all directions.

Trapped molecules are an important pre-requisite for further cooling to ultra-cold temperatures, which can be achieved via sympathetic, Sisyphus or evaporative cooling. Sympathetic cooling brings trapped molecules into contact with an ultra-cold atom gas to establish a new thermal equilibrium via elastic collisions [104]. For cooling polyatomic molecules into the μK regime Sisyphus cooling has proven to be a promising method. When applied to electrically trapped dipolar H_2CO molecules, optoelectrical Sisyphus cooling has been used to generate a molecular ensemble at a temperature of approximately $420 \mu\text{K}$ [105]. Evaporative cooling is also often applied to optically trapped atoms to generate temperatures in the nK regime. This process is only really effective for molecules in low-field-seeking states. Hence, the desire to develop traps that are effective for molecules in high-field-seeking states.



Chapter 2

Theoretical background of rotational spectroscopy

Quantum mechanics provides the underlying theory for our understanding of molecular spectroscopy. Spectroscopy employs static or dynamic electromagnetic fields to probe the energy eigenvalues of a quantum system. In quantum mechanics the energy E of a molecule is calculated with the Schrödinger equation;

$$\hat{H}\Psi = E\Psi \quad (2.1)$$

where \hat{H} denotes the Hamiltonian and Ψ the molecular wave function. According to the Born-Oppenheimer approximation [106] it is possible to separate the coupling between the motion of nuclei and the motion of electrons. Consequently, the total molecular Hamiltonian is represented by the sum of the electronic \hat{H}_{elec} , vibrational \hat{H}_{vib} , rotational \hat{H}_{rot} , translational \hat{H}_{trans} and nuclear spin \hat{H}_{ns} parts:

$$\hat{H} = \hat{H}_{elec} + \hat{H}_{vib} + \hat{H}_{rot} + \hat{H}_{trans} + \hat{H}_{ns} \quad (2.2)$$

Thus the total molecular energy and the total molecular wave function are written as:

$$E = E_{elec} + E_{vib} + E_{rot} + E_{trans} + E_{ns} \quad (2.3)$$

$$\Psi = \psi_{elec}\psi_{vib}\psi_{rot}\psi_{trans}\psi_{ns} \quad (2.4)$$

In this work low temperatures on the order of 1 K, achieved via supersonic expansion, mean that molecules are essentially all in the electronic and vibrational ground states. For molecules with small rotational constants, however, many rotational quantum states remain populated. Microwave spectroscopy probes the rotational part of the Hamiltonian. Consequently the rotational Hamiltonian and its corresponding time-independent Schrödinger equation;

$$\hat{H}_{rot}\psi_{rot} = E_{rot}\psi_{rot} \quad (2.5)$$

is discussed in more detail in the following section.

2.1 Rotational Hamiltonian

The rotational energy of a rigid rotor is given by:

$$E_{rot} = \frac{1}{2}\omega^T I \omega = \frac{P^2}{2I} \quad (2.6)$$

where ω is the angular velocity, P the angular momentum and I the inertia tensor. Only the masses of the nuclei contribute to the inertia tensor as they are much larger in mass relative to the electrons. In a molecule-fixed coordinate system the nuclei are treated as point particles with masses m_i at coordinates x_i , y_i and z_i . Thus the inertia tensor can be written as:

$$I = \sum_{i=0}^N m_i \begin{pmatrix} y_i^2 + z_i^2 & -x_i y_i & -x_i z_i \\ -y_i x_i & x_i^2 + z_i^2 & -y_i z_i \\ -z_i x_i & -z_i y_i & x_i^2 + y_i^2 \end{pmatrix} \quad (2.7)$$

$$I_{xx} = \sum_i m_i (y_i^2 + z_i^2) \quad (2.8)$$

$$I_{yy} = \sum_i m_i (x_i^2 + z_i^2) \quad (2.9)$$

$$I_{zz} = \sum_i m_i(x_i^2 + y_i^2) \quad (2.10)$$

Diagonalization of the inertia tensor transforms it into the molecule-fixed principal axis system. Diagonal elements of the inertia tensor are then defined as the principal moments of inertia and increase in size so that $I_a \leq I_b \leq I_c$. The z-axis is assigned to the principal axis with the highest symmetry, which simplifies the eventual computation of the Hamiltonian. There are 6 different ways in which the molecular fixed axes (x, y, z) can be assigned to the principal axes (a, b, c), these are summarised in Table 2.1. The rigid rotor Hamiltonian \hat{H}_{rr} in the principal axis system can be expressed with the principal moments of inertia in the form;

$$\hat{H}_{rr} = \frac{\hat{P}_a^2}{2I_a} + \frac{\hat{P}_b^2}{2I_b} + \frac{\hat{P}_c^2}{2I_c} \quad (2.11)$$

Table 2.1: Identification of molecule-fixed coordinates x, y, z with the principal axis coordinates a, b, c .

	I^r	I^l	II^r	II^l	III^r	III^l
x	b	c	c	a	a	b
y	c	b	a	c	b	a
z	a	a	b	b	c	c

In rotational spectroscopy it is common to measure transitions as frequencies. Consequently, it is convenient to introduce the dimensionless angular momentum operator \hat{J} . It is also common that rotational constants are used instead of the moments of inertia.

$$\hat{\mathcal{H}}_{rr} = \frac{\hat{H}_{rr}}{h} = (A\hat{J}_a^2 + B\hat{J}_b^2 + C\hat{J}_c^2) \quad (2.12)$$

$$A = \frac{h}{8\pi^2 I_a} \quad (2.13)$$

$$B = \frac{h}{8\pi^2 I_b} \quad (2.14)$$

$$C = \frac{h}{8\pi^2 I_c} \quad (2.15)$$

Although the rigid rotor Hamiltonian relies entirely upon the angular momentum operators defined in the molecular axis system, to determine the rotational energy of a molecule it is still necessary to relate the molecular coordinate system to the laboratory-fixed coordinate system. This transformation is achieved via a series of three rotations, which are described in Figure 2.1.

From commutation relations and with the help of the ladder operators ($\hat{J}_\pm = \hat{J}_x \pm i\hat{J}_y$) eigenvalues and matrix elements of angular momentum operators can be derived [107, 108]. As $[\hat{J}^2, \hat{J}_z] = 0$ and $[\hat{J}^2, \hat{J}_Z] = 0$ due to the Heisenberg uncertainty principle, the wave functions $|J, K, M\rangle$ are simultaneous eigenfunctions of these operators, and the following matrix elements can be constructed:

$$\langle J, K, M | \hat{J}^2 | J, K, M \rangle = J(J+1) \quad (2.16)$$

$$\langle J, K, M | \hat{J}_z | J, K, M \rangle = K \quad (2.17)$$

$$\langle J, K, M | \hat{J}_Z | J, K, M \rangle = M \quad (2.18)$$

with quantum numbers

$$J = 1, 2, 3, \dots,$$

$$K = -J, -J+1, \dots, J-1, J$$

$$M = -J, -J+1, \dots, J-1, J$$

The quantum number J represents the total angular momentum, and quantum numbers K and M then represent the projection of the total angular momentum onto the z - and Z -axis, respectively. In the absence of an external electric or magnetic field the rigid rotor Hamiltonian is invariant against any space-fixed three-dimensional rotation. Corresponding eigenvalues of the rigid rotor are $(2J+1)$ -fold degenerate in M and twofold degenerate in K .

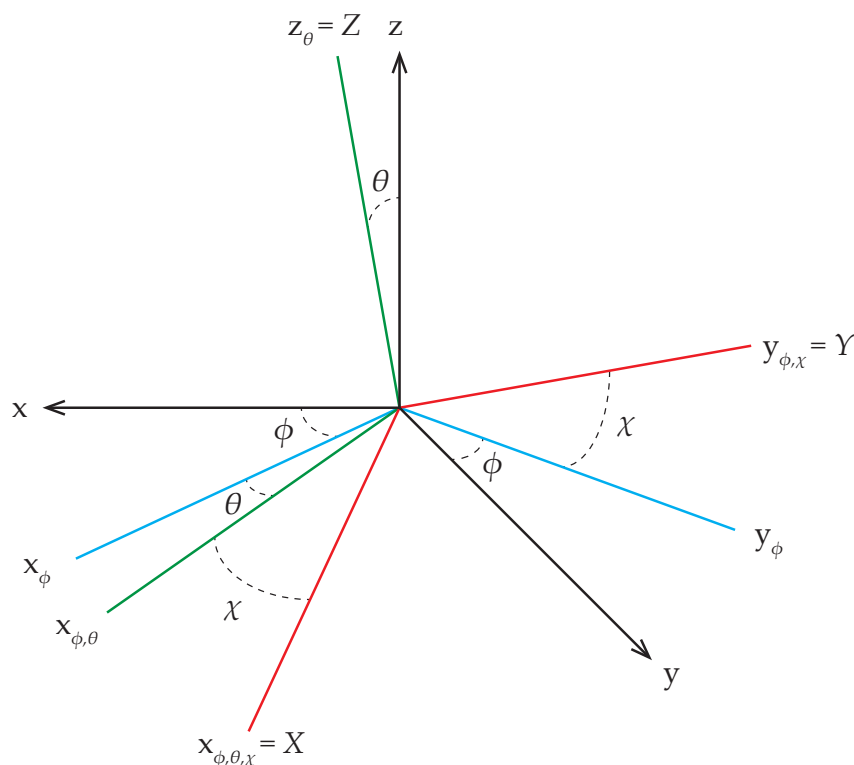


Figure 2.1: Illustration of the Euler angles θ , ϕ and χ , which define the orientation of a molecule (x, y, z) in the laboratory frame (X, Y, Z). Starting in the molecular coordinate system, the first step acquiring the laboratory-fixed coordinate system is the anti-clockwise rotation about z by ϕ , which results in the blue lines x_ϕ and y_ϕ . The second step is an anti-clockwise rotation about y_ϕ by θ , which results in the green lines $x_{\phi,\theta}$ and Z . The third step is the anti-clockwise rotation about Z by χ , which results in the red lines X and Y .

According to the values of each rotational constant with respect to the other, different cases of rigid rotor exist. To observe rotational emission or absorption, a molecule must display a permanent electric dipole moment, which also leads to different selection rules for the different cases. The non-vanishing off-diagonal matrix elements in the symmetric-top representation can be found in Table 3.1. These are useful for determining the selection rules of different rotors. In the following, the Hamiltonian for each type of rigid rotor and the respective selection rules are discussed in more detail.

2.1.1 Linear molecules ($A = \infty$ and $B = C$)

Rotation of a linear molecule occurs within a plane perpendicular to the molecule-fixed axis z . Consequently, the moments of inertia around the axes x and y are equal. In the I^r representation $\hat{J}_a = \hat{J}_z = 0$ and the total angular momentum $\hat{J}^2 = \hat{J}_b^2 + \hat{J}_c^2$ [109], thus $B = C$ and the Hamiltonian is written

$$\hat{\mathcal{H}}_{rr} = B\hat{J}^2 \quad (2.19)$$

with the eigenvalues

$$\mathcal{E}_{rr}(J) = BJ(J+1) \quad (2.20)$$

The non-vanishing matrix elements for a linear molecule can be obtained from Table 3.1 when K is set to zero. Thus the selection rules for a rigid linear molecule are $\Delta J = \pm 1$ and $\Delta M = 0, \pm 1$.

2.1.2 Spherical-top molecules ($A = B = C$)

Such molecules possess an equilibrium structure that belongs to either one of the cubic or icosahedral point groups. The Hamiltonian is represented as

$$\hat{\mathcal{H}}_{rr} = B\hat{J}^2 \quad (2.21)$$

and using the diagonal elements of equation 2.16 the eigenvalues are given as

$$\mathcal{E}_{rr}(J) = BJ(J+1) \quad (2.22)$$

Although the eigenvalues are equal to that of a linear molecule the degeneracy differs. The total degeneracy of a rigid spherical rotor is $(2J+1)^2$, whereas for a linear molecule it is only $2J+1$.

2.1.3 Symmetric-top molecules ($A > B = C$ or $A = B > C$)

Two rotational constants are equal if the point group of the equilibrium structure possess a threefold or higher symmetry axis C_n or S_n ($n > 2$). If $A > B = C$ the

molecule is a prolate symmetric-top. In this case the I^r representation is often used to assign the principal axis a to the molecule-fixed axis z . The Hamiltonian in its diagonal form as shown in equations 2.16 and 2.17 is written as

$$\hat{\mathcal{H}}_{rr} = B\hat{J}^2 + (A - B)\hat{J}_z^2 \quad (2.23)$$

with the eigenvalues

$$\mathcal{E}_{rr}(J, K) = BJ(J + 1) + (A - B)K^2 \quad (2.24)$$

For the oblate symmetric rotor ($A = B > C$) using the III^r representation, the principal axis c coincides with z so that the Hamiltonian is diagonal

$$\hat{\mathcal{H}}_{rr} = B\hat{J}^2 + (C - B)\hat{J}_z^2 \quad (2.25)$$

with the eigenvalues

$$\mathcal{E}_{rr}(J, K) = AJ(J + 1) + (C - A)K^2 \quad (2.26)$$

From the non-vanishing matrix elements of Table 3.1 the selection rules for a symmetric top with μ along z are $\Delta J = 0, \pm 1$, $\Delta K = 0$, and $\Delta M = 0, \pm 1$.

2.1.4 Asymmetric-top molecules ($A \neq B \neq C$)

The largest group of molecules are classified as asymmetric tops, where none of the rotational constants are equal. A measure of a molecule's asymmetry is Ray's asymmetry parameter

$$\kappa = \frac{2B - A - C}{A - C} \quad (2.27)$$

which ranges from -1 to $+1$. These limiting values correspond to the prolate and oblate symmetric-tops respectively. For asymmetric tops the degeneracy of K states is now lifted, refer to Fig. 2.2. The K quantum number is no longer a "good" quantum number so pseudo-quantum numbers, normally written as subscripts of J , are employed to designate the sequence of sub-levels. The King-Hainer-Cross notation [110] uses this double subscript system ($J_{K_a K_c}$) to label the $2J + 1$

It is then necessary to expand the asymmetric rotor wave functions in terms of symmetric rotor wave functions [111]:

$$|J_{KaKc}, M\rangle = \sum_{J,K,M} a_{J,K,M} |J, K, M\rangle \quad (2.28)$$

where $a_{J,K,M}$ are numerical constants and $|J, K, M\rangle$ are the symmetric rotor wave functions. The matrix representation of the rigid rotor Hamiltonian (equation 2.12) is a block diagonal for each J and M . The matrix is independent of M , and as K takes on all integral values between $-J$ and $+J$ each determinant has $(2J + 1)$ rows and columns. Off-diagonal elements in K also need to be included in the matrix. Using the I^r representation (Table 2.1), which is most suited for near-prolate asymmetric tops, the non-vanishing matrix elements of the rigid rotor Hamiltonian are:

$$\langle J, K, M | \hat{\mathcal{H}}_{rr} | J, K, M \rangle = \frac{B + C}{2} (J(J + 1) - K^2) + AK^2 \quad (2.29)$$

$$\begin{aligned} \langle J, K \pm 2, M | \hat{\mathcal{H}}_{rr} | J, K, M \rangle &= \frac{B - C}{4} \sqrt{J(J + 1) - K(K \pm 1)} \\ &\cdot \sqrt{J(J + 1) - (K \pm 1)(K \pm 2)} \end{aligned} \quad (2.30)$$

Similar to symmetric tops, both the I^r and III^r type representations are sufficient to handle most asymmetric-top molecules. After having built the rigid rotor Hamiltonian matrix, energy levels for the asymmetric top can be obtained via diagonalization.

The physics of an asymmetric-top molecule is complicated further by its selection rules. For an asymmetric-top molecule all three dipole moment components along the principle axes can be non-zero. This enables a set of transitions with different selection rules for the pseudo-quantum numbers K_a and K_c , these are listed in Table 2.2. Selection rules for J and M are $\Delta J = 0, \pm 1$ and $\Delta M = 0$. In reality, a rotating molecule is not rigid, especially for higher rotational quantum states. An accurate description of a molecule's rotational states therefore requires the inclusion of centrifugal distortion constants in the Hamiltonian.

Table 2.2: Selection rules for an asymmetric-top molecule.

Dipole	Transition type	ΔK_a	ΔK_c
μ_a	<i>a</i> -type	$0, \pm 2, \dots$	$\pm 1, \pm 3, \dots$
μ_b	<i>b</i> -type	$\pm 1, \pm 3, \dots$	$\pm 1, \pm 3, \dots$
μ_c	<i>c</i> -type	$\pm 1, \pm 3, \dots$	$0, \pm 2, \dots$

2.1.5 Centrifugal distortion

There are two established reduction schemes used in rotational spectroscopy that include the centrifugal distortion constants [112–114]. The A-reduction scheme is most suited to asymmetric-top molecules, whereas the S-reduction is most suited to symmetric and slightly asymmetric molecules. Using the A-reduction scheme the matrix elements of the rotational Hamiltonian that include the five quadratic centrifugal distortion constants ($\Delta_J, \Delta_{JK}, \Delta_K, \delta_J, \delta_K$) are written:

$$\langle J, K, M | \hat{\mathcal{H}}_{rot}^{cd} | J, K, M \rangle = -\Delta_J J^2 (J+1)^2 - \Delta_{JK} J (J+1) K^2 - \Delta_K K^4 \quad (2.31)$$

$$\begin{aligned} \langle J, K \pm 2, M | \hat{\mathcal{H}}_{rot}^{cd} | J, K, M \rangle = & (-\delta_J J (J+1) - \frac{\delta_K}{2} ((K \pm 2)^2 + K^2)) \\ & \cdot \sqrt{J(J+1) - K(K \pm 1)} \\ & \cdot \sqrt{J(J+1) - (K \pm 1)(K \pm 2)} \end{aligned} \quad (2.32)$$

2.2 Nuclear quadrupole splitting

For molecules with nuclei that possess spins \mathbf{I} larger than $1/2$, the electric quadrupole moment of the nuclei will interact with the molecular electric field gradient to generate nuclear hyperfine structure in the rotational spectrum. Quadrupole hyperfine structure was first detected in the microwave region by Good [3] in 1946. The theory established to describe this interaction [115] has been extended to symmetric [4, 116] and asymmetric rotors [117, 118].

Nuclei with spins of 0 or 1/2 are spherically symmetric and therefore have no quadrupole moment Q . For nuclei where $\mathbf{I} \geq 1$ (ellipsoid), the nuclear spin couples to the molecular rotational angular momentum \mathbf{J} . Consequently, the total angular momentum is represented by \mathbf{F} rather than \mathbf{J} , and the new angular momentum quantum numbers are:

$$F = J + I, J + I - 1, \dots, |J - I| \quad (2.33)$$

From the hyperfine structure it is possible to determine the quadrupole coupling tensor's diagonal elements in the principal moment of inertia's axes system.

$$\chi = \begin{pmatrix} \chi_{aa} & \chi_{ab} & \chi_{ac} \\ \chi_{ba} & \chi_{bb} & \chi_{bc} \\ \chi_{ca} & \chi_{bc} & \chi_{cc} \end{pmatrix} \quad (2.34)$$

Upon diagonalization χ is rotated into the principal axis system of the quadrupolar axes, with diagonal elements χ_{xx} , χ_{yy} and χ_{zz} . The nuclear quadrupole coupling constant of χ_{gg} , where $g = x, y, z$, is defined as;

$$\chi_{gg} = eq_{gg}Q = e \frac{d^2V}{dg^2} Q \quad (2.35)$$

where e is the elementary charge, q is the electric field gradient, Q is the nuclear quadrupole moment, and V is the electric potential. The quadrupole coupling constant is directly related to the electric field gradient surrounding the quadrupole nucleus, which can be used to obtain information on the local electronic environment of the nucleus. In the case of a single coupling nucleus or a weak coupling nucleus the assignment of the hyperfine structure is usually straight forward. For molecules with several strongly coupling nuclei the spectra become increasingly complex.

2.3 Spectrum analysis and fitting

Analysis of the rotational spectrum requires the use of an appropriate Hamiltonian, i.e., a Hamiltonian where empirical parameters can be adjusted to fit the observed

frequencies. This is usually an iterative process. The accuracy of the assignment is then reflected in how the effective Hamiltonian parameters fit the observed spectrum. A bad fit would then suggest a misassignment or an unsuitable choice of Hamiltonian. A number of programs have been developed to assist in the analysis of a rotational spectrum. Throughout this work the program PGOPHER [119] was utilized. PGOPHER can implement both the S- and A-reduction of the molecular Hamiltonian. The parameters that can be adjusted include the rotational constants, distortion constants and the nuclear quadrupole coupling constants. All of these parameters can be fit to the observed spectrum simultaneously.

Chapter 3

Experimental details

In this chapter an overview of the two experimental set-ups utilized is given. For the experiments that aim to manipulate the motion of a molecular beam of polar molecules both the Stark decelerator and microwave resonator are included in potential experimental set-ups (refer to Fig. 3.1). Details on the theory needed to understand the application of such apparatus is provided. The chirped-pulse Fourier transform microwave (CP-FTMW) spectrometer COMPACT used in microwave spectroscopy experiments and its experimental details will also be covered in this chapter (see Section 3.2).

3.1 Motion manipulation experiments

Figure 3.1 displays a schematic for the different experimental set-ups that could be employed for the motion manipulation experiments. The combination of a Stark decelerator with a microwave resonator (Fig. 3.1(b)) was first employed as a proof of principle experiment to demonstrate the deceleration of ammonia molecules in high-field-seeking states with microwave fields [91, 92]. Both the Stark decelerator and microwave resonator are housed in a differentially pumped vacuum chamber. A molecular beam of ammonia (17.5%) seeded in xenon is produced by supersonically expanding the mixture into the source chamber. This is done with a modified Parker General Valve Series 9, which is cooled to $-70\text{ }^{\circ}\text{C}$ in order to generate a mean initial longitudinal velocity of approximately 300 m/s. A distance of $\sim 35\text{ mm}$

behind the nozzle opening, a skimmer with an aperture of 1.5 mm separates the source chamber from the Stark decelerator and the detection chamber. A 60 mm long hexapole, consisting of electrodes with a 3 mm diameter, focuses the ammonia molecules into the Stark decelerator. The skimmer has two functions, it preselects molecules with small transverse velocity components and also serves for differential pumping. Operating pressures of 2 to 6×10^{-6} mbar in the source chamber and 2 to 4×10^{-8} in the detection chamber are maintained by turbo-molecular pumps TMU 1001 and TMU 501 (from Pfeiffer Vacuum) backed by a single diaphragm pump. The detection chamber holds a 95-stage Stark decelerator, a cylindrically symmetric microwave resonator, repeller (+1.9 kV) and extractor (+0.5 kV) plates, and a multi-channel plate detector (-1.9 to -2.1 kV) in a compact time-of-flight mass

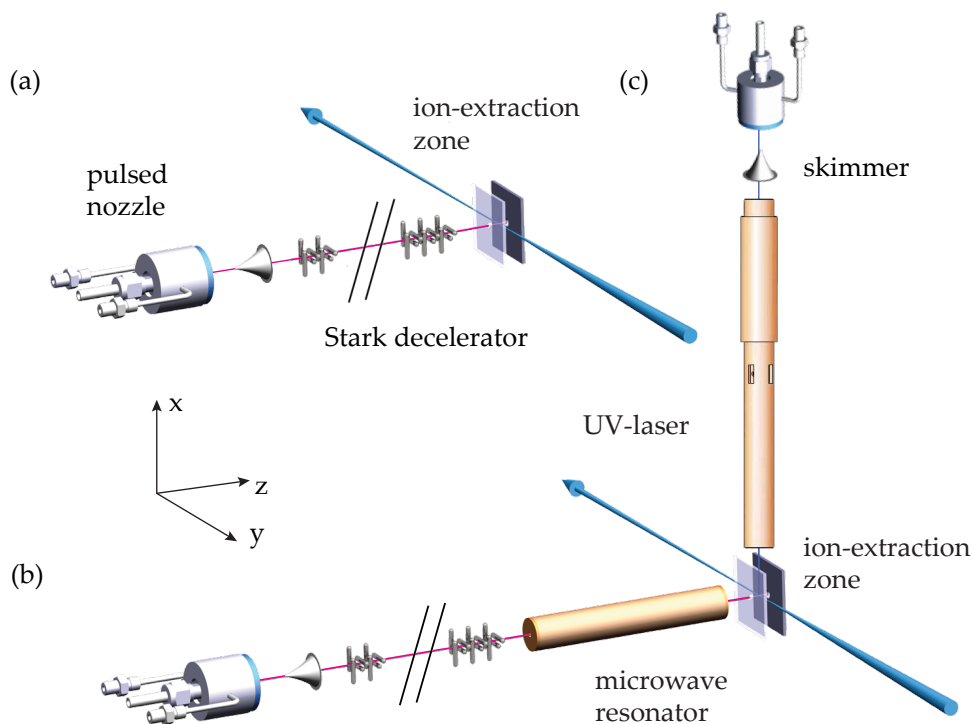


Figure 3.1: Schematic of each motion manipulation experimental set-up (not to scale): (a) Stark deceleration of NH_3 and 4-aminobenzonitrile, (b) Stark and microwave deceleration of NH_3 , (c) microwave manipulation of 4-aminobenzonitrile. Although set-ups (b) and (c) share the same detection region, they cannot be used simultaneously.

spectrometer. The detection region is 5 mm behind the 120 mm long microwave resonator, which is another 4 mm behind the Stark decelerator.

To extend microwave manipulation experiments to larger more complex molecules, such as 4-aminobenzonitrile (see Section 4.2), the same chamber that housed the aforementioned experimental set-up was adapted to accommodate a second molecular beam experiment (Fig. 3.1(c)). This particular experiment was designed to operate on an axis perpendicular to the previously described ammonia experiment and share the same detection region. The supersonic expansion of 4-aminobenzonitrile seeded in xenon would produce a molecular beam with a mean longitudinal velocity close to 400 m/s. Approximately 35 mm behind the valve opening a skimmer is held only 5 mm above a 301 mm long microwave resonator. The distance from the exit of the microwave resonator to the detection region would be 25 mm. Although a smaller distance would be preferred, the dimensions of the extractor and repeller plates make this impractical. In order to determine the feasibility of such an experimental set-up, simulations were carried out, see Section 4.2.2.

For pure Stark deceleration experiments (Fig. 3.1(a)) the microwave resonator is removed from the ammonia experimental set-up, and the detection region moves towards the Stark decelerator. In this case the detection region is located approximately 11 mm behind the Stark decelerator exit. This experimental set-up is included for completeness, as the potential application of the Stark decelerator to 4-aminobenzonitrile is later proposed in Section 4.2.3.

3.1.1 Stark decelerator

The Stark decelerator consist of 95 pairs of parallel electrodes. Each pair of electrodes, a so-called stage, is made of two parallel cylindrical metal rods with a diameter of 3 mm, distanced 2 mm apart from one another. Subsequent stages are rotated by 90° with respect to the previous stage, thereby enabling a focusing force in perpendicular transverse directions, and separated by a distance L of 2.5 mm. The stages at even numbered positions are connected to a different power supply from those stages at odd positions, which means at a given time the even stages can be switched to a high voltage (± 10 kV) whilst the odd stages are grounded

and vice versa. Figure 3.2 shows the two different configurations and the working principle of the Stark decelerator.

A polar molecule in a low-field-seeking state will experience a potential hill as it approaches the pair of high-voltage electrodes. To climb this hill, the molecule's kinetic energy is converted into DC-Stark (potential) energy. If the molecule's kinetic energy is sufficient and its flight path undisturbed it will regain the same amount of kinetic energy when it exits the electric field maximum. In order to prevent the molecule from regaining this energy the voltages are rapidly switched into a second configuration close to the peak of the potential hill. Repeating this process for each of the stages in the Stark decelerator results in a molecular packet of decelerated molecules. The deceleration process is only effective for molecules within the acceptance space of the decelerator. How the acceptance space is defined, depends upon the phase stability of a molecular packet.

Phase stability

The molecular packet that enters the Stark decelerator has a given spatial and velocity distribution. To determine the appropriate switching times for the decelerator a molecule within the phase space of the initial packet is defined as the synchronous molecule. The synchronous molecule is a hypothetical molecule that travels along the molecular beam axis at the exact velocity v_0 supposed to be manipulated so its changes in kinetic energy per stage remain constant. At the time the fields are switched, the position z of the molecule is called the phase angle, $\varphi = z\pi/L$ (with periodicity 2π). In the time between two successive switches the synchronous molecule travels exactly the distance L and is described as "in phase" with the switching of the decelerator. For the synchronous molecule, and those molecules that surround it, an accelerating force is experienced at phase angles smaller than zero. Phase angles larger than zero result in decelerating forces. When the phase angle equals zero this is referred to as guiding, which results in a molecular packet that is kept together in both transverse and longitudinal directions.

To better understand the concept of phase stability the guiding mode is particularly helpful. Whilst guiding, the synchronous molecule travels at a constant

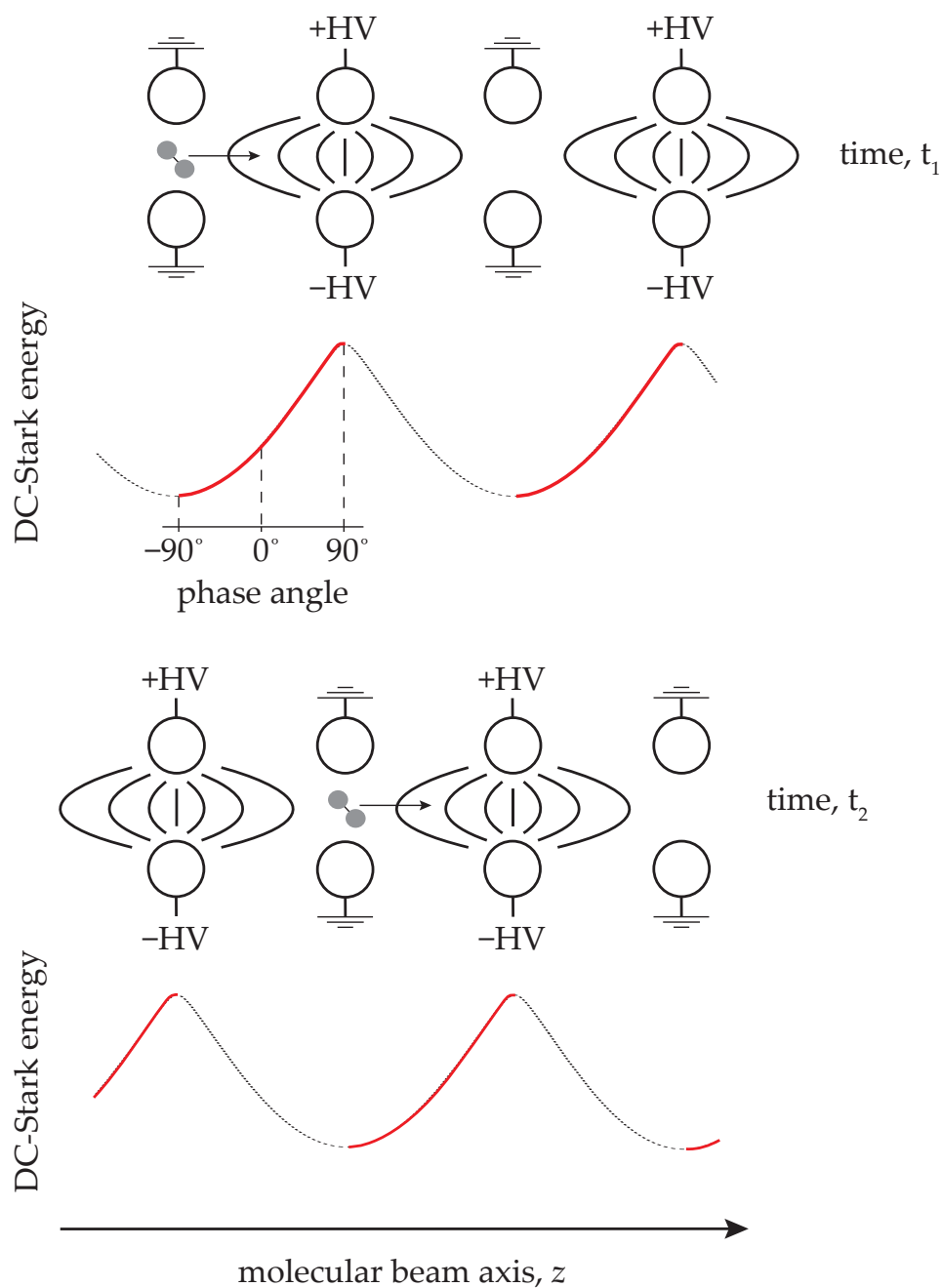


Figure 3.2: Schematic displaying the change in DC-Stark energy for a polar molecule as a function of position z within the Stark decelerator. Switching between the two configurations after a time interval of $t_1 - t_2$ converts kinetic energy from the forward motion into DC-Stark energy. The phase angle φ is used to determine appropriate switching times for the desired effect. Molecules can be accelerated when $\varphi < 0$, guided when $\varphi = 0$ and decelerated when $\varphi > 0$.

phase $\varphi_0 = 0$, thus there is no net change in its kinetic energy. Molecules that have a slightly different phase or velocity experience a correcting force toward the equilibrium values φ_0 and v_0 . For those molecules that lag behind the synchronous molecule the relative phase is $\varphi < 0$. At the switching time, molecules with slightly smaller φ_0 will then gain more kinetic energy than the synchronous molecule and are thus accelerated towards it. The opposite is true for molecules with a relative phase $\varphi > 0$, in this case molecules experience a net deceleration. As a consequence, molecules within a certain region of phase space undergo phase space oscillations around the synchronous molecule. This leads to a well defined molecular packet in longitudinal space, which is maintained throughout the entire Stark decelerator.

The Stark decelerator also works to focus molecules that occupy low-field-seeking states in transverse space. Neighbouring electrode pairs are rotated 90° with respect to the other so that focusing occurs in both transverse directions. For a more detailed explanation of phase-space stability and motion refer to Reference [120].

DC-Stark effect

The DC-Stark effect describes the interaction of a polar molecule's dipole moment $\vec{\mu}$ with a static electric field \vec{E} . When the dipole moment interacts with a time-varying field this is described as the AC-Stark effect. The shift in energy that results from this interaction and the effect on the Hamiltonian can be described using perturbation theory:

$$\hat{H} = \hat{H}_0 + \hat{H}_{Stark} \quad (3.1)$$

where $\hat{H}_{Stark} = -\vec{\mu} \cdot \vec{E}$ accounts for the perturbation and \hat{H}_0 is the unperturbed rotational Hamiltonian.

For a symmetric-top molecule rotating about its symmetry axis, the dipole moment is in the direction of J . The direction of the electric field vector is chosen to coincide with an axis in the laboratory frame, and the projection of J on such an axis is always an integer of M . It is also necessary to consider the projection of J along the symmetry axis K . With all this considered, the change in energy

of a symmetric top due to the Stark effect can be written:

$$\Delta W_{DC-Stark} = -\mu E \frac{MK}{J(J+1)} \quad (3.2)$$

This change in energy is proportional to the first power of μE and is therefore referred to as the first-order Stark effect. Second-order Stark shifts are only due to the molecular dipole moments and are generally much smaller as they depend on the square of the electric field strength. For a more indepth description of the higher order DC-Stark effects refer to References [121, 122].

For a more rigorous derivation, \hat{H}_{Stark} can be expressed in terms of directional cosines ϕ . Using the dipole moment matrix elements from Table 3.1, the symmetric-top wave function with rotational quantum numbers J, K, M gives;

$$\begin{aligned} \langle J, K, M | \hat{H}_{Stark} | J', K', M' \rangle &= -\mu E \phi_{J,J'} \phi_{JK,J'K'} (\phi_z)_{JM,J'M'} \\ &= -\mu E \frac{MK}{J(J+1)} \end{aligned} \quad (3.3)$$

which is exactly the same as Equation 3.2. The selection rules of the molecule determine which rotational states interact with each other through this perturbation. For a symmetric top, matrix elements are non-zero for all the combination of states where $J = J'$, or $J = J' \pm 1$ when $M = M'$ and $K = K'$.

The complexity of the matrix depends on the molecule's symmetry as well as the number of rotational states included. For example, the inversion-split vibronic ground state of para-ammonia ($|J, K\rangle = |1, 1\rangle$) consists of two components with differing symmetry that interact strongly via an external field. Here, ammonia can be treated as a two-level system, which means a 2×2 matrix can be used to describe the Hamiltonian. To find the 1st-order DC-Stark energy of the inversion doublet the matrix can be written as:

$$H = \begin{pmatrix} \frac{W_{inv}}{2} & -\mu \frac{MK}{J(J+1)} E \\ -\mu \frac{MK}{J(J+1)} E & -\frac{W_{inv}}{2} \end{pmatrix} \quad (3.4)$$

where W_{inv} is the inversion splitting in the absence of an external field. The energy eigenvalues of the states ϵ_i can then be determined by diagonalizing H so that:

$$\epsilon_{1,2} = \pm \sqrt{\left(\frac{W_{inv}}{2}\right)^2 + \left(\mu E \frac{MK}{J(J+1)}\right)^2} \quad (3.5)$$

where the positive square root describes the energy of molecules that occupy the low-field-seeking state of the inversion doublet, and the negative the high-field-seeking state.

For an asymmetric-top molecule, like 4-aminobenzonitrile, an increased density of rotational states and less symmetry means the molecular system can no longer be approximated as a two-level system. Linear combinations of symmetric-top wave functions $|J, K, M\rangle$ are used as the basis set for the Hamiltonian matrix, and the off-diagonal matrix elements are again obtained from Table 3.1. If the asymmetric top is near-prolate ($K = K_a$) the I^r representation is used to assign the off-diagonal elements, and if it is near-oblate ($K = K_c$) the III^r representation is used. Different selection rules introduce more coupling between the rotational states ($\Delta J = 0, \pm 1$, $\Delta K = 0, \pm 1$, $\Delta M = 0$), and also determine if crossing or avoided crossing occurs as rotational states approach each other with increasing electric field strength. The Wang transformation [123] can be used to simplify the Hamiltonian matrix by transforming it into a symmetrized basis. When an external field is then applied the size of the matrix is reduced depending upon the direction of the dipole moment and the values of M . This approach is not employed in this thesis, but mentioned here for completeness. For more detailed information on the application of the Wang transformation see References [111, 124].

Table 3.1: Dipole moment matrix elements taken from Reference [121]. The ϕ 's are factors of the directional cosine matrix and depend upon the rotational quantum numbers indicated by subscripts, as well as the molecular axis being evaluated. The elements listed are appropriate for a prolate symmetric top using the I^r representation. For the oblate symmetric top the III^r representation can be used by switching ϕ_a with ϕ_c , ϕ_b with ϕ_a , and ϕ_c with ϕ_b . The x , y , z subscripts depend upon a molecules orientation with respect to the polarization of an external field.

Matrix element factor	Value of J'		
	$J + 1$	J	$J - 1$
$\phi_{J,J'}$	$[4J(J + 1)\sqrt{(2J + 1)(2J + 3)}]^{-1}$	$[4J(J + 1)]^{-1}$	$[4J\sqrt{4J^2 - 1}]^{-1}$
$(\phi_a)_{JK,J'K}$	$2J\sqrt{(J + 1)^2 - K^2}$	$2K$	$2J\sqrt{J^2 - K^2}$
$(\phi_b \text{ or } \pm i\phi_c)_{JK,J'K\pm 1}$	$\mp\sqrt{(J \pm K + 1)(J \pm K + 2)}$	$\sqrt{(J \mp K)(J \pm K + 1)}$	$\mp\sqrt{(J \mp K)(J \mp K - 1)}$
$(\phi_z)_{JM,J'M}$	$2\sqrt{(2J + 1)^2 - M^2}$	$2M$	$2J\sqrt{J^2 - M^2}$
$(\phi_x \text{ or } \pm i\phi_y)_{JK,J'M\pm 1}$	$\mp\sqrt{(J \pm M + 1)(J \pm M + 2)}$	$\sqrt{(J \mp M)(J \pm M + 1)}$	$\mp\sqrt{(J \mp M)(J \mp M - 1)}$

3.1.2 Microwave resonators

The application of microwave waveguides and resonators for spectroscopic purposes has been going on for close to 70 years [121]. Continued development led to the invention of the MASER [5, 6] the first experimental demonstration of stimulated emission. Besides the spectroscopic applications, microwave resonators offer promising features for experiments in motion manipulation. Closed cylindrically symmetric microwave resonators are employed by both the experimental set-ups that focus on microwave manipulation, which are described in Section 3.1. Tailored microwave fields can be generated by using high-quality microwave resonators. With electric field maxima on the molecular beam axis, acceleration, deceleration and focusing of polar molecules in high-field-seeking states can be achieved [90–92]. The following section introduces the theory needed to understand the functioning of such resonators and is mostly based on References [125, 126]. The AC-Stark effect is also introduced here and discussed in detail.

Maxwell's equations

The Maxwell equations include Gauss' law, Gauss' law of magnetism, Faraday's law of induction, and Ampere's law, all of which are necessary for understanding the physics of an electromagnetic wave travelling through a waveguide/microwave resonator. Gauss' law,

$$\vec{\nabla} \cdot \vec{E} = \frac{\rho}{\epsilon_0} \quad (3.6)$$

describes how an electric field \vec{E} is generated by an electric charge density ρ , where the permittivity of vacuum is $\epsilon_0 = 8.852 \times 10^{-12} \text{ As/Vm}$. Gauss' law of magnetism states that the divergence of a magnetic field \vec{B} is zero:

$$\vec{\nabla} \cdot \vec{B} = 0 \quad (3.7)$$

Faraday's law of induction states that a time-dependent magnetic field can induce an electric field:

$$\vec{\nabla} \times \vec{E} = -\frac{\partial \vec{B}}{\partial t} \quad (3.8)$$

And Ampere's law states that the movement of charges \vec{J} , or time-dependent electric fields, can be used to generate a magnetic field:

$$\vec{\nabla} \cdot \vec{B} = \mu_0 \left(\vec{J} + \epsilon_0 \frac{\partial \vec{E}}{\partial t} \right) \quad (3.9)$$

where the constant for the permeability of vacuum is $\mu_0 = 4\pi \times 10^{-7}$ Am/Vs.

A practical application of Maxwell's equations is to consider the propagation of an electromagnetic wave along the symmetry axis of a hollow metallic cylinder. In this case, both the cross sectional size and shape are assumed to be constant along the cylinder axis (z -axis). For an electromagnetic wave with a time dependence $e^{-i\omega t}$ propagating along the positive z -axis in the Cartesian coordinate system, Maxwell's equations take the form:

$$\vec{\nabla} \cdot \vec{E} = i\omega \vec{B} \quad (3.10)$$

$$\vec{\nabla} \cdot \vec{B} = -i\mu\epsilon\omega \vec{E} \quad (3.11)$$

$$\vec{\nabla} \times \vec{E} = 0 \quad (3.12)$$

$$\vec{\nabla} \cdot \vec{B} = 0 \quad (3.13)$$

where $\mu = \mu_r \mu_0$ and $\epsilon = \epsilon_r \epsilon_0$, which describe the permeability and permittivity of the dielectric medium that fills the cylinder, respectively. Constants with the r subscript describe the relative values for the dielectric medium with respect to vacuum.

For the cylindrical geometry it is useful to separate the transverse field components from the longitudinal field component:

$$\vec{E}(x, y, z, t) = \vec{E}(x, y) e^{-ikz - i\omega t} \quad (3.14)$$

$$\vec{B}(x, y, z, t) = \vec{B}(x, y) e^{-ikz - i\omega t} \quad (3.15)$$

where k is an unknown parameter that could be real or complex. With the assumed z -dependence of the fields, the wave equation can be reduced to the two dimensional form:

$$\left(\vec{\nabla}_t^2 + (\mu\epsilon\omega^2 - k^2)\right) \cdot \begin{pmatrix} \vec{E} \\ \vec{B} \end{pmatrix} = 0 \quad (3.16)$$

where the Laplacian operator is $\vec{\nabla}_t^2 = \vec{\nabla}^2 - \partial^2/\partial z^2$. As the Maxwell equations satisfy the wave equation, the transverse field components can then be derived from the first two Maxwell equations (Eq. 3.10 and 3.11):

$$\vec{E}_t = \frac{1}{\mu\epsilon\omega^2 - k^2} \left(\vec{\nabla}_t \frac{\partial E_z}{\partial z} - i\omega \hat{z} \times \vec{\nabla}_t B_z \right) \quad (3.17)$$

$$\vec{B}_t = \frac{1}{\mu\epsilon\omega^2 - k^2} \left(\vec{\nabla}_t \frac{\partial B_z}{\partial z} - i\mu\epsilon\omega \hat{z} \times \vec{\nabla}_t E_z \right) \quad (3.18)$$

where \hat{z} is the unit vector in the z -direction. Solving the wave equation (Eq. 3.16) requires finding a solution for the longitudinal electric and magnetic field components (E_z and B_z , respectively). The transverse field components can then be calculated from Equations 3.17 and 3.18.

Waveguides and resonators

To determine the distribution of electric field strength within a waveguide, the effect of the waveguide on the electromagnetic wave needs to be considered. For a perfect conductor the electric and magnetic fields must satisfy the boundary conditions at its surface:

$$\hat{n} \times \vec{E} = 0 \quad (3.19)$$

$$\hat{n} \cdot \vec{B} = 0 \quad (3.20)$$

where \hat{n} is the unitary normal vector on the waveguide surface S . Once again, the transverse and longitudinal field components can be split, thus simplifying the boundary conditions so:

$$E_z|_S = 0 \quad (3.21)$$

$$\left. \frac{\partial B_z}{\partial n} \right|_S = 0 \quad (3.22)$$

From the wave equation (Eq. 3.16) and the boundary conditions (Eq. 3.21 and 3.22) an initial value problem arises as the boundary conditions to \vec{E}_z and \vec{B}_z cannot be satisfied everywhere. Thus solutions to this problem are separated into three different categories:

- Transverse magnetic (TM) modes with $B_z = 0$ everywhere.
- Transverse electric (TE) modes with $E_z = 0$ everywhere.
- Transverse electromagnetic (TEM) modes with $B_z = E_z = 0$ everywhere.

The microwave resonators employed within this thesis exploit only the TE modes, so from here on the discussion will focus on this category.

The microwave resonator is a hollow, cylindrically symmetric waveguide with a constant cross section throughout, which is closed at each end. What differentiates the resonator from the waveguide is the inclusion of end-caps. The addition of end-caps to the cylindrically symmetric waveguide results in reflections between the front and end face of the resonator. As the end-caps are plane and perpendicular to the axis of the cylinder, the z -dependence of the fields are that appropriate to standing waves:

$$E_z(z) = A \sin kz + B \cos kz \quad (3.23)$$

Boundary conditions can be satisfied at each end-cap surface ($z = 0$ and $z = d$, where d is the length of the resonator) only if:

$$k = \frac{p\pi}{d}, \quad p = 0, 1, 2, \dots \quad (3.24)$$

where, p is the longitudinal mode number. For the TE mode ($E_z = 0$), the vanishing of B_z at $z = 0$ and $z = d$ requires:

$$B_z = B_0 \psi(\rho\phi) \sin \frac{p\pi z}{d}, \quad p = 1, 2, 3, \dots \quad (3.25)$$

In the cylindrical coordinate system, the scalar wave function $\psi = B_z$ is a solution to the two-dimensional wave equation:

$$\frac{1}{\rho} \frac{\partial}{\partial \rho} \left(\rho \frac{\partial \psi}{\partial \rho} \right) + \frac{1}{\rho^2} \frac{\partial^2 \psi}{\partial \phi^2} + \gamma^2 = 0 \quad (3.26)$$

From this equation (Eq. 3.26) and Equation 3.24 the resonance frequencies of the resonator can be obtained:

$$\gamma_{m,n}^2 = \mu\epsilon\omega^2 - \left(\frac{p\pi}{d} \right)^2 \quad (3.27)$$

For each value of p the $\gamma_{m,n}^2$ determines the resonance frequencies for the TE modes of the resonator:

$$\omega_{m,n,p} = \frac{c}{\sqrt{\mu_r \epsilon_r}} \sqrt{\frac{x_{m,n}'^2}{R^2} + \frac{p^2 \pi^2}{d^2}} \quad (3.28)$$

where $x_{m,n}'^2$ is the n^{th} root of the first derivative of the m^{th} order Bessel function, and the solution to the constant γ for the TE modes is $\gamma_{m,n} = x_{m,n}'^2/R$.

To calculate the transverse field components for the TE mode of the resonator, Equation 3.25 needs to be inserted into Equations 3.17 and 3.18:

$$\vec{E}_t = -B_0 \frac{i\omega}{\gamma_{m,n}^2} \sin \left(\frac{p\pi z}{d} \right) \hat{z} \times \vec{\nabla}_t \psi(\rho, \phi) \quad (3.29)$$

$$\vec{B}_t = B_0 \frac{p\pi}{d\gamma_{m,n}^2} \cos \left(\frac{p\pi z}{d} \right) \vec{\nabla}_t \psi(\rho, \phi) \quad (3.30)$$

For the $\text{TE}_{1,1,p}$ mode these equations can be further simplified so:

$$\vec{E}_t(\rho, \phi, z) = -B_0 \frac{i\omega}{\gamma_{1,1}^2} \sin \left(\frac{p\pi z}{d} \right) \hat{z} \times \vec{\nabla}_t J_1(\gamma_{1,1}\rho) \cos \phi \quad (3.31)$$

$$\vec{B}_t(\rho, \phi, z) = B_0 \frac{p\pi}{d\gamma_{1,1}^2} \cos \left(\frac{p\pi z}{d} \right) \vec{\nabla}_t J_1(\gamma_{1,1}\rho) \cos \phi \quad (3.32)$$

The electric field component can then be calculated from:

$$E_\rho(\rho, \phi, z) = -E_0 \frac{i\omega}{\gamma_{1,1}^2 c} \frac{J_1(\gamma_{1,1}\rho)}{\rho} \sin \phi \sin\left(\frac{p\pi z}{d}\right) \quad (3.33)$$

$$\begin{aligned} E_\phi(\rho, \phi, z) &= -E_0 \frac{i\omega}{\gamma_{1,1}^2 c} \frac{\partial}{\partial \rho} J_1(\gamma_{1,1}\rho) \cos \phi \sin\left(\frac{p\pi z}{d}\right) \\ &= -E_0 \frac{i\omega}{\gamma_{1,1}^2 c} \left(J_0(\gamma_{1,1}\rho) - \frac{J_1(\gamma_{1,1}\rho)}{\gamma_{1,1}\rho} \right) \cos \phi \sin\left(\frac{p\pi z}{d}\right) \end{aligned} \quad (3.34)$$

$$E_z(\rho, \phi, z) = 0 \quad (3.35)$$

Now the analytical solutions for the electric fields in a closed cylinder are known. A 3D-plot of the electric field distribution for the $\text{TE}_{1,1,18}$ mode in a closed, cylindrically symmetric resonator is shown in Figure 3.3. To calculate the Stark shifts induced by the electromagnetic field coupled to the resonator the electric field strength E_0 needs to be determined. This parameter is required for the simulation of potential motion manipulation experiments, such as the guiding of a molecular beam of 4-aminobenzonitrile (see Section 4.2.2).

Electric field strength

To calculate the electric field strength, the energy stored in the field W at a specific resonance frequency ω_0 needs to be determined first. Important variables include the input power P_{IN} and the quality factor Q of the resonator. The quality factor is essentially the ratio between the energy stored W and the power lost (P_{loss}) at a resonance frequency.

$$Q = \omega_0 \frac{W}{P_{\text{loss}}} \quad (3.36)$$

A detailed derivation of this variable can be found in Reference [125]. Once the system reaches an equilibrium where both the input power and the power lost are equal, the stored energy can be calculated via:

$$W = \frac{P_{\text{IN}} Q}{\omega_0} \quad (3.37)$$

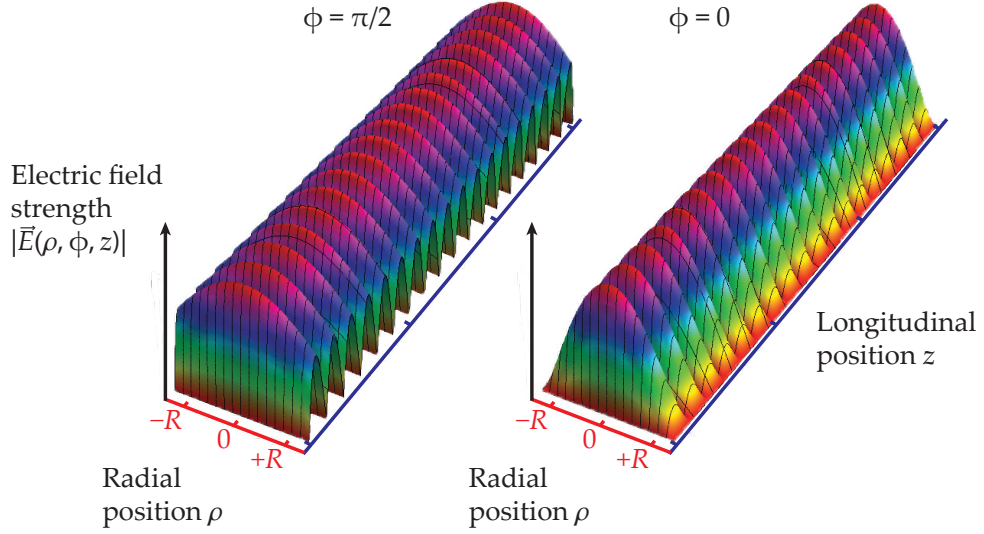


Figure 3.3: Electric field distribution $|\vec{E}(\rho, \phi, z)|$, depending upon the position in the (ρ, z) -plane with $\phi = \pi/2$ (left) and $\phi = 0$ for the $\text{TE}_{1,1,18}$ mode of the microwave resonator design for the 4-aminobenzonitrile experiments. The 301 mm long resonator has an inner diameter of 13.23 mm at room temperature.

Combining the above equation (Eq. 3.37) with that of the total time-averaged energy for a linearly polarized plane wave, the electric field strength of the $\text{TE}_{m,n,p}$ mode takes the form:

$$E_0 = c \sqrt{\frac{8P_{\text{IN}}Q}{\epsilon_0\omega_0^3\pi R^4d \left[1 - \left(\frac{m}{x'_{m,n}}\right)^2\right]}} \frac{x'_{m,n}}{J_m(x'_{m,n})} \quad (3.38)$$

where J_m are the Bessel functions of the first kind and m^{th} order.

The maximum electric field strength is then obtained by utilising additional factors $\omega R(cx'_{m,n})^{-1}$ from Equation 3.31, and noting that the maximum of the Bessel function $J_1(x)$ is $1/2$ at $x = 0$. Thus:

$$E_{0,\text{max}} = \sqrt{\frac{2P_{\text{IN}}Q}{\epsilon_0\omega_0\pi R^2d \left[1 - \left(\frac{m}{x'_{m,n}}\right)^2\right]}} \frac{1}{J_m(x'_{m,n})} \quad (3.39)$$

For a specific mode like the $\text{TE}_{1,1,p}$, which is most relevant to this thesis, the above

equation can be simplified further to:

$$\begin{aligned} E_{0,max} &= \sqrt{\frac{2P_{IN}Q}{\epsilon_0\omega_0V(x'_{1,1}{}^2 - 1)}} \frac{x'_{1,1}}{J_1(x'_{1,1})} \\ &= 2.9 \cdot \sqrt{\frac{P_{IN}Q}{\epsilon_0\omega_0V}} \end{aligned} \quad (3.40)$$

The maximum electric field strength is thus dependent upon the square root of the input power and the square root of the quality factor, as well as the resonator volume ($V = \pi R^2 d$).

AC-Stark effect

The interaction of a molecule with an electromagnetic field is described by the AC-Stark effect. In principle, the Hamiltonian 3.1 is still valid. However, as the electric field is time-dependent, one would need to solve the time-dependent Schrödinger equation to quantify the effect. An alternative approach, often used to describe the interaction of atoms with intense fields, is the dressed-state model [127, 128]. In this approach the electric field is considered as a quantised photon bath, rather than a classical field. Thus the Hamiltonian can be written:

$$\mathcal{H} = H_{rot} + H_{AC-Stark} + H_{EM} \quad (3.41)$$

where H_{rot} is the pure rotational Hamiltonian, $H_{AC-Stark}$ the Hamiltonian for the interaction between the field and the molecule, and H_{EM} the Hamiltonian for the quantized electromagnetic field, $H_{EM} = h\nu(\hat{a}^\dagger\hat{a} + 1/2)$. This incorporates both the photon creation operator \hat{a}^\dagger and the photon annihilation operator \hat{a} .

Using the dressed-state formalism reported in Reference [127], the dressed-states are the eigenfunctions for the total Hamiltonian \mathcal{H} . Each of the field-free rotational states E_n are dressed by a field that contains m number of photons. In this approach, coupling between rotational states dressed by a field that differs by one m photon ($\Delta m = \pm 1$) is allowed, coupling between states dressed with a field of the same number photons is forbidden. For a two-level system like ammonia, with unperturbed energy eigenvalues E_0 and E_1 , the Hamiltonian takes the form:

$$\mathcal{H} = \begin{pmatrix} E_1 + mh\nu & -\mu\mathcal{E}/2 \\ -\mu\mathcal{E}/2 & E_0 + (m+1)h\nu \end{pmatrix} \quad (3.42)$$

where the local electric field amplitude $\mathcal{E} = |\vec{E}(\rho, \phi, z)|$, and μ is the transition dipole moment between the two coupled states.

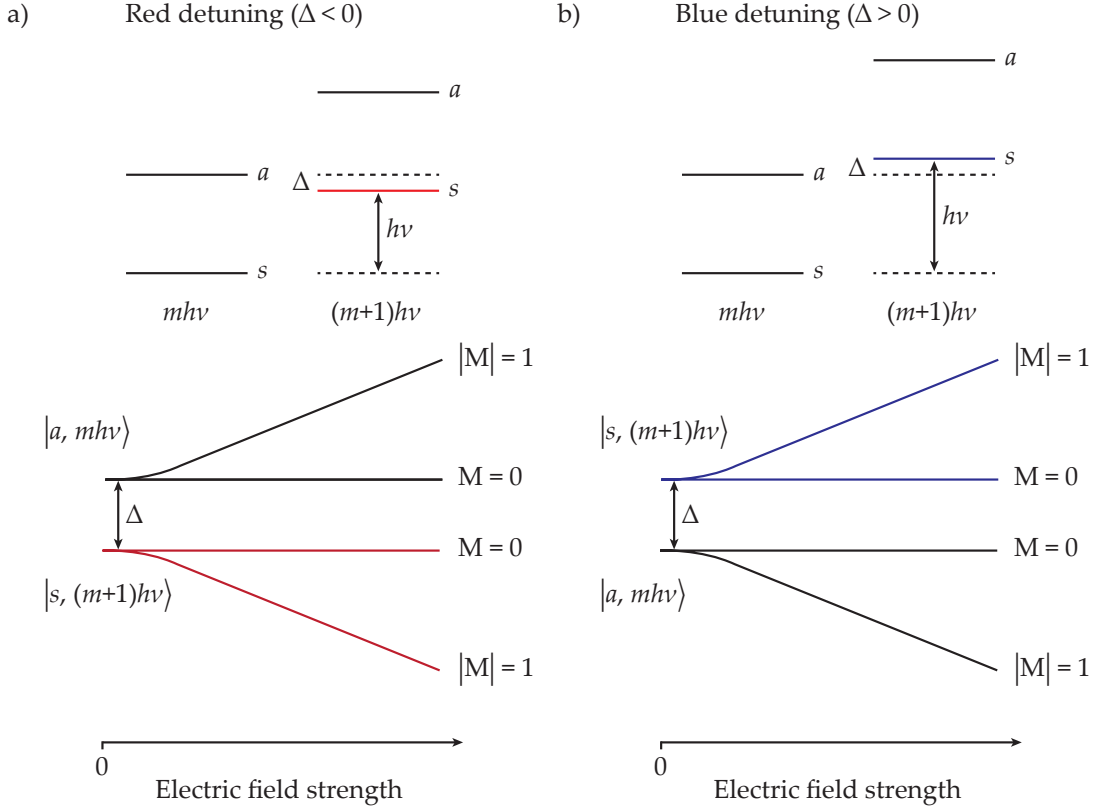


Figure 3.4: Dressed state picture and AC-Stark shift of the $|J, K\rangle = |1, 1\rangle$ inversion doublet of ammonia based on the scheme used in Reference [90]. Both (a) red and (b) blue detuning schemes are displayed. From the (b) scheme it is easier to see how the originally high-field-seeking behaviour of the symmetric (s) level becomes low-field-seeking when blue detuned from the antisymmetric (a) level.

The AC-Stark shifts can be calculated by including the detuning ($\Delta = \nu - \nu_{mol}$) of the microwave frequency with respect to the molecular transition frequency ν_{mol} , and then diagonalizing the Hamiltonian. When ν is red detuned from ν_{mol} ($\Delta < 0$), the AC-Stark energy for the upper state is:

$$W_{\text{AC-Stark}} = E_1 + \frac{1}{2} \left[\sqrt{(h\Delta)^2 + (\mu\mathcal{E})^2} + h\Delta \right] \quad (3.43)$$

and for the lower state it is:

$$W_{\text{AC-Stark}} = E_0 - \frac{1}{2} \left[\sqrt{(h\Delta)^2 + (\mu\mathcal{E})^2} + h\Delta \right] \quad (3.44)$$

Detuning introduces two additional parameters that can be exploited for the motion manipulation of polar molecules with AC-electric fields. The sign of the detuning can be used to switch the field-seeking behaviour of the rotational state under investigation. For example, with deceleration experiments carried out on ammonia [90–92] it was necessary to blue-detune from the inversion frequency mentioned in Section 3.1.1. This meant that the pre-decelerated packet of molecules in the low-field-seeking state could be treated as high-field-seeking in a microwave resonator, refer to Figure 3.4 for a more detailed look into how the dressed-state model has been applied to ammonia. The magnitude of the detuning also impacts the strength of the AC-Stark shift. A small detuning results in a strong, linear AC-Stark shift already at weak electric field strengths. Although small detunings are preferred, depending on the input power microwave radiation that is too close to resonance should be avoided as it can lead to unwanted transitions.

Similarly to the DC-Stark effect, the calculation of the AC-Stark effect is further complicated when applied to a multi-level system. To extend the dressed-state model to molecules where several energy levels interact in the presence of a microwave field, the Hamiltonian can be written as a block matrix:

$$\mathcal{H} = \left(\begin{array}{ccc|ccc} E_0 + mh\nu & 0 & \dots & 0 & \dots & 0 \\ 0 & \ddots & 0 & \Omega_{n,n'} & 0 & \vdots \\ \vdots & 0 & E_N + mh\nu & \Omega_{n,n'} & \Omega_{n,n'} & 0 \\ \hline 0 & \Omega_{n',n} & \Omega_{n',n} & E_0 + (m+1)h\nu & 0 & \dots \\ \vdots & 0 & \Omega_{n',n} & 0 & \ddots & 0 \\ 0 & \dots & 0 & \vdots & 0 & E_N + (m+1)h\nu \end{array} \right) \quad (3.45)$$

Field-free rotational states E_n ($n = 0, 1, 2, \dots, N$), when dressed with a microwave field $mh\nu$, form the diagonal for the first block in the dressed-state matrix. The subsequent diagonal block is then dressed with a field where the photon number m is increased by one. To incorporate the new selection rule introduced by the dressed-state model ($\Delta m = \pm 1$), there are no off-diagonal elements included within the diagonal blocks. Instead, only the off-diagonal blocks consider the coupling between the dressed rotational states. The off-diagonal dipole moment matrix elements (refer to Table 3.1) form the coupling components $\Omega_{n,n'} = -\frac{1}{2}\mathcal{E}(\mu_z)_{n,n'}$, which are determined by the selection rules of the molecule. For example, the selection rules for an asymmetric top are $\Delta J = 0, \pm 1$, $\Delta K_a = 0, \pm 1$, $\Delta K_c = 0, \pm 1$, and $\Delta M = 0$, which means non-vanishing off-diagonal dipole moment matrix elements occur for transitions that obey these rules. Once the dressed-state matrix is complete it can be diagonalized at different values of the electric field strength to obtain the shifted energy levels.

3.1.3 Detection

One-colour two-photon resonance enhanced multi-photon ionization, also known as 2+1-REMPI, is used in the detection of ammonia (Fig. 3.5) [129]. Here, 2+1 indicates that two photons are necessary to excite a molecule from the ground state $X(v_2 = 0)$ into an electronically and vibrationally excited state $B(v_2 > 0)$. The third photon of the same wavelength is what ionizes the molecule, thus enabling detection with a simple time-of-flight (TOF) mass spectrometer. A Wiley-McLaren type TOF mass spectrometer [130] combined with a 250 mm drift tube and two electrode plates complete the detection set-up. The electrode plates are separated by 5.5 mm and put under different voltages. One plate acts as a repeller for the ammonia ions with a voltage of +1.9 kV, and the second acts as the extractor with a voltage of +500V. Each plate has an aperture of 3 mm covered in a fine nickel mesh, which allows for a high particle transmission and homogeneous electric fields. The next stage is the drift tube at -1.2 kV, which focuses the ions towards a Jordan micro channel plate (MCP) set to -2.1 kV.

Ionization of the $|J, K\rangle = |1, 1\rangle$ state of ammonia requires near-UV radiation of 312 nm for the upper inversion component. As the 2+1-REMPI scheme involves

a two-photon transition, high photon intensities are required. To achieve this, an Nd:YAG-pumped-dye-laser system is employed. The Nd:YAG laser, a Spitlight 500 from InnoLas, is frequency doubled with an anti-reflex coated lithiumtriborate (LBO) crystal to produce a 300 mJ pulse of 532 nm light at a 10 Hz repetition rate. For ammonia, DCM dissolved in ethanol is used as the dye in the dye-laser (Narrowscan by Radiant Dyes). This generates broadband light from 620 to 640 nm. A resonator consisting of two grazing-incident gratings facilitates the selection of a specific wavelength within this range. After an amplification stage, the red laser light is frequency doubled by a potassiumdiphosphate (KDP) crystal to produce UV light at 12–16 mJ per pulse.

For the application of this detection set-up to 4-aminobenzonitrile, the dye

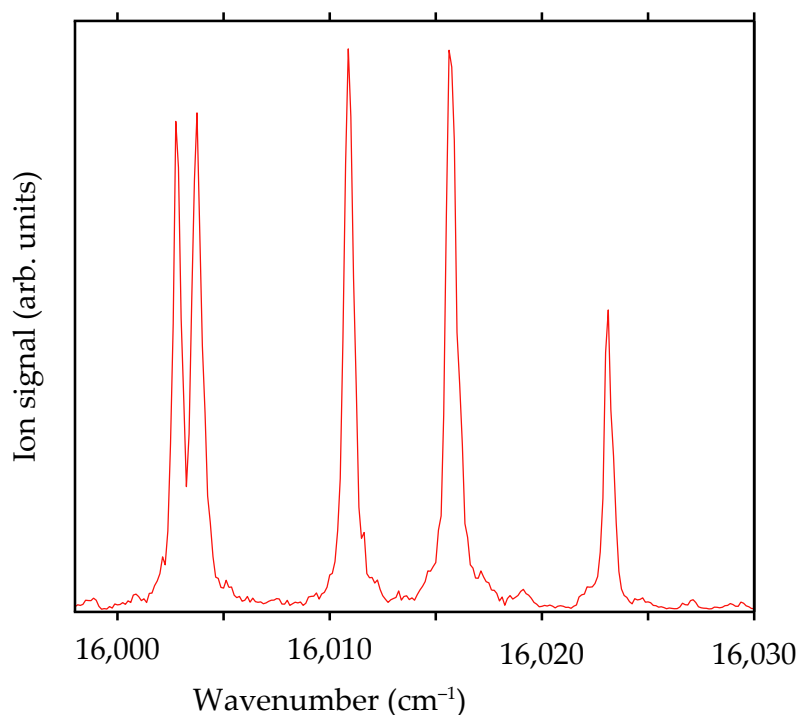


Figure 3.5: Rotationally resolved 2+1-REMPI spectrum for $^{14}\text{NH}_3$ obtained behind the Stark decelerator, with the Stark decelerator on. The 2+1-REMPI channel is the $|X, v_2 = 0\rangle \rightarrow |B, v_2 = 5\rangle$ transition, and the molecule's initial level is the $|J, K\rangle = |1, 1\rangle$ state. All peaks originate from the low-field-seeking upper inversion doublet.

Pyromethene 597 would be used instead of DCM. In order to test the detection efficiency for the application of motion manipulation experiments to 4-aminobenzonitrile, the 2+1-REMPI spectrum was recorded in the range from 290 to 300 nm (Fig. 3.6). The frequency was increased in steps of 0.01 nm, and for each point 180 acquisitions were averaged. Line positions were determined by fitting a Lorentzian line shape to each peak [134].

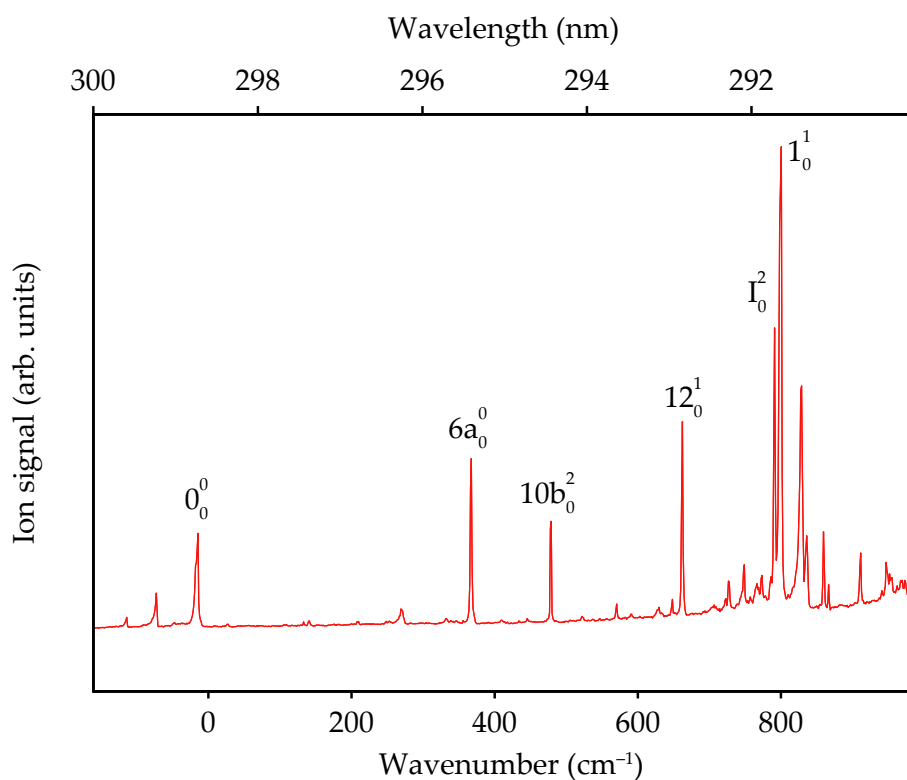


Figure 3.6: 2+1-REMPI spectrum of 4-aminobenzonitrile. The different lines represent resonances of different vibrational levels for the same excited electronic level. Here, the origin is set to the known value of 33 493 cm⁻¹ to conform with the line assignment presented in other studies that use the Varsányi notation [131–133].

3.2 Chirped-pulse Fourier transform microwave spectrometer

Molecular rotational spectroscopy is one of the most powerful methods for obtaining rotationally resolved spectra. The technique itself is widely applicable, and its only requirements are that the molecule under investigation is polar and in the gas phase. Chirped-pulse Fourier transform microwave (CP-FTMW) spectroscopy is a fast, robust and sensitive technique [13]. The CP-FTMW spectrometer (COMPACT) employed throughout this thesis belongs to a new generation of spectrometers, which have been aided in their development by the advancement of high-speed digital electronics [15, 135]. These advancements generally simplify the experimental set-up of CP-FTMW spectrometers, especially for those operating at lower frequencies.

The COMPACT spectrometer covers a frequency range from 2-8.5 GHz, and has recently been extended to 14 GHz. In this set-up, a broadband microwave chirp pulse is generated using an 8-bit, 24 Gs/s arbitrary waveform generator (Tektronix AWG 7122B with channel interleave). The microwave excitation chirp produced is amplified by an adjustable travelling wave tube (TWT) amplifier (Amplifer Research 300T2G8) and then coupled to the vacuum chamber using a microwave cable. According to specifications, the TWT amplifier generates a maximum output power between 300 W at the edge of the frequency band to 600 W in the center (depending upon the specific microwave frequency). Horn antenna (Q-Par Angus WBH 2-18-NHG), with a high gain and high directionality, broadcast the microwave chirp into the vacuum chamber where it interacts with a sample of supersonically expanded, internally cold molecules. A second horn antenna is used as the receiver. Supersonic expansion of the molecular sample is achieved with a pulsed nozzle (Parker General Valve, Series 9) in an arrangement perpendicular to the horn antennae.

Outside of the vacuum chamber a high power PIN diode limiter (Advanced Control Components) followed by a PIN diode switch (ATM Microwave) with 20 ns rise and fall times protect the low-noise amplifier (LNA) and the digital oscilloscope from the amplified excitation pulse. Polarization of the sample is achieved via excitation, and a macroscopic dipole moment is formed when the molecules are

resonant with a frequency within the chirp. The resulting free induction decay (FID), or the coherent molecular emission, is amplified and then digitized using an 8-bit, 25 Gs/s digital oscilloscope (Tektronix DPO 73304D). A delay generator (Stanford Research Systems Model DG645) provides the triggers for the valve driver, AWG, oscilloscope and the protection switch. Thus the delay generator controls the opening time of the valve and the expansion time of gas, as well as ensuring the protection switch protects the detection side of the spectrometer during the excitation process. The delay generator, oscilloscope and AWG are

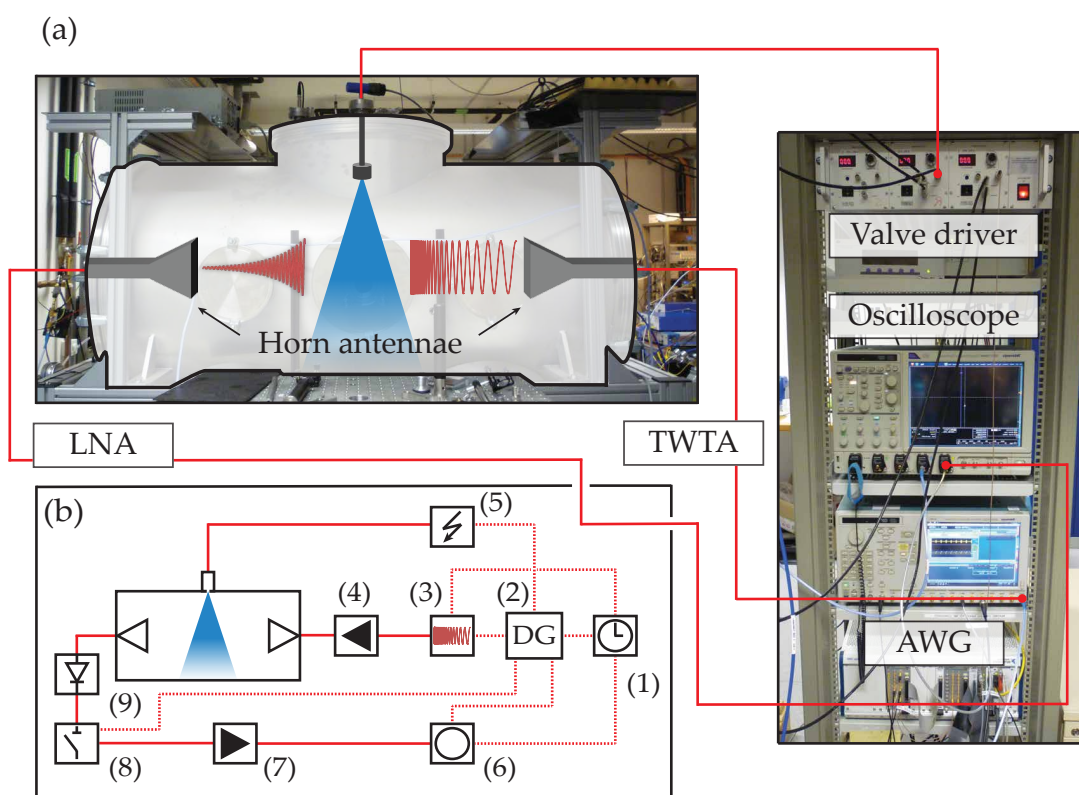


Figure 3.7: Experimental set-up of the COMPACT spectrometer. (a) relatively accurate representation of the experimental set-up in the laboratory. (b) More detailed schematic of the experimental set-up: (1) Rb-frequency standard, (2) delay generator, (3) arbitrary waveform generator (AWG), (4) travelling wave tube amplifier (TWTA), (5) valve driver, (6) oscilloscope, (7) low noise amplifier, (8) protection switch, (9) pin-diode limiter.

also connected to a Rb-frequency standard clock to synchronize their phases. As the digitizer is triggered with a marker channel of the AWG, synchronous pulse-to-pulse operation is achieved allowing for time domain signal averaging. Refer to Figure 3.7 for a depiction of how each of these components connect to one another. Phase stability allows for averaging high numbers of acquisitions in the time domain increasing the sensitivity of the instrument. To obtain a spectrum in the time domain a Fourier transformation is performed. The length of the recorded FID determines the resolution of the rotational spectrum obtained. A length of $40\ \mu\text{s}$ produces, after Fourier transformation, a spectrum with a 25 kHz resolution.

A recent development to the COMPACT spectrometer is the incorporation of the ‘fast frame’ approach [15]. This data acquisition scheme is an option made available by the digital oscilloscope and is an example of how this technique benefits from the advancement of digital electronics. Essentially for each pulse of sample, eight back-to-back excitation chirps are performed and each of the consequential FID acquisitions are co-added and then averaged. This scheme can drastically decrease measurement time and sample consumption. For example, over a 24 hour measurement using a repetition rate of 9 Hz a total of approximately 6.2 million acquisitions can be achieved, which is often sufficient for the observation of a molecule’s singly substituted isotopologues in their natural abundance, foremost ^{13}C , ^{15}N , and ^{18}O . Analysis of the spectra measured for each isotopologue in their natural abundance allows for the determination of molecular structure via isotopic substitution, or alternatively a least-squares fitting approach.

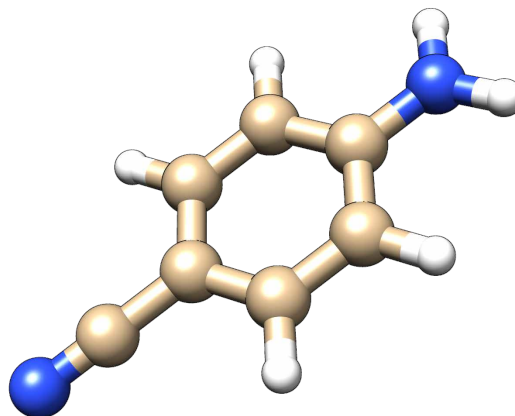
3.2.1 Methods for structural determination

Determination of molecular structure using rotational spectroscopy is an essential tool for chemistry and has displayed unique capabilities when applied to conformational flexibility [136] and molecular clusters [137]. This capability of rotational spectroscopy moves the technique beyond a simple molecular identification tool. The high resolution and sensitivity provided by CP-FTMW spectroscopy means that rotational constants can be obtained for singly substituted ^{13}C , ^{15}N and ^{18}O isotopologues in their natural abundances (1.1%, 0.36% and 0.21%, respectively). With this information, the structure of a molecule in the gas phase can be deter-

mined experimentally, and in principle without the need for any prior knowledge.

Molecular structure can be obtained via the isotopic variation of the rotational constants, which depends upon an atom's position within the principal axis frame. Consequently, an experimental structure can be built one atom at a time, on the basis of single isotopic substitutions. This approach is referred to as the substitution, r_s , method and relies on the Kraitchman equations [14]. Limitations of this method become apparent when attempting to determine small coordinates in the principal axis system, i.e., positions that lie close to a principal axis of the molecule. In this case, rovibrational contributions to the measured ground state rotational constants interfere and can result in imaginary coordinates. To address these issues other methods that determine the molecular structure from the isotopic data have also been developed.

An effective ground state, r_0 , structure can be obtained by fitting structural parameters in a least-squares fitting manner to reproduce the experimentally determined ground-state rotational constants for each isotopologue. Structural changes brought about by isotopic substitution are neglected, which results in deviations of the effective structure from the equilibrium (r_e) structure. The least-squares fitting method can be developed further by scaling a molecule's moments of inertia according to the change in mass upon substitution. Watson et al. [138] discuss several of the most successful models that yield equilibrium quality structures from ground-state experimental data, denoted $r_m^{(1)}$, $r_m^{(1L)}$, $r_m^{(2)}$, and $r_m^{(2L)}$. Mass-dependent structures can still show distortions when applied to coordinates close to the principal axes, both the $r_m^{(2)}$ and $r_m^{(2L)}$ models are expected to better account for this effect. Additionally, large isotopic effects on deuterium substitution can be better accounted for with the $r_m^{(1L)}$, which introduces extra adjustable parameters for each deuterated bond. The simplest $r_m^{(1)}$ method produces results that can be directly compared to those obtained from the r_s method, as well as the r_e values obtained computationally. It is important to note that r_e structure produces equilibrium internuclear distances from hypothetically vibrationless nuclei, which is unrealistic for any molecule, reinforcing the need for experimentally determined structures.



Chapter 4

Aminobenzonitrile*

4-Aminobenzonitrile (4-ABN) is a polyatomic asymmetric molecule with a large permanent dipole moment, $\mu_{\text{perm}} = 6.9\text{D}$, which is one of the largest dipole moments predicted of all the molecules investigated in this thesis. It consists of two substituents, an amino (NH_2) group and a nitrile (CN) group, bonded to a benzene ring in a *para* arrangement. The total dipole moment of a polyatomic molecule can be estimated by adding the dipole moments of polar bonds together. According to this logic, the total dipole moment of 4-ABN could be determined from the addition of the total dipole moments of aniline and benzonitrile. Where the aniline molecule consists of a benzene ring bonded to an amino group, and benzonitrile consists of a benzene ring bonded to a nitrile group. However, Borst et al. [139] determined experimentally that this was not the case for 4-ABN, and rationalised that charge transfer enhanced the total dipole moment resulting in the observed non-additivity. The large dipole moment of 4-ABN is thus a consequence of the combined electron-donating and withdrawing behaviour of the amino and the nitrile group, respectively. Together with its large polarity, the ease of which 4-ABN can be seeded into a molecular beam makes it a viable candidate for motion manipulation experiments with AC-electric fields. In order to apply such techniques to a large molecule, like 4-ABN, it is advantageous to have a detailed knowledge

*This chapter is based on the following publications: T. Betz, S. Zinn, J. B. Graneek, and M. Schnell, *Nuclear quadrupole coupling constants of two chemically distinct nitrogen atoms in 4-aminobenzonitrile*, J. Phys. Chem. A. **118**, 5164–5169 (2014), and J. B. Graneek, S. Merz, D. Patterson, T. Betz, and M. Schnell, *Simulating spatial microwave manipulation of polyatomic asymmetric-top molecules using a multi-level approach*, ChemPhysChem. **17**, 3624-3630 (2016).

of its rotational energy level structure. This information can be obtained from the analysis of a molecule’s rotational spectrum. In this chapter, 4-ABN is the focus of two different investigations; a spectroscopic and a motion manipulation study.

4.1 Structural determination of 4-aminobenzonitrile

The rotational spectrum of 4-ABN in the frequency range of 2–8.5 GHz was first measured by our group in 2014 [134]. This measurement was carried out using the same chirped-pulse Fourier transform technique discussed earlier in Section 3.2, but utilised a somewhat different molecular beam arrangement, referred to as the ‘BEAMSPEC’ instrument, resulting in a lower sensitivity. The different molecular beam arrangement also incorporated a time-of-flight (TOF) ion mass spectrometer into the set-up. The resolution and sensitivity obtained were still sufficient to determine the quadrupole coupling constants due to the two chemically distinct nitrogen atoms of 4-ABN. For more information regarding the BEAMSPEC set-up see Reference [134].

This work was the first step towards identifying 4-ABN as a good candidate for the motion manipulation study (Section 4.2). It not only provided a rotational spectrum, thus information on the rotational energy levels, but also a 2+1-REMPI spectrum (Fig. 3.6) intrinsic to the detection of 4-ABN for the potential motion manipulation experiments. The spectroscopic results reported in 2014 [134] are also included in this chapter and compared with the updated spectroscopic parameters obtained using the COMPACT spectrometer. The improved sensitivity provided by the COMPACT spectrometer allowed for the assignment of almost twice as many lines of the parent molecule and the observation of ^{13}C and ^{15}N isotopologues in their natural abundance.

4.1.1 Experimental

The broadband rotational spectrum of 4-ABN was recorded using the COMPACT spectrometer, a detailed description of the set-up can be found in Section 3.2. A sample of 4-ABN was purchased from Sigma-Aldrich (98% purity) and used without further purification. The sample was placed within the reservoir of the nozzle

and heated to approximately 113 °C. Using neon as a carrier gas, at a backing pressure of 2.5 bar, the mixture was supersonically expanded into the vacuum chamber via the pulsed nozzle at repetition rate of 4 Hz. After supersonic expansion, the ensemble was excited by a 4 μ s long microwave chirp spanning 2–8 GHz, which was amplified by the TWT amplifier set to 100% gain. The molecular response in the form of an FID was recorded for 40 μ s resulting in a spectral resolution of 25 kHz. In total two million FIDs were co-added and Fourier transformed to produce a rotational spectrum with a signal-to-noise ratio of approximately 900:1. Such a signal-to-noise ratio is usually sufficient for the observation of isotopologues in their natural abundance, facilitating the determination of 4-ABN's molecular structure.

4.1.2 Results and discussion

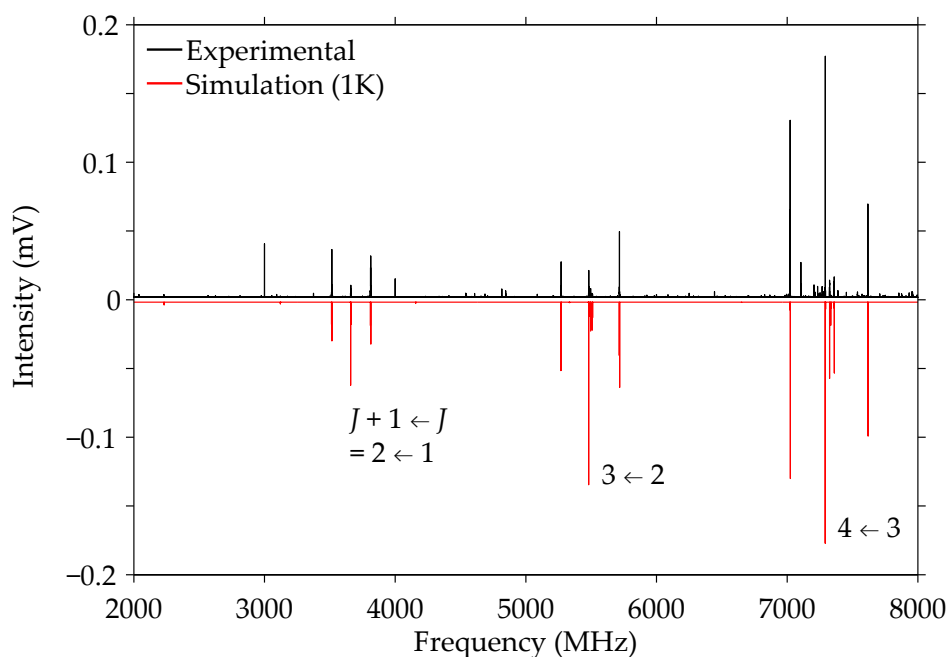


Figure 4.1: Rotational spectrum of 4-aminobenzonitrile. The lower trace represents a simulation of the fitted spectroscopic parameters reported in Table 4.1.

The broadband rotational spectrum obtained for 4-ABN and the corresponding fit is displayed in Figure 4.1. Structure optimization calculations were carried out in Gaussian09 [140] using the aug-cc-pVTZ basis set with the B3LYP hybrid functional including and excluding Grimme’s empirical dispersion. The experimental and calculated spectroscopic parameters of 4-ABN obtained, including the nuclear quadrupole coupling components, are listed in Table 4.1, along with those obtained using the BEAMSPEC instrument [134]. At first glance, the spectroscopic parameters determined experimentally using the different spectrometers are relatively similar. The improved sensitivity obtained with the COMPACT spectrometer does, however, allow for the assignment of many more lines, which results in reduced errors for each of the determined parameters. In total 227 lines were assigned for the parent molecule with an average error of the fit of 5.6 kHz.

Table 4.1: Spectroscopic constants of 4-ABN determined experimentally with the COMPACT, compared with those obtained with the BEAMSPEC spectrometer [134] and via quantum-chemical calculations. Here N_{11} refers to the nitrogen atom of the amino group and N_{15} to the nitrogen atom of the nitrile group.

Parameter	COMPACT	BEAMSPEC Ref. [134]	B3LYP/ aug-cc-pVTZ	B3LYP(GD3BJ)/ aug-cc-pVTZ
A [MHz]	5580.2(2)	5581.0(4)	5623.66	5625.40
B [MHz]	990.36061(7)	990.3717(7)	994.26	996.25
C [MHz]	841.48433(7)	841.4827(6)	845.26	846.74
χ_{aa} (N_{11}) [MHz]	2.472(3)	2.48(1)	2.5034	2.4872
χ_{bb-cc} (N_{11}) [MHz]	6.189(4)	6.22(2)	6.6618	6.6444
χ_{aa} (N_{15}) [MHz]	-4.143(2)	-4.138(9)	-4.5699	-4.5720
χ_{bb-cc} (N_{15}) [MHz]	0.650(5)	0.66(2)	0.8611	0.8618
$\mu_a/\mu_b/\mu_c$ [D]	6.86/0/0.74	6.84/0/0.75
N_{lines}	227	114
σ [kHz]	5.6	11.64

The assignment of the strong a -type transitions clearly visible within the spectrum was performed with the program PGOPHER [119]. Rotational quantum numbers involved in the assigned transitions range from $J = 1$ up to $J = 7$. After assignment, the determined rotational parameters can be directly compared to those obtained via quantum-chemical calculations (Table 4.1).

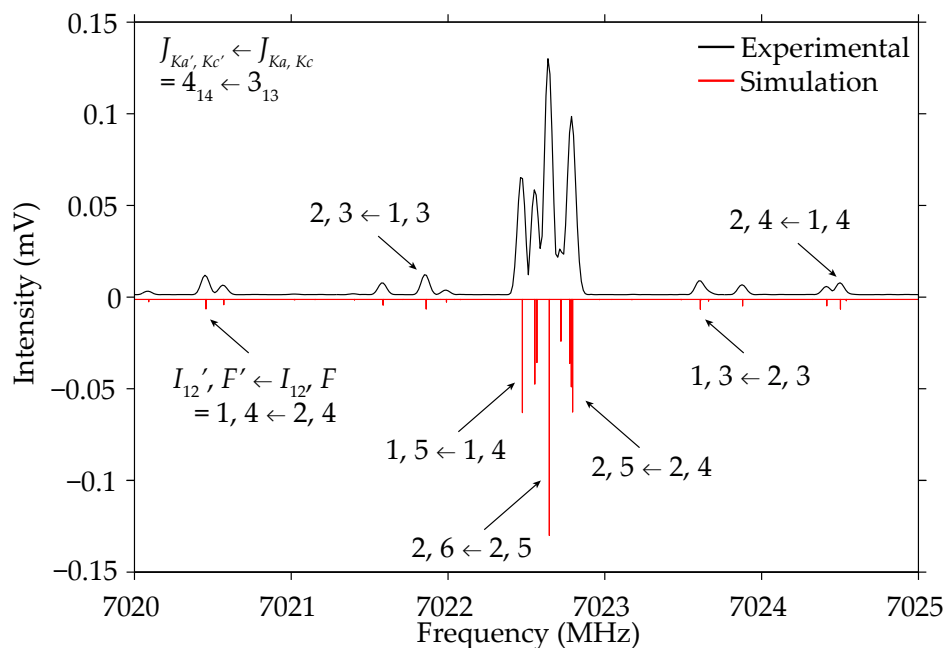


Figure 4.2: Nuclear quadrupole coupling splitting due to the N_{11} and N_{15} atoms of 4-ABN. The F quantum numbers for the $J'_{Ka', Kc'} \leftarrow J_{Ka, Kc} = 4_{14} \leftarrow 3_{13}$ transition are also displayed.

The molecule 4-ABN has also been investigated using rotationally resolved electronic spectroscopy [139] and laser-induced fluorescence (LIF) spectroscopy [141]. Each study concludes that an angle between the plane of the benzene ring and the plane of the amino group exists for 4-ABN, similar to that observed for aniline ($C_6H_5NH_2$) [142]. This inversion angle was determined to be 37° – 44° for aniline [142–144] and is expected to reduce by approximately 6° for 4-ABN [141]. Heine et al. [145] determined the structure of 4-ABN in the crystalline form at 153 K and observe an inversion angle of $34(3)^\circ$. The out-of-plane hydrogen atoms of the amino group should result in a non-zero dipole moment component μ_c for

4-ABN, and therefore observable c -type transitions in the broadband rotational spectrum. Borst et al. [139] predict a μ_c dipole moment component as large as 1.45 D. However, the results obtained in this investigation indicate this to be a rather large overestimation.

Both sets of calculations that employ the B3LYP hybrid functional including and excluding Grimme’s empirical dispersion predict a non-planar structure with inertial defects ($\Delta = I_c - I_a - I_b$) of $-0.26 \mu\text{\AA}^2$ and $-0.27 \mu\text{\AA}^2$, respectively. Calculations including Grimme’s empirical dispersion generally produce rotational parameters closer to those determined experimentally, and are thus the focus of the following discussion. The inversion angle determined for the B3LYP(GD3BJ) structure is 20.2° . To determine this angle using experimental data was not possible as deuterium has a very low natural abundance of 0.015%. Consequently, singly substituted D isotopologues were not observed in the spectrum.

Irrespective of the splitting that would arise from the inversion of the amino group and the predicted non-zero μ_c of 0.75 D, no c -type transitions have been assigned in the recorded spectrum. However, the experimentally determined rotational constants still indicate a non-planar structure with an inertial defect of $-0.3 \mu\text{\AA}^2$, similar to the calculated values. A negative contribution to the inertial defect is typical for molecules that display out-of-plane motions. The absence of c -type transitions in the rotational spectrum of 4-ABN has been previously rationalized by the cold conditions brought about by supersonic expansion [134]. Similarly to aniline [142], the splittings of energy levels caused by inversion of the amino group are so large that the thermal population of the excited modes are negligible at low temperatures. It is also likely that a significantly smaller μ_c dipole moment component and inversion angle to those reported previously in References [139] and [141], respectively, would contribute to the absence of c -type transitions in the rotational spectrum of 4-ABN.

The presence of nitrogen atoms in 4-ABN results in an observable hyperfine structure (Fig. 4.2), caused by the coupling of nitrogen’s nuclear charge density with the electric potential generated by electrons and other nuclei. As mentioned earlier in Section 2.2, the hyperfine structure is further complicated when a molecule possesses more than one strongly coupling nucleus. Quadrupole coupling nuclei are generally considered equivalent when they have the same, or compara-

ble coupling strength. This is the case of 4-ABN, where the quadrupole coupling nuclei present are both nitrogen atoms and the nuclear spin $I(^{14}\text{N}) = 1$. The most convenient scheme to describe this coupling interaction is the $(I_1 I_2 I_{12} J F M_F)$ representation [146], which combines the spins of each quadrupole coupling nuclei before coupling with molecular rotational angular momentum \mathbf{J} . In this case, the new angular momentum quantum numbers are:

$$\begin{aligned} I_{12} &= I_1 + I_2, \\ F &= J + I_{12} \end{aligned}$$

where F is the new quantum number for the total angular momentum of 4-ABN. A detailed look at the hyperfine structure for the $J'_{K'a',Kc'} \leftarrow J_{Ka,Kc} = 4_{14} \leftarrow 3_{13}$ transition and the quantum numbers involved can be found in Figure 4.2.

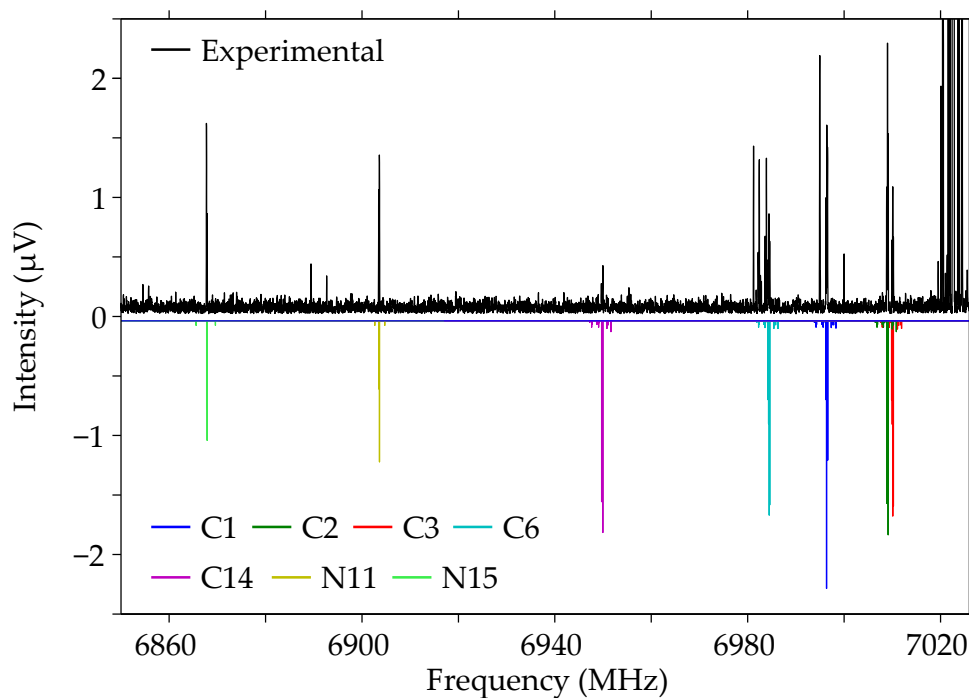


Figure 4.3: Satellite lines of singly substituted ^{13}C and ^{15}N isotopologues of 4-ABN for the $J'_{K'a',Kc'} \leftarrow J_{Ka,Kc} = 4_{14} \leftarrow 3_{13}$ transition. Although the C_{14} signal intensity is particularly weak in this example, this is not the case for every transition within the spectrum. This transition was chosen as it displays lines for each of the respective isotopologues within a convenient frequency range.

The closeness of the nuclear quadrupole coupling constants determined with the COMPACT spectrometer compared to those determined with the BEAMSPEC spectrometer reinforces the conclusions made in the original 4-ABN investigation [134]. This study compared the nuclear quadrupole coupling constants deter-

Table 4.2: Rotational constants determined from the assignment for each isotopologue of 4-ABN. Also included are the number of lines assigned for each isotopologue (N_{lines}) and the average error of the assignments (σ).

Parameter	Parent	C ₁	C ₂	C ₃
A [MHz]	5580.2(2)	5492.3(2)	5492.1(2)	5580.1(2)
B [MHz]	990.36061(7)	988.1718(5)	990.1813(4)	988.3610(4)
C [MHz]	841.48433(7)	837.8843(4)	839.3223(4)	840.0476(4)
χ_{aa} (N ₁₁) [MHz]	2.472(3)	2.471(5)	2.502(8)	2.43(1)
χ_{bb-cc} (N ₁₁) [MHz]	6.189(4)	6.23(4)	6.20(2)	6.06(3)
χ_{aa} (N ₁₅) [MHz]	-4.143(2)	-4.149(5)	-4.152(6)	-4.13(1)
χ_{bb-cc} (N ₁₅) [MHz]	0.650(5)	0.62(2)	0.67(2)	0.76(3)
N_{lines}	227	51	59	35
σ [kHz]	5.6	4.4	5.0	3.5
Parameter	C ₆	C ₁₄	N ₁₁	N ₁₅
A [MHz]	5580.7(2)	5580.9(5)	5580.8(8)	5580.5(7)
B [MHz]	984.2951(4)	978.8252(5)	971.5101(7)	965.8673(6)
C [MHz]	837.1072(3)	833.1398(4)	827.8358(8)	823.7345(6)
χ_{aa} (N ₁₁) [MHz]	2.43(2)	2.37(2)	...	2.49(2)
χ_{bb-cc} (N ₁₁) [MHz]	6.189(4)	6.23(4)	...	6.2(3)
χ_{aa} (N ₁₅) [MHz]	-4.17(2)	-4.26(2)	-4.26(4)	...
χ_{bb-cc} (N ₁₅) [MHz]	0.50(4)	0.8(1)	1.4(5)	...
N_{lines}	28	27	14	18
σ [kHz]	3.0	3.8	4.6	4.6

mined for 4-ABN with those reported for dimethylaminobenzonitrile (DMABN), dimethylaniline (DMA), aniline [147], and benzonitrile (BN) [148]. It was concluded that the electron-donating character of the dimethylamino ($(\text{CH}_3)_2\text{N}$) and amino groups of DMABN and ABN, respectively, have an observable effect on the nuclear quadrupole coupling constants of their respective nitrile N atoms, made especially obvious when compared to the nuclear quadrupole coupling constants of BN. In addition, the absence of electron-donating methyl groups in ABN means that the quadrupole coupling constants of the amino group N atom are more comparable to those of aniline rather than DMABN and DMA.

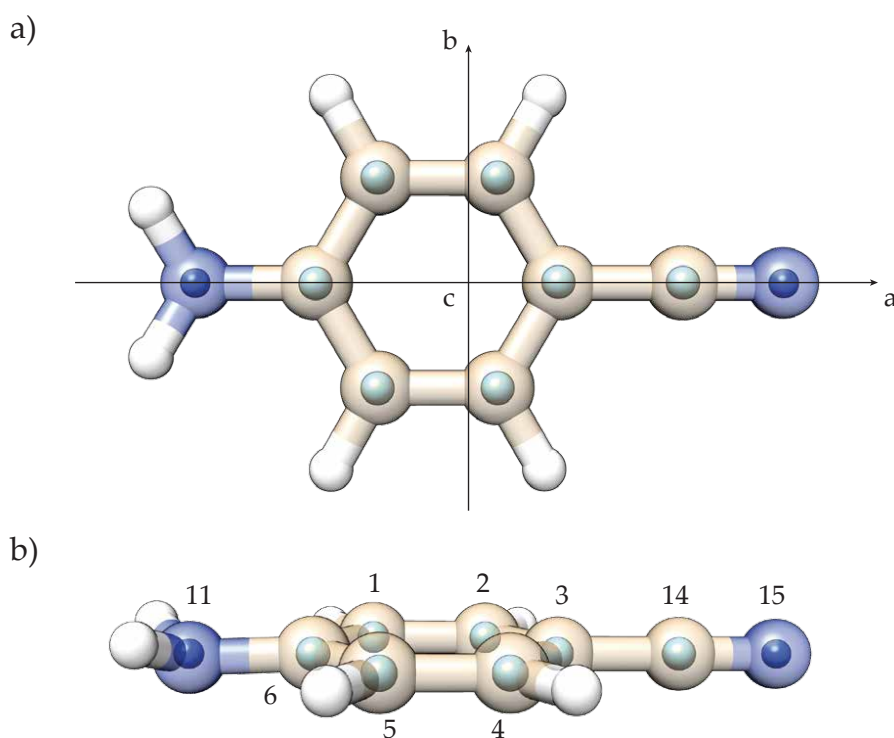


Figure 4.4: Comparison of the calculated (background) and the experimentally determined (foreground, spheres) atom positions, excluding hydrogen. Calculated atom positions obtained via B3LYP(GD3BJ)/aug-cc-pVTZ calculations. Experimental atom positions determined via a mass-dependent least-squares fit ($r_m^{(1)}$ -structure) approach. A reference to the inertial axis frame is included in (a) and atoms labels are included in (b). The inversion angle between the plane of the amino group and the plane of the benzene ring is clearly visible in (b).

The high sensitivity of the COMPACT spectrometer allows for the observation of singly substituted ^{13}C and ^{15}N isotopologues of 4-ABN in their natural abundance. Lines for these isotopologues assigned to the $J'_{K'a',Kc'} \leftarrow J_{Ka,Kc} = 4_{14} \leftarrow 3_{13}$ transition are displayed in Fig. 4.3. The number of lines assigned and the rotational constants derived from the fits for each isotopologue are summarized in Table 4.2. A mass-dependent least-squares fit of the structure to the rotational constants, as well as an additional parameter ($c_a = 0.0297(3) \mu^{1/2} \text{\AA}$), was performed with the STRFIT program [149]. The information obtained for the isotopologues is also sufficient to determine a substitution structure using Kraitchman's equations [14]. As discussed in Section 3.2.1, the substitution approach is not always effective for coordinates that lie close to an inertial axis. This complicates structure determination of 4-ABN using this method as most of 4-ABN's atoms lie close to, or directly on an inertial axis (see Figure 4.4(a)). The majority of the atom positions obtained via this approach yielded imaginary components and are consequently not

Table 4.3: Experimentally determined and calculated bond lengths of 4-ABN: $r_m^{(1)}$ -structure (mass-dependent least-squares fit), and r_e -structures determined using the aug-cc-pVTZ basis set with the B3LYP hybrid functional including and excluding Grimme's empirical dispersion.

Bond lengths	$r_m^{(1)}$ (\AA)	B3LYP	B3LYP(GD3BJ)
		r_e (\AA)	r_e (\AA)
C ₁ –C ₂	1.384(5)	1.380	1.380
C ₂ –C ₃	1.406(4)	1.400	1.400
C ₃ –C ₄	1.387(4)	1.400	1.400
C ₄ –C ₅	1.384(5)	1.381	1.380
C ₅ –C ₆	1.410(2)	1.403	1.402
C ₆ –C ₁	1.401(2)	1.403	1.402
C ₆ –N ₁₁	1.387(1)	1.380	1.379
N ₁₁ –H	...	1.005	1.005
C ₃ –C ₁₄	1.440(2)	1.425	1.424
C ₁₄ –N ₁₅	1.159(1)	1.154	1.153

reported here. The mass-dependent least-squares method yields the $r_m^{(1)}$ geometry, which is generally less susceptible to the same effects, such as the position of an atom with respect to the inertial axes, that reduce the accuracy of a determined substitution structure.

A direct comparison of the structural parameters determined experimentally to those obtained via quantum chemical calculations is given in Tables 4.3 and 4.4. The quantum chemical calculations provide a hypothetical equilibrium structure (r_e) at a potential energy minimum without zero-point energy vibration. Including or excluding Grimme’s empirical dispersion results in only minor changes to the structural parameters calculated. As mentioned earlier, the atom positions of the hydrogen atoms could not be determined experimentally as the natural abundance of deuterium (0.015%) is insufficient to observe lines within the spectrum. Consequently, structural parameters relating to the amino group can only be compared

Table 4.4: Experimentally determined and calculated bond angles of 4-ABN: $r_m^{(1)}$ -structure (mass-dependent least-squares fit), and r_e -structures determined using the aug-cc-pVTZ basis set with the B3LYP hybrid functional including and excluding Grimme’s empirical dispersion.

Bond angles	$r_m^{(1)}$ ($^\circ$)	B3LYP	B3LYP(GD3BJ)
		r_e ($^\circ$)	r_e ($^\circ$)
$\angle C_1C_2C_3$	119.9(2)	120.7	120.6
$\angle C_2C_3C_4$	119.8(3)	118.7	118.9
$\angle C_3C_4C_5$	120.4(2)	120.7	120.6
$\angle C_4C_5C_6$	120.4(1)	120.7	120.6
$\angle C_5C_6C_1$	118.9(1)	118.4	118.6
$\angle C_6C_1C_2$	120.6(1)	120.7	120.7
$\angle C_1C_6N_{11}$	120.8(1)	120.8	120.7
$\angle NH_2(\text{inv})$...	19.99	20.19
$\angle C_4C_3C_{14}$	120.7(2)	120.7	120.6
$\angle C_3C_{14}N_{15}$	179.97(6)	180.0	180.0

between the alternative quantum chemical approaches. Figure 4.4(b) shows a side view of 4-ABN where the inversion angle is much more noticeable. To determine an experimental value for the amino group's inversion angle via CP-FTMW spectroscopy it would be necessary to work with a deuterated form 4-ABN. However, as this would involve a change in mass of 100% the assumption that the structure does not change might not hold here, complicating analysis.

Information derived from the analysis of 4-ABN's rotational spectrum is essential for the development of potential deceleration, focusing or trapping experiments. A detailed knowledge of a system's rotational energy level structure allows for a better understanding of how such states interact with one another in an inhomogeneous electric field. The physical structure is also relevant, as the dipole moment determines the force a molecule experiences when exposed to an electric field, and the different dipole moment components determine which selection rules are applicable. This is discussed in more detail in the following section.

4.2 Motion manipulation

Over the last 15 years a number of techniques have been developed to control the internal and external degrees of freedom for small, polar molecules using external electric, magnetic or electromagnetic fields (refer to Section 1.2.4). With increasing molecule size and decreasing molecular symmetry, the number of non-degenerate rotational states and thus their density increases dramatically. Due to this high density of states, the majority of rotational states for such a system would be high-field seeking at typical electric field strengths used in Stark deceleration and trapping experiments (≥ 100 kV/cm). In 2004 a microwave trap for confining diatomic molecules in high-field-seeking states [88] was proposed. A proposal for a microwave decelerator based on a similar design followed soon after in 2005 [89]. Tailored microwave fields can be generated using high-quality microwave resonators with field maxima on the molecular beam axis. Such an experimental set-up can then be used to decelerate and focus molecules in high-field-seeking states. Focusing, guiding, and deceleration of polar molecules in high-field-seeking states using cylindrically symmetric microwave resonators and internally cold and slow packets of ammonia molecules has already been reported [90–92]. Additionally, microwave

focusing has been extended to acetonitrile (CH_3CN) using a counter-rotating nozzle and cylindrically symmetric resonator of a similar design [93]. Both ammonia and acetonitrile are treated as two-level systems for these experiments, see Section 3.1.2 for more detail. For the application of microwave focusing and guiding to 4-ABN this two-level approximation is no longer helpful.

4.2.1 Numerical approach

The interaction of a molecule with a microwave field is described by the AC-Stark effect (see Section 3.1.2). A microwave field perturbs the rotational states of a molecule resulting in energy shifts. The magnitude of these shifts depends upon the detuning of the microwave radiation from a molecular resonance, as well as the electric field strength. Consequently, an inhomogeneous microwave field can exert a force on a molecule. This force is essential to achieve microwave motion control, such as focusing, guiding, and deceleration. To determine the feasibility of extending such microwave manipulation techniques to 4-ABN, the dressed-state formalism [127, 128] has been incorporated into a numerical approach. This enables the calculation of AC-Stark shifts for a multi-level system.

Matrix formation and diagonalization

For a multi-level system, calculation of the AC-Stark shift is complicated by a high density of rotational states. As previously discussed in Section 3.1.2, the Hamiltonian for a multi-level system within the dressed-state approach can be

written in a block-by-block extended way similar to Eq. 4.1:

$$\mathcal{H} = \left(\begin{array}{ccc|ccc} E_0 + mh\nu & 0 & \cdots & 0 & \cdots & 0 \\ 0 & \ddots & 0 & \Omega_{n,n'} & 0 & \vdots \\ \vdots & 0 & E_N + mh\nu & \Omega_{n,n'} & \Omega_{n,n'} & 0 \\ \hline 0 & \Omega_{n',n} & \Omega_{n',n} & E_0 + (m+1)h\nu & 0 & \cdots \\ \vdots & 0 & \Omega_{n',n} & 0 & \ddots & 0 \\ 0 & \cdots & 0 & \vdots & 0 & E_N + (m+1)h\nu \end{array} \right) \quad (4.1)$$

E_0 to E_N are the field-free rotational energy levels. These values can be calculated using methods described in rotational spectroscopy textbooks [111, 121], but in this case they were extracted from PGOPHER [119] after having fit the rotational spectrum of 4-ABN. The rotational energy levels extracted range from $J = 0$ up to 15 and include all K and M sublevels. As discussed in Section 4.1.2 nuclear quadrupole coupling causes further splitting of 4-ABN's energy levels. However, at large electric field strengths the split F states generally display the same behaviour as the J state without considering the nuclear quadrupole hyperfine coupling. To simplify calculations and reduce the size of the overall matrix, the hyperfine splitting is omitted.

The field-free rotational states E_n ($n = 0, 1, 2, \dots, N$), when dressed with a microwave field $mh\nu$, form the diagonal for the first block in the dressed-state matrix. The next block along the diagonal includes the same rotational energy levels dressed with a field where the photon number m is increased by one. In order to prevent losses from unwanted transitions the microwave frequency is detuned from a selected rotational transition. The narrow rotational transitions allow for small detunings, so that values of $\Delta \approx \pm 50$ MHz are typically chosen. Only two dressed rotational energy level systems, or 'ladders', are considered here: $E_{0,1,2,\dots,N} + mh\nu$ and $E_{0,1,2,\dots,N} + (m+1)h\nu$. The off-diagonal dipole moment matrix elements ($\Omega_{n,n'} = -\frac{1}{2}\mathcal{E}(\mu_z)_{n,n'}$) are determined using the selection rules for an asymmetric-top according to Table 3.1. These matrix elements couple the zero-order quasi-energy levels $E_n + mh\nu$ and $E_{n'} + (m+1)h\nu$. This essentially

introduces a new selection rule $\Delta m = \pm 1$. Thus coupling only occurs between rotational states that obey the selections rules of an asymmetric rotor, and are dressed by a difference of one microwave photon. Once complete, the matrix is diagonalized with increasing values of electric field strength and the shifted rotational energy levels are obtained.

Crossing/avoided-crossing

A consequence of increasing the complexity of the molecule is the increased occurrence of crossings and/or avoided crossings of the rotational states. For example, acetonitrile is a relatively small symmetric top molecule. Compared to 4-ABN, acetonitrile's large rotational constants ($A=158.4$ GHz, $B=C=9.204$ GHz) and higher symmetry results in a reduced density of states. Thus large electric field strengths are needed before rotational states might cross/avoid one another. Consequently, when applying a microwave field detuned from a transition of interest, acetonitrile can be treated as two-level system. When considering the AC-Stark effect on the rotational states of 4-ABN, crossing scenarios arise at electric field strengths as low as 1 kV/cm. See Figure 4.5 to gain some understanding of how the different molecule's rotational states interact with increasing electric field strength, and pay particular attention to the energy scale axis when comparing the density of rotational states.

Accurate predictions of AC-Stark shifts are complicated by the density of molecular energy levels. As the density increases, or when operating at large electric field strengths it can become increasingly tedious to interpret the results of potential crossing scenarios. So to better identify the respective zero-field rotational states at larger electric field strengths a second computer code was developed. This code labels the rotational states at zero-field using the appropriate quantum numbers and with increasing electric field strength recognises potential crossing scenarios. As two rotational states approach each other their respective state labels are adjusted depending on whether they cross or avoid one another. This outcome is determined by the electric dipole moment selection rules of the system, which for an asymmetric top are established according to the non-zero dipole moment components and the polarization of the external field. For 4-ABN

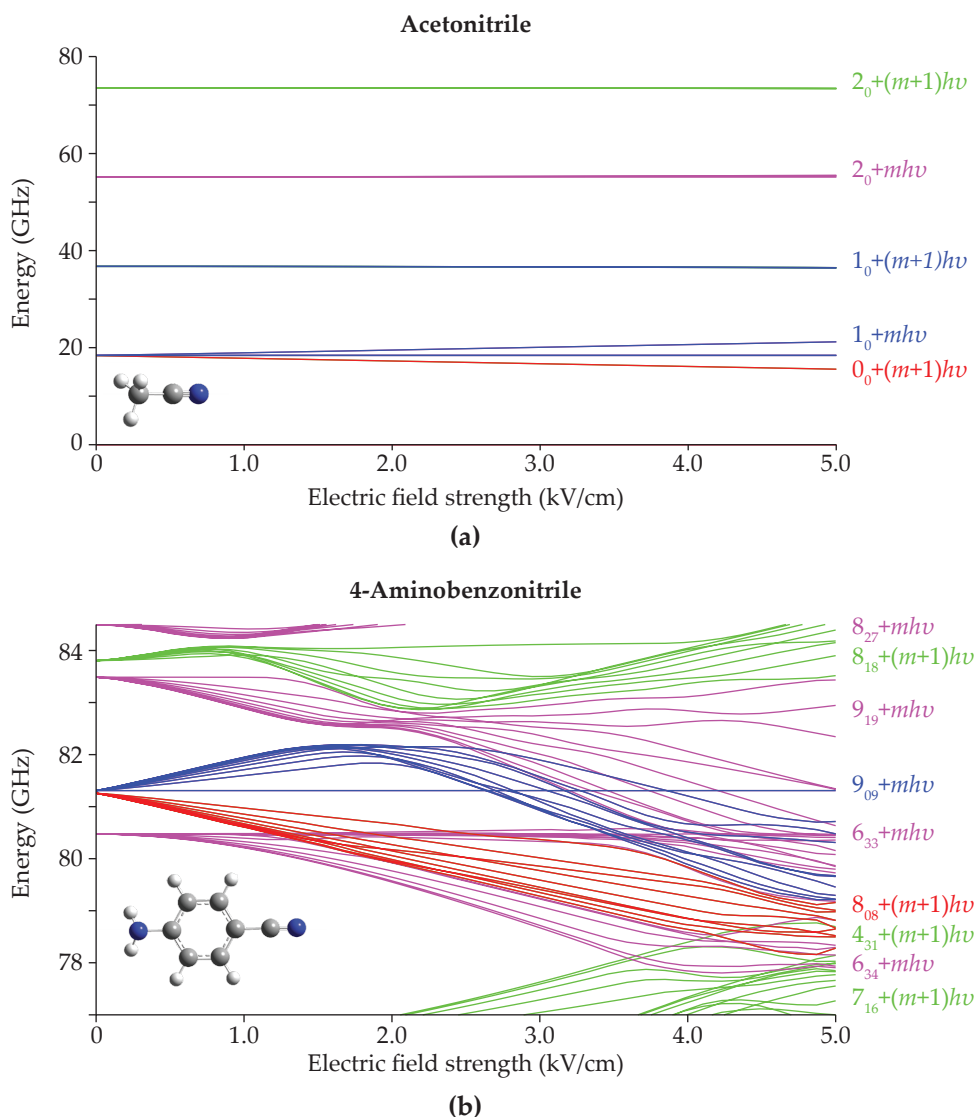


Figure 4.5: AC-Stark curves obtained from numerical calculations based on the dressed-state formalism. The applied MW field is red-detuned ($\Delta = -50$ MHz) from a selected rotational transition: (a) CH_3CN : $1_0 \leftarrow 0_0$ at 18 398 MHz (J_K notation). (b) 4-ABN: $9_{09} \leftarrow 8_{08}$ at 16 092 MHz ($J_{K_a K_c}$ notation). The red and blue lines correspond to the M manifold of rotational states dressed with m and $m + 1$ microwave photons, respectively, which are directly addressed by the microwave radiation. The purple and green lines correspond to the other rotational states within the manifolds dressed with m and $m + 1$ photons, respectively. Notably, there are different scales for the energy axes. For acetonitrile the y -axis spans 80 GHz, whereas the y -axis for 4-ABN covers approximately 7 GHz. The hyperfine structure due to the nuclear quadrupole coupling of nitrogen was omitted for both molecules.

$\Delta J = 0, \pm 1$, $\Delta K_a = 0, \pm 1$, $\Delta K_c = 0, \pm 1$, and using linearly polarized microwave radiation $\Delta M = 0$. An example of such a crossing scenario can be seen in Figure 4.5(b) at approximately 1 kV/cm. Here, the M substates of the $8_{08} + (m+1)h\nu$ approach those of the $6_{33} + mh\nu$ and the $6_{34} + mh\nu$ levels, and according to the selection rules these states cross.

In Reference [88], DeMille et al. discuss the application of circularly polarized light to polar diatomic molecules. When considering a dressed system with more than two ladders near-degenerate rotational states are inevitable. The use of circularly polarized light in this case reduces losses from avoided crossings by altering the M selection rule ($\Delta M = \pm 1$). This model was proposed to inhibit the ground state of a molecule from absorbing multiple microwave photons thus reducing the effective trap depth. For 4-ABN, only two ladders are considered in the calculations and the rotational state of interest is not the ground state, thus in this case linearly polarized radiation is preferred, and the $\Delta M = 0$ selection rule is still relevant.

4.2.2 Microwave manipulation simulations

For the microwave manipulation simulations the transition of interest is the $9_{09} \leftarrow 8_{08}$ at 16 092 MHz. The M manifold of the $8_{08} + (m+1)h\nu$ rotational state of 4-ABN is chosen for microwave focusing and guiding experiments. As can be seen from Figure 4.5(b), these states undergo reasonably large AC-Stark shifts in a microwave field close to the 16 GHz frequency range. This frequency range is beneficial for two main reasons. Firstly, strong microwave amplifiers are commercially available at this range. Secondly, $\lambda/2 \approx 10$ mm, which fits nicely to the size of a supersonically expanded molecular packet. Previous experiments with a molecular beam of ammonia were performed with maximum field strengths of up to 1.4 kV/cm [92]. These field strengths were obtained using input powers of 5 W and resonators with quality factors (Q) up to 10 000. The AC-Stark shifts calculated for the $8_{08} + (m+1)h\nu$ rotational states at a microwave frequency of 16 042 MHz suggest that electric field strengths of 5 kV/cm and larger input powers could be utilised for experiments with 4-ABN.

The AC-Stark curves can then be used to evaluate the performance of a mi-

crowave lens for 4-ABN. To calculate the force on the molecules in the microwave field ($h\nu = 16\,042$ MHz) a polynomial expression was fit to every M sublevel of the $8_{08} + (m + 1)h\nu$ rotational state. Along with an analytical expression for the microwave field and the properties of the resonator, this information was input into a trajectory simulation program that solves the equation of motion numerically (4th order Runge-Kutta procedure). Microwave focusing and decelerating experiments performed on ammonia [90–92] employed a Stark decelerator to prepare a packet of slow molecules before further manipulation with the microwave resonator (see Section 3.1). As discussed earlier in this section (Sec. 4.2) this is currently not a viable option for larger, more complex molecules, such as 4-ABN. Instead, we consider molecular packets originating from a supersonic expansion of a pulsed valve and from a buffer-gas cell.

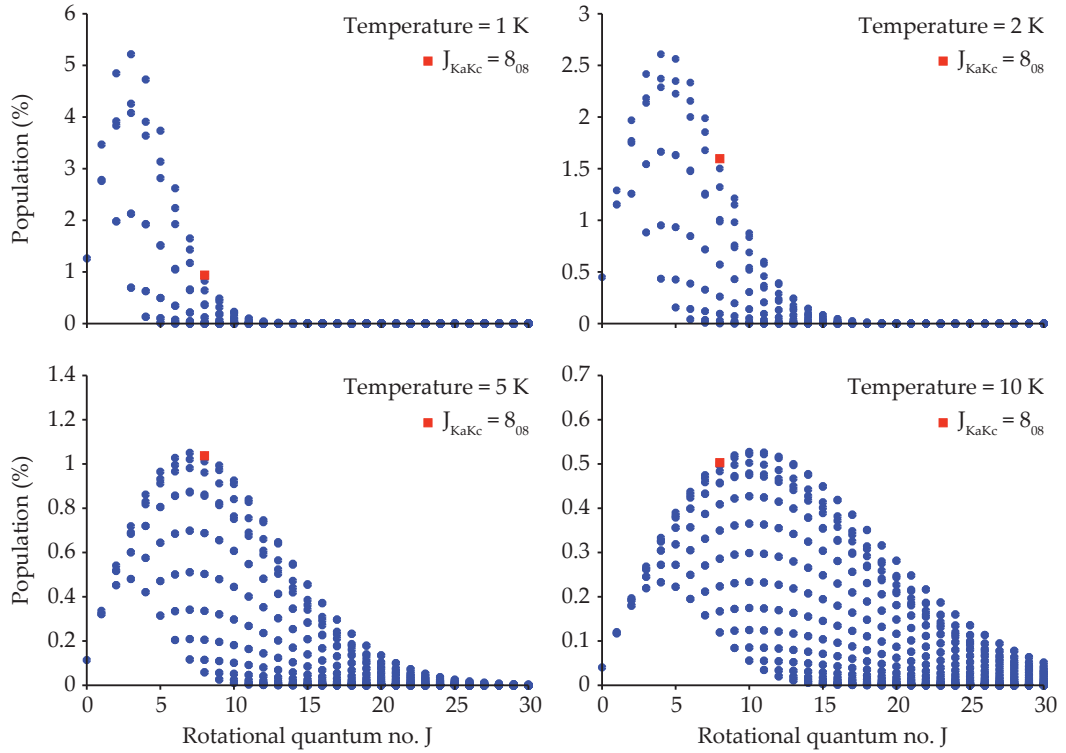


Figure 4.6: Population distribution of the rotational states up to $J = 30$ for 4-ABN at 1, 2, 5 and 10 K. The 8_{08} state of 4-ABN is marked in red. From 10 to 1 K, the scale of the y -axis changes by an order of magnitude. The percentage population of the 8_{08} state is approximately the same for all temperatures displayed.

A supersonic expansion of a dilute mixture of 4-ABN in xenon produces rotational temperatures of 5–10 K and longitudinal velocities of approximately 400 m/s. These longitudinal velocities are substantially higher than those utilized in the ammonia experiments. Effective deceleration and acceleration of a molecular beam of 4-ABN would require very long microwave resonators and high input powers. Therefore, the simulations here focus on microwave lensing (2D focusing) and microwave guiding (3D focusing), the latter of which can generate 3D control of a molecular packet resulting in spatial bunching. Simulations based on the experimentally determined rotational constants (Sec. 4.1.2) indicate that at a rotational temperature of 5 K the 8_{08} state of 4-ABN carries about 1% of the population. Similar values are also found for the rotational temperatures of 1, 2, and 10 K, refer to Figure 4.6. This observation was an additional reason for targeting the $8_{08} + (m + 1)h\nu$ manifold of 4-ABN in these experiments.

To focus the high-field-seeking 8_{08} state of 4-ABN with microwave fields a cylindrically symmetric resonator was designed with an entrance hole of 4 mm, an exit hole of 3 mm, an inner diameter of 13.23 mm and a length of 301 mm at room temperature. When cooled to 77 K, this microwave resonator supports the $TE_{1,1,18}$ mode at 16 042 MHz (see inset of Figure 4.7), which is 50 MHz red-detuned from the $9_{09} \leftarrow 8_{08}$ transition of 4-ABN. The precision of the resonator's inner diameter is of particular importance as a deviation of 10 μm would shift the cavity resonances by approximately 10 MHz. To reach a quality factor of $Q \approx 10\,000$, the resonator is made from oxygen-free copper and cooled to liquid nitrogen temperatures. The microwave input power P_{IN} is related to the circulating power in the cavity P_0 via $P_{\text{IN}} = P_0/(1 + \kappa)$, where κ is the coupling coefficient. With a simple dipole antenna, good impedance matching can be realised, and $\kappa \approx 1$ is a good estimation. Consequently, the circulating power is approximately half of the input power and an electric field strength of 4.5 kV/cm can be achieved with $P_{\text{IN}} = 100$ W.

Trajectory simulations were performed for a range of starting longitudinal velocities (50 to 400 m/s) and input powers (0 to 100 W) to establish the feasibility of microwave focusing and deceleration of 4-ABN. The longitudinal width of the generated packet is related to the opening time of the pulsed valve of approximately 150 μs , and the longitudinal velocity spread is approximated to be 12%. The transverse size of the molecular packet is given by the size of the skimmer orifice (100 μm

diameter), and the transverse velocity distribution is approximated as square distribution with a width of 8 m/s. In the simulations, the microwave radiation can be turned on and off depending upon the position of the so-called synchronous molecule. This is a hypothetical molecule that travels along the microwave resonator axis with the initial longitudinal velocity targeted for manipulation (refer to Section 3.1.1 for more detail). In the lens mode, MW radiation is turned on for the entire time that the synchronous molecule spends inside the resonator. Molecules are counted only if they arrive in a defined acceptance space behind the resonator that mimics the size and shape of a focused laser beam for REMPI detection (see Section 3.1.3). The simulation output is a time-of-flight profile that depends on the arrival time of the molecules.

The trajectory simulations show that the envisioned resonator design, in the

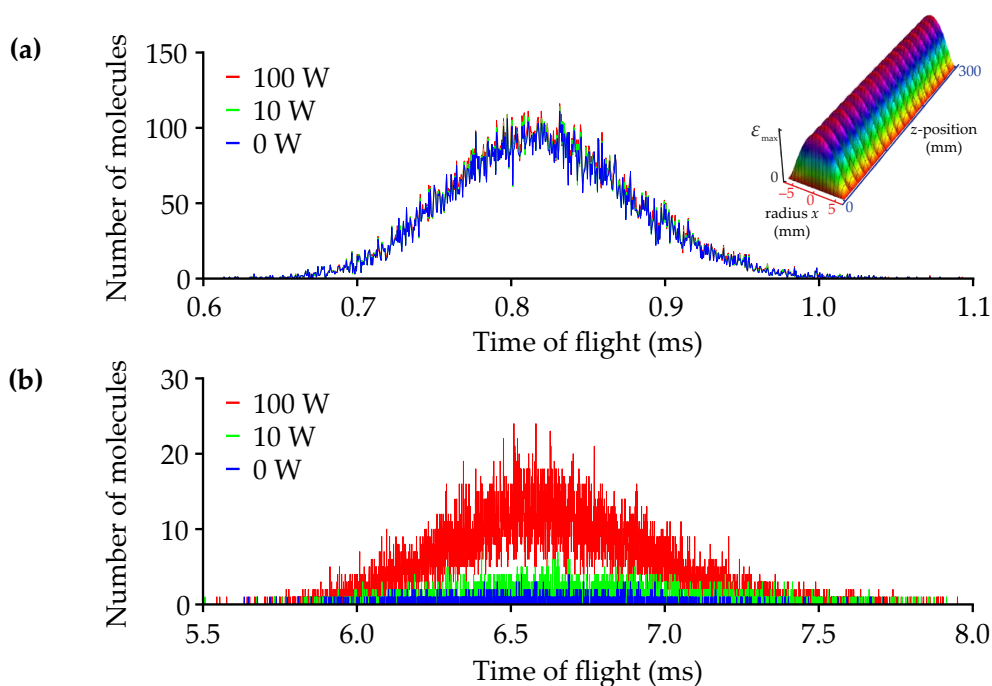


Figure 4.7: Time-of-flight profiles of 4-ABN from trajectory simulations in the lens mode with a $5\mu\text{s}$ resolution, employing the $\text{TE}_{1,1,18}$ mode of a cylindrically symmetric microwave resonator (upper right). The mean starting velocity is (a) 400 m/s with a total of 3×10^6 simulated molecular trajectories and (b) 50 m/s with a total of 6×10^6 simulated molecular trajectories.

lens mode, would have a negligible focusing effect on a molecular packet with a mean longitudinal velocity of $v_z = 400$ m/s. This is even the case for input powers as high as 100 W, see Figure 4.7(a). Such a molecular packet can be expected from a supersonic expansion of 4-ABN in xenon. According to the simulations, when comparing the number of molecules detected with input powers of 10 and 100 W to the simulation without a microwave field present (0 W), only minor increases of 2 and 4.5%, respectively, are observed. Molecules travelling at 400 m/s fly through the microwave resonator in approximately 0.75 ms. This rather short exposure time clearly limits the effect of the transversely focusing $TE_{1,1,18}$ mode

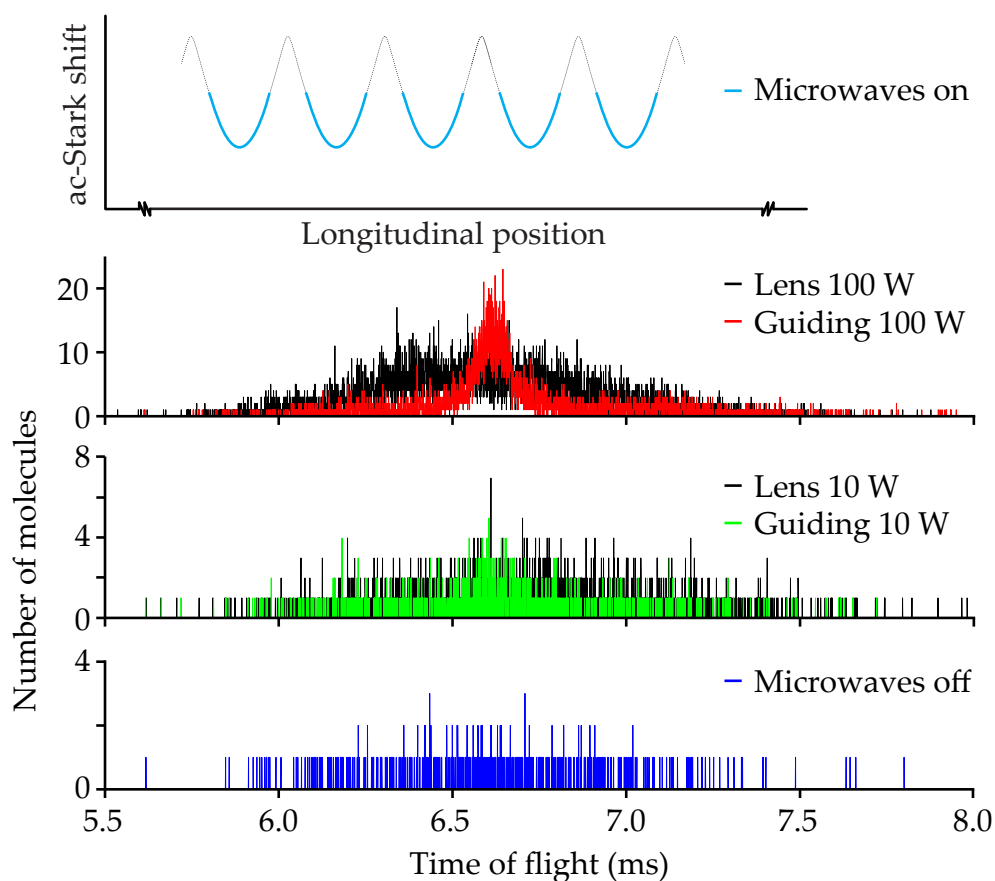


Figure 4.8: Comparison between the simulated time-of-flight profiles of 4-ABN for lensing and guiding by using a mean initial velocity of 50 m/s and a total of 6×10^6 simulated molecules. The top panel shows a schematic for the guiding switching scheme that was employed in the trajectory simulations.

on molecular motion.

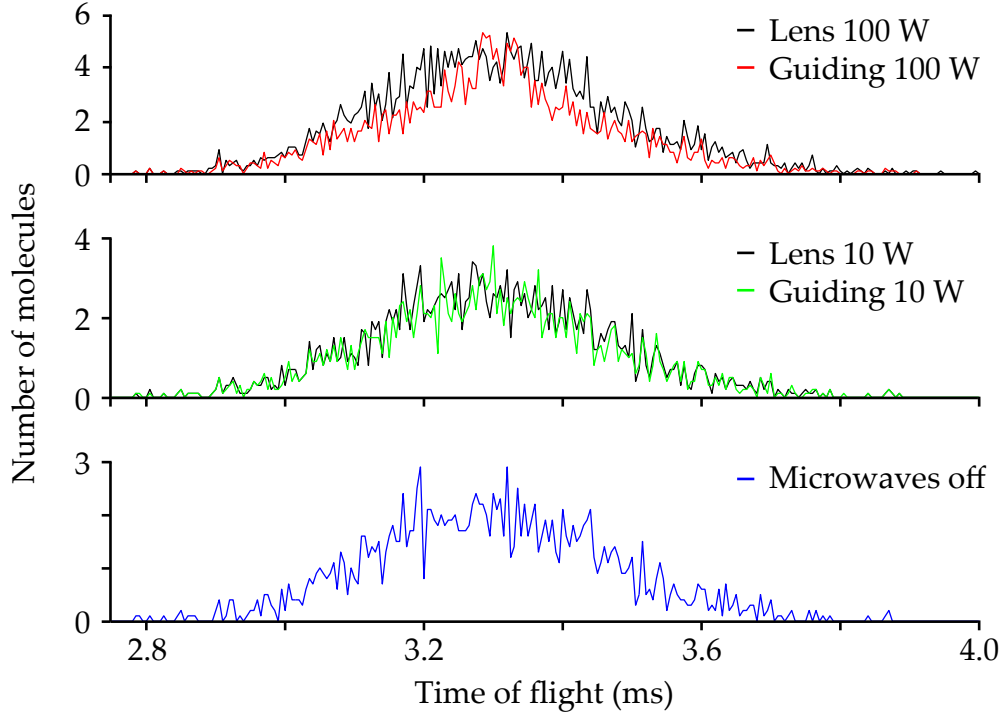


Figure 4.9: Comparison between the simulated time-of-flight profiles for lensing and guiding of 4-ABN with a mean initial velocity of 100 m/s and a total of 6×10^6 simulated molecules. Here, the number of molecules is the average number of detected molecules over $5 \mu\text{s}$ time steps to improve resolution.

For slower longitudinal velocities, losses from the molecular beam due to transverse motions increase, but the effect of the transverse focusing force from the microwave fields also becomes more apparent. At mean longitudinal velocities close to, or below, 100 m/s this behaviour is observable within the simulations. For $v_z = 50 \text{ m/s}$, molecules with initial transverse velocity components of $\pm 0.3 \text{ m/s}$ in the x -dimension and $\pm 0.2 \text{ m/s}$ in the y -dimension are detected at 0 W (Fig. 4.7(b)). Increasing the microwave power to 100 W increases the detectable initial transverse velocity components to $v_x = \pm 3 \text{ m/s}$ and $v_y = \pm 0.5 \text{ m/s}$. This corresponds to an increase in the time-of-flight signal by a factor of 20, as well as a 20-fold increase in the total number of detected molecules. When comparing the detectable transverse velocity components with each other it is important to consider the defined acceptance space. Here, the x -dimension lies along the path of the detection laser,

whereas the y -dimension falls along the height of the laser beam. Thus, as a rule the detectable v_x will always be larger than v_y .

In guiding simulations the microwave field is switched on and off when the synchronous molecule reaches a position within the resonator where the electric field strength is at 50% of its maximum (see the scheme in Figure 4.8). Due to the shape of the potential, the molecules that lag behind the synchronous molecule experience an acceleration towards it, those ahead experience a relative deceleration. At initial longitudinal velocities of 50 m/s with an input power of 100 W, this phenomenon can be clearly observed (Fig. 4.8). Comparing Figures 4.8 and 4.9, there appears to be no advantage gained by employing the guiding mode over the lens mode for input powers below 100 W or longitudinal velocities faster than $v_z = 50$ m/s. The signal gains brought about by longitudinal bunching are effectively cancelled out by the reduced transverse focusing inherent in the guiding switching scheme due to shorter durations for which the focusing microwave field is present. Results presented throughout this section indicate that the envisioned microwave resonator design would be far more effective when applied to a molecular beam with longitudinal velocities close to 50 m/s. Combining the proposed experimental set-up with a technique that could pre-decelerate a molecular packet of 4-ABN, such as buffer-gas cooling, would be a very interesting prospect.

4.2.3 Application of Stark decelerator

Considering the need for a pre-decelerated packet of 4-ABN molecules to observe focusing, guiding, and finally deceleration with microwave fields, simulations have also been carried out to determine the potential application of the Stark decelerator to such a system. As previously discussed (Sec. 4.2), Stark deceleration can generally not be applied to larger polyatomic systems as most states are high-field-seeking at electric field strengths close to 100 kV/cm. However, a recent study has identified potential rotational states of polyatomic asymmetric molecules that are low-field-seeking up to reasonable electric field strengths (~ 50 kV/cm) [150]. In the late 1990s, such states were focused in two dimensions for spectroscopic purposes using a quadrupole device [151, 152].

The highest energy rotational state of any J manifold of a near-prolate asym-

metric rotor, like 4-ABN, is the $J_{K_a K_c} = J_{J_0}$ rotational state. These states exhibit two qualities that make them interesting for Stark deceleration. A near degeneracy with the J_{J_1} rotational state results in an almost linear DC-Stark shift at low electric field strengths, and crossings that occur at larger electric field strengths represent mostly forbidden transitions. To determine this, the same numerical approach described earlier in Section 4.2.1 was utilized, but altered to calculate the DC-Stark (Sec. 3.1.1) shifts of 4-ABN. This meant disregarding the dressed-state formalism, which simplified matrix formation considerably. For the DC case the Hamiltonian can be written:

$$\mathcal{H} = \begin{pmatrix} E_0 & \Omega_{0,1} & \cdots & 0 \\ \Omega_{1,0} & E_1 & \Omega_{1,\dots} & \vdots \\ \vdots & \Omega_{\dots,1} & \ddots & \Omega_{\dots,N} \\ 0 & \cdots & \Omega_{N,\dots} & E_N \end{pmatrix} \quad (4.2)$$

Similar to Equation 4.1, the E_0 and E_N are the field free rotational states that form the diagonal, and $\Omega_{n,n'}$ ($n = 0, 1, \dots, N$) are the off-diagonal dipole moment matrix elements determined using the selection rules for the asymmetric top (Table 3.1). Rotational energy levels from $J = 0$ up to $J = 15$, including all K and M sublevels, were extracted from PGOPHER [119] to form the diagonal of Equation 4.2. After having input all the off-diagonal matrix elements, the matrix was diagonalized with increasing values of electric field strength to obtain the DC-Stark shifted energy levels. Conveniently, the second code used to determine if approaching rotational states cross or avoid (see Sec. 4.2.1) could be used with even fewer changes as only one selection rule ($\Delta m = \pm 1$, which refers to the dressed photons) needed to be removed. The M selection rule remained $\Delta M = 0$ as $M = \pm 1$ transitions are strictly forbidden in this case.

Previous simulations exploiting the AC-Stark effect focused on a rotational state where $J = 8$. Here, the rotational state of interest is the $J_{K_a K_c} = 4_{40}$. According to the calculations carried out in Reference [150], higher J states appear to result in larger trap depths. Although this would be preferential for decelerating/trapping experiments, higher J states are also less populated at temperatures

generated via a supersonic expansion (~ 1 K). Focusing on a rotational state with a lower J also provided the added benefit of simplifying calculations. Figure 4.10 shows the relevant DC-Stark shifts and crossings for the 4_{40} rotational state focusing specifically on the $M = 4$ sublevel. With increasing electric field strength avoided crossings of the $M = 4$ sublevel with other rotational states where $M \neq 4$ are strictly forbidden. This phenomenon is what enables the $4_{40}(M = 4)$ rotational state to remain low-field-seeking at larger electric field strengths. For electric field strengths larger than 20 kV/cm the outcome of crossing scenarios became increasingly difficult to interpret for the code, even when focusing solely on the $M = 4$ sublevel. Calculations were therefore restricted to a maximum electric field strength of 20 kV/cm, which is also reasonable from an experimental point of view. For the $J_{K_a K_c}, M = 4_{40}, 4$ rotational state of 4-ABN calculations predict a trap depth of approximately 0.62 K, which is essentially the same as the value

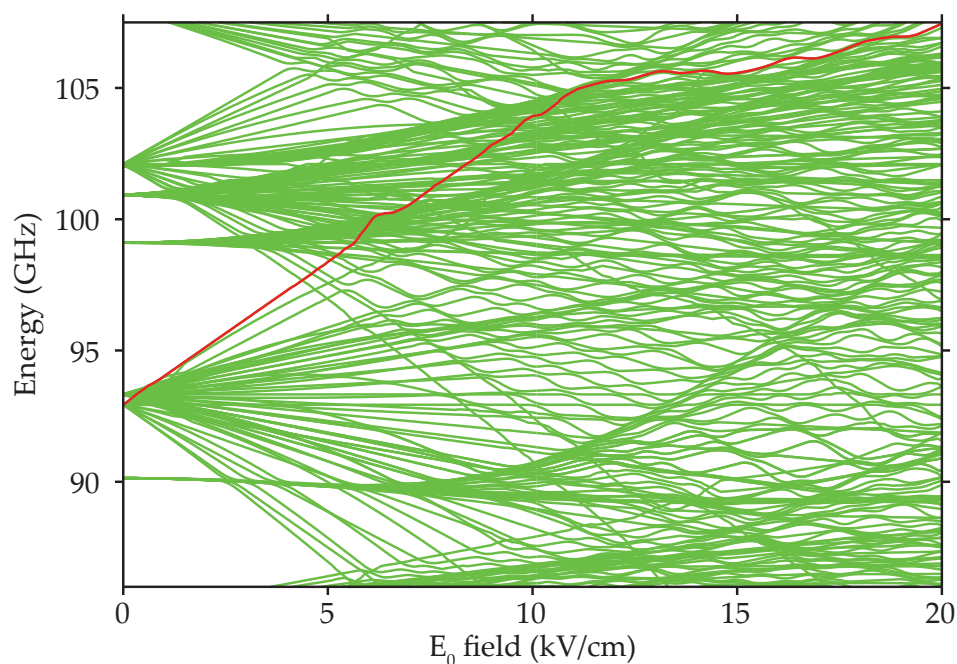


Figure 4.10: DC-Stark curves obtained from numerical calculations for 4-ABN. This includes all of the rotational states, including all the K and M sublevels, that are close in energy to the rotational state of interest, the $J_{K_a K_c}, M = 4_{40}, 4$ state in red.

determined in Reference [150].

Information determined from the DC-Stark calculations was input into a simulation that uses the already known time-dependent electric field distribution inside the Stark decelerator [70]. This simulation plots the trajectory of a molecular packet of 4-ABN, in the $4_{40}(M = 4)$ rotational state, through the decelerator. The mean longitudinal velocity of the molecules was chosen to be 400 m/s with a Gaussian longitudinal velocity spread and transverse velocity components ranging from 0 to 30 m/s. Starting with a total of 100 000 4-ABN molecules in the $4_{40}(M = 4)$ rotational state, simulations that employed the guiding mode of the

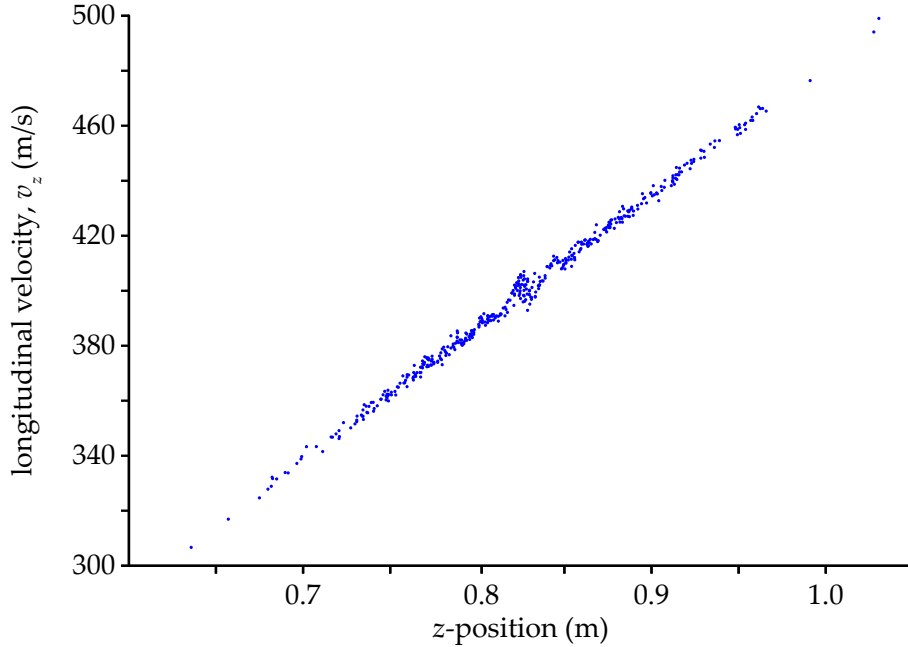


Figure 4.11: Simulated longitudinal phase space of 4-ABN in the $4_{40}(M = 4)$ rotational state. The simulation utilised the guiding mode of Stark decelerator with a maximum electric field strength of 20 kV/cm, and assumed an initial longitudinal velocity of 400 m/s with a longitudinal velocity spread of approximately 100 m/s. The snapshot of the longitudinal phase space is taken when the synchronous molecule is at the end of the Stark decelerator. Longitudinal bunching can be observed around the centre of the molecular packet as slightly faster/slower velocities are decelerated/accelerated closer to the position of the synchronous molecule.

Stark decelerator with the maximum electric field strength set to 20 kV/cm were carried out. The longitudinal phase space of the 4-ABN molecules at the end of the Stark decelerator is shown in Figure 4.11. In total, simulations anticipate that only 449 4-ABN molecules in the $4_{40}(M = 4)$ rotational state make it to the end of the decelerator. Although this is a rather low number, it is large enough to observe bunching in longitudinal phase space around the synchronous molecule. The observation of longitudinal bunching indicates that deceleration might also be effective.

4.3 Conclusions

The high-resolution broadband spectrum of 4-ABN was recorded and fit. The high sensitivity of the spectrometer meant that the ^{13}C and ^{15}N isotopologues could also be assigned. Consequently, the position of each heavy atom within the molecule was obtained using a mass-dependent least-squares fitting method. The experimentally determined rotational constants of 4-ABN produced an inertial defect of $-0.3 \mu\text{Å}$, which is typical for molecules that exhibit out-of-plane motions. An angle between the plane of the amino group and the plane of the benzene ring is responsible for the negative contribution to the inertial defect. B3LYP calculations that excluded and included Grimme’s empirical dispersion confirmed the presence of this inversion angle for the amino group of 4-ABN. Compared to previous investigation of 4-ABN’s structure, inversion angles predicted via theory [139] and determined experimentally in the crystalline phase [145] are considerably larger than the inversion angle predicted in this work, which would also results in a smaller μ_c dipole moment component. Here, it is rationalized that a smaller inversion angle and μ_c is more realistic as no c -type transitions were observed in 4-ABN’s rotational spectrum. This observation has a direct impact upon the microwave manipulation simulations. The dipole moment components are included in AC-Stark calculations and when non-zero also determine what selection rules are appropriate for the system.

To determine the AC-Stark shifts for different molecular systems of varying complexity a numerical approach has been developed. Trajectory simulations used this data to evaluate the feasibility of extending microwave focusing and

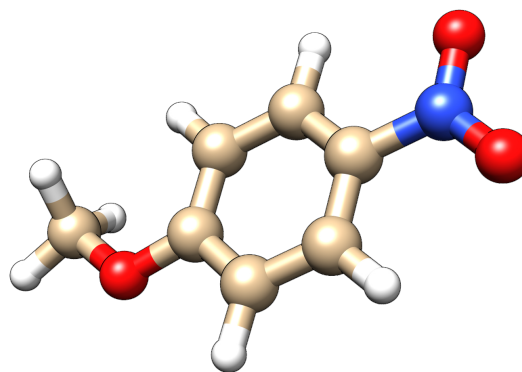
deceleration experiments from ammonia [90–92] to 4-ABN, a larger, more complex molecule. AC-Stark calculations performed for 4-ABN produced a trap depth of 3.1 GHz (~ 150 mK) at an electric field strength of 5 kV/cm. In simulations of the proposed experiment, the $TE_{1,1,18}$ resonance mode of a closed, high- Q microwave resonator manipulates a molecular packet of internally cold 4-ABN. To achieve input powers larger than 100 W is difficult and, due to the scaling of the electric field strength ($\mathcal{E} \propto \sqrt{P_{IN}}$), field strengths in excess of 10 kV/cm would be challenging to realise with closed, cylindrically symmetric microwave resonators. Thus, input powers have been limited to a maximum of 100 W.

Transverse (2D) focusing of high-field-seeking states could be achieved by using input powers as low as 10 W. However, longitudinal (3D) focusing was only observed with initial longitudinal velocities of 50 m/s and input powers of 100 W. To observe significant focusing and deceleration of the high-field-seeking states of 4-ABN, initial longitudinal velocities close to, or even below, 50 m/s would then be required. For the potential future application of accelerating or decelerating switching schemes it would therefore be necessary to work within such experimental parameters. This would rule out the possibility of starting directly from a supersonic expansion, for which mean longitudinal velocities as slow as 350 m/s could be achieved with xenon as a carrier gas. Alternatively, buffer-gas-cooling methods could be utilised to produce cold molecular beams with longitudinal velocities below 100 m/s and potentially replace a supersonic expansion source.

Essentially, microwave focusing and deceleration of larger molecules require a method that can create packets of molecules in high-field-seeking states with low mean longitudinal velocities (~ 50 m/s). This could be a counter-rotating pulsed valve [93] or the aforementioned buffer-gas cell. Microwave fields can be a powerful tool for spatial manipulation of complex polar molecules, which is ideally suited to complement current efforts for creating ultra-cold molecules, such as optoelectrical cooling [105]. Along with the AC trap, successful microwave deceleration and trapping make it possible to overlay polar ground-state molecules with an atomic magneto-optical trap. Such an experimental set-up could bridge the gap between cold and ultra-cold molecules via, for example, sympathetic cooling [104, 153].

The possibility of using the Stark decelerator with 4-ABN was also investigated. Although this technique would be restricted to specific rotational states

($J_{K_a K_c} = J_{J_0}$), initial simulations produce interesting results. Simulations predict the bunching of 4-ABN molecules in longitudinal phase space, which makes deceleration a viable option. Practical application of the Stark decelerator to a multi-level system such as 4-ABN would be challenging. Limiting the electric field strength to 20 kV/cm means a reduction in the number of molecules that actually arrive at the end of the decelerator. This means that if the rotational state of interest is not already well populated the observation of decelerated packets is unlikely. In this case, it would therefore be beneficial to selectively boost the population for a rotational state of interest. This prospect is investigated experimentally for 4-nitroanisole in Section 5.2.



Chapter 5

Nitroanisole*

4-nitroanisole is considered a push and pull π -conjugated system as it contains an electron-withdrawing and an electron-donating group at opposite ends of the molecule. The nitro group has a negative inductive and mesomeric effect on the phenyl ring and is thus the withdrawing group. The methoxy group has a negative inductive effect and positive mesomeric effect. Usually the mesomeric effect is stronger than the inductive effect, so overall the methoxy group is considered to be electron-donating. Surface-enhanced Raman spectroscopy (SERS) has been carried out on 4-nitroanisole and other similar "push-pull" systems [154, 155]. These studies use SERS to investigate the adsorption of such systems on silver nanoparticles and discuss their relevance for non-linear optical applications [156, 157]. With the adsorption of 4-nitroanisole to an Ag colloid, the electronic structure of the molecule can be altered via internal charge transfer between the methoxy and nitro group. After laser irradiation ($\lambda = 514.5$ nm) a catalytic reduction can occur resulting in further structural changes. Such changes can be better understood with a detailed knowledge of the system's structural properties.

In keeping with the other molecular systems under investigation within this thesis, 4-nitroanisole displays certain characteristics that make it an interesting candidate for motion manipulation experiments with AC-electric fields [158]. 4-nitroanisole has a large dipole moment to mass ratio (6.2D:153.04 u) and can be

*This chapter is based on the following publications: J. B. Graneek, C. Pérez, and M. Schnell, *Structural determination and population transfer of 4-nitroanisole by broadband microwave spectroscopy and tailored microwave pulses*, J. Chem. Phys. **147**, 154306 (2017).

easily seeded into a molecular beam. Effective deceleration and trapping of a molecule is dependent upon the interaction of an external field with a specific quantum state. This effectiveness is influenced by the size and complexity of the molecule under investigation. The ability to identify and selectively increase the population of a rotational state would be desirable for each of the focusing, deceleration, and trapping techniques that employ an external field discussed in Section 1.2.4. This would be especially useful for the application of the Stark decelerator to more complex molecules (refer to Section 4.2.3). So in addition to the structural determination of 4-nitroanisole, microwave double-resonance experiments have been designed to explore the possibility of increasing the population in a rotational state of interest.

5.1 Structure determination of 4-nitroanisole

The sensitivity and high resolution of Fourier transform microwave (FTMW) spectroscopy can provide detailed information on a molecule's structure (see Section 4.1). Prior to this study, 4-nitroanisole had not been investigated with such a technique and there was no experimental structure available for this molecule. Low resolution microwave spectroscopy has been used to study a number of molecules containing a methoxy group, including 4-nitroanisole [159]. Although this study was able to determine the rotational constants of 4-nitroanisole, it did not yield any structural parameters, such as bond lengths and angles, or information on the nuclear quadrupole coupling that arises due to the ^{14}N nucleus. The high resolution and sensitivity offered by chirped-pulse Fourier transform microwave (CP-FTMW) spectroscopy allows for the determination of such structural parameters [160, 161]. Other microwave spectroscopy studies carried out on nitrobenzene [162, 163] and anisole [164] were able to yield structural parameters that can be directly compared to those determined in this investigation. Such a comparison should provide more information regarding the influence of nitro and methoxy substituents on the phenyl ring.

5.1.1 Experimental details

The broadband rotational spectrum of 4-nitroanisole was recorded using the COMPACT spectrometer, for a detailed description of the set-up see Section 3.2. A sample of 4-nitroanisole was purchased from Sigma-Aldrich (97% purity) and used without further purification. The sample was placed within the reservoir of the nozzle and heated to approximately 90°C. Using neon as a carrier gas at a backing pressure of 2.5 bar, the mixture was supersonically expanded into the vacuum chamber at a repetition rate of 4 Hz. After supersonic expansion, the ensemble was excited by a 4 μ s long microwave chirp spanning 2–8 GHz. The microwave chirp was amplified by the TWT amplifier, which was set to various levels of gain. Reasons for using alternative gain settings of the TWT amplifier is discussed in Section 5.1.2. In addition to various levels of gain, measurements were also carried out where the TWT amplifier was replaced entirely by a solid-state amplifier with an output power of approximately 2 W. The molecular response of each measurement in the form of an FID was recorded for 40 μ s resulting in a spectral resolution of 25 kHz. In total, at 100% gain, 800 000 FIDs were co-added and Fourier transformed to produce a rotational spectrum with a signal to noise ratio of 1000:1. This is sufficient to observe the ^{13}C , ^{15}N and ^{18}O isotopologues of 4-nitroanisole in their natural abundance, which enables the determination of the molecular structure.

5.1.2 Results and discussion

Three different experimental broadband rotational spectra of 4-nitroanisole, measured with a solid-state amplifier, the TWT amplifier at 100% and 50% gain, as well as the corresponding fit are displayed in Figure 5.1. The measured intensities vary considerably depending on the gains employed. To rationalise this behaviour it is necessary to consider two different regimes of fast passage phenomena, the rapid adiabatic passage (RAP) and the linear fast passage (LFP). The large dipole moment of 4-nitroanisole means that for measurements taken at 100% gain (corresponding to an output power of at least 300 W) the RAP regime best describes transient effects during the chirp. In this regime, transfer and inversion of the population for a rotational transition can occur reducing coherence and therefore the intensity recorded. Even stepwise multi-resonance effects can occur when us-

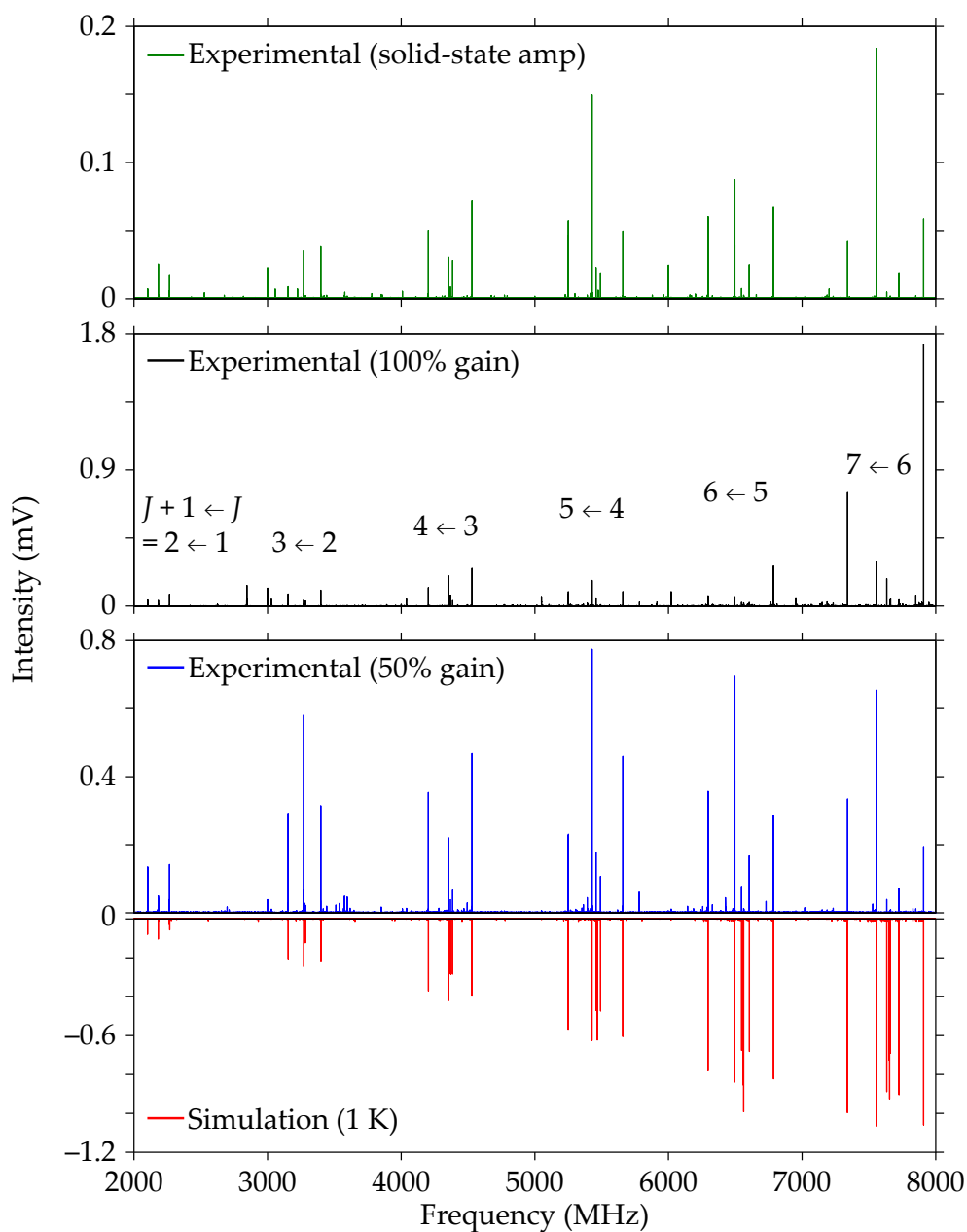


Figure 5.1: Rotational spectra of 4-nitroanisole; the upper traces show the experimental spectrum recorded at three different levels of amplification. According to specifications, using the TWT amplifier at 100% gain corresponds to a frequency dependent output power of at least 300 W, whereas a 50% gain gives an output power of approximately 75 W. The solid-state amplifier provides approximately 2 W output power. The lower trace represents a simulation using the fitted spectroscopic parameters reported in Table 5.1.

ing such a chirp. This phenomenon can affect the observed transition intensities further and can be used to explain the gradual increase in intensity from 2–8 GHz, i.e., for rotational transitions with higher J rotational quantum numbers, at 100% gain. This was previously observed for benzonitrile [165], which also has a large dipole moment ($\mu_a = 4.52\text{D}$). For the LFP regime, the chirp has a negligible effect on the population difference, instead coherence dominates resulting in increased transition intensities. Experiments carried out at 50% gain (corresponding to an output power of approximately 75 W) are within this LFP regime, hence the stronger intensities observed and better agreement with the predicted intensities from the PGOHPER program [119]. Line strengths predicted within PGOPHER rely on the Boltzmann distribution of a population at a selected rotational temperature, in this case 1 K, and ignore other effects that might alter a system's population distribution. From the intensities of the respective a -, b -, c -type transitions we can estimate a ratio of 6.75:1:0 for the dipole moment components, which is in good agreement with those predicted via calculations.

Structure optimization calculations were carried out in Gaussian09 [140] using different basis sets in combination with the B3LYP hybrid functional including and excluding Grimmes's empirical dispersion, as well as Møller-Plesset perturbation theory (MP2). The obtained rotational parameters, including the nuclear quadrupole coupling constants, from the B3LYP and MP2 calculations are listed in Table 5.1. While there is a good agreement between the experimental and calculated rotational constants, the nuclear quadrupole coupling constants largely deviate for the MP2 calculations. This is independent of the molecular structure used as a basis of the calculations so appears to be intrinsic to the method. Although not further discussed, the results of the MP2 calculation are included in Table 5.1 for completeness. After assignment of the strong a -type and weaker b -type transitions, the quantum-chemical rotational parameters could be directly compared to those determined experimentally. This assignment was performed with the program PGOPHER. The rotational quantum numbers involved in the assigned transitions range from $J = 1$ up to $J = 11$. In total 169 lines were assigned for the parent molecule with an average error of the fit of 4.9 kHz.

A closer look at the quadrupole coupling splitting due to the nitrogen atom of the nitro group can be found in Figure 5.2. The observed hyperfine structure is due

to the coupling of nitrogen’s nuclear charge density with the electric potential generated by the electrons and other nuclei. As 4-nitroanisole has only one strongly coupling nucleus, compared to 4-ABN less splitting is observed in the spectrum (Fig. 4.2) and the scheme used to interpret the coupling is also more straightforward (refer to Section 4.1). Nitrogen’s nuclear spin ($I(^{14}\text{N}) = 1$) couples with the molecular rotational angular momentum \mathbf{J} . Consequently the total angular momentum of 4-nitroanisole is \mathbf{F} rather than \mathbf{J} , and the new angular momentum quantum numbers are:

$$F = J + I, J + I - 1, J + I - 2, \dots, |J - I|$$

The experimentally determined nuclear quadrupole coupling constants for 4-nitroanisole are very similar to those determined for the ground state of nitrobenzene, where $\chi_{aa} = -1.1589(24)$ MHz and $\chi_{bb-cc} = -0.5199(68)$ MHz [166]. Nuclear quadrupole

Table 5.1: Spectroscopic constants of 4-nitroanisole determined experimentally and via quantum-chemical calculations. The value in square brackets was taken directly from calculations.

Parameter	Experiment	B3LYP/ aug-cc-pVTZ	B3LYP/(GD3BJ) aug-cc-pVTZ	B3LYP/(GD3BJ) def2-TZVP	MP2/ 6-311++G(d,p)
A (MHz)	3533.8097(5)	3565.90	3563.30	3565.43	3514.65
B (MHz)	587.03009(5)	586.25	588.15	588.07	584.66
C (MHz)	505.37812(5)	505.09	506.45	506.44	502.89
D_K (kHz)	0.33(8)
D_{JK} (kHz)	-0.031(5)
D_J (kHz)	0.006(1)
χ_{aa} (MHz)	-1.164(2)	-1.2409	-1.2494	-1.2813	-0.5915
χ_{bb-cc} (MHz)	-0.569(3)	-1.0179	-1.0172	-1.0495	1.3711
χ_{ab} (MHz)	[-0.1145]	-0.1145	-0.1168	-0.1200	-0.1336
$\mu_a/\mu_b/\mu_c$ (D)	...	6.15/0.78/0	6.14/0.78/0	6.09/0.78/0	5.45/0.0.82/0
N_{lines}	169
σ (kHz)	4.9

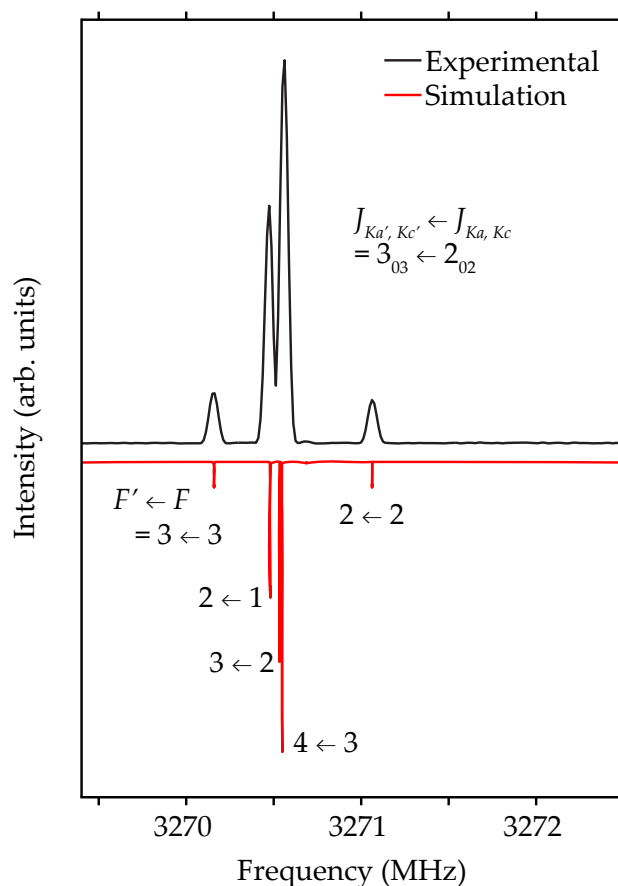


Figure 5.2: Nuclear quadrupole coupling splitting for the $J'_{K_{a'}, K_{c'}} \leftarrow J_{K_a, K_c} = 3_{03} \leftarrow 2_{02}$ rotational transition due to the ^{14}N atom in 4-nitroanisole measured at 50% gain. The F quantum numbers are also displayed.

coupling constants are sensitive to the local electronic environment, as well as the orientation of the principal axis system for the molecule. A difference in the nuclear quadrupole coupling constants of only 5 and 49 kHz for χ_{aa} and χ_{bb-cc} , respectively, would suggest that the addition of a para-methoxy group to nitrobenzene has only a small effect on the local electronic environments of the respective nitrogen atoms, or the orientation of the principal axis system, or both.

Initially, a larger difference between the nuclear quadrupole coupling constants was expected, as the additional methoxy group (a) introduces an electron donating effect and (b) re-positions the centre of mass and the inertial coordinate system of 4-nitroanisole relative to nitrobenzene. The closeness of the nuclear quadrupole coupling constants leads to two potential conclusions:

1. The electron donating effect of the para-methoxy group has little impact on

the electronic environment of the nitrogen atom due to the weak interaction via the phenyl ring, or the re-positioning of the coordinate system works to counteract this electron donating effect.

2. The nitrogen atom is a weakly coupling quadrupole nucleus and therefore not a sufficiently sensitive probe for such effects.

To gain more insight into the influence of nitroanisole's substituents on the phenyl ring more structural information is required.

The high sensitivity of the spectrometer allows for the observation of singly substituted ^{13}C , ^{15}N and ^{18}O isotopologues of 4-nitroanisole in their natural abundance. The lines assigned to the isotopologues for the $J'_{K_a',K_c'} \leftarrow J_{K_a,K_c} = 3_{12} \leftarrow 2_{12}$ transition are displayed in Fig. 5.3. Here, it is worth noting the absence of hyperfine structure observed for the ^{15}N isotopologue as $I(^{15}\text{N}) = 1/2$. The number of lines assigned and the rotational constants derived from the fits for each isotopologue are summarized in Table 5.2. As with 4-ABN (Section 4.1), this information is essentially for the determination of an experimental structure for 4-nitroanisole. The r_s coordinates for each heavy atom of 4-nitroanisole were determined using Kraitchman's equations [14] for both planar and non-planar molecules, implemented in the KRA program [149]. As expected, the non-planar approach is more appropriate as the inertial defect ($\Delta = I_c - I_a - I_b$) of 4-nitroanisole is $-3.91 \mu\text{\AA}^2$. Anisole displays a similar inertial defect of $-3.41 \mu\text{\AA}^2$ and was also treated with the non-planar approach [167]. For nitrobenzene an inertial defect of $+0.249 \mu\text{\AA}^2$ was determined [162]. The absence of the methoxy group and therefore the out-of-plane hydrogen atoms results in an inertial defect with a magnitude and sign expected of planar molecules with small amplitude vibrations.

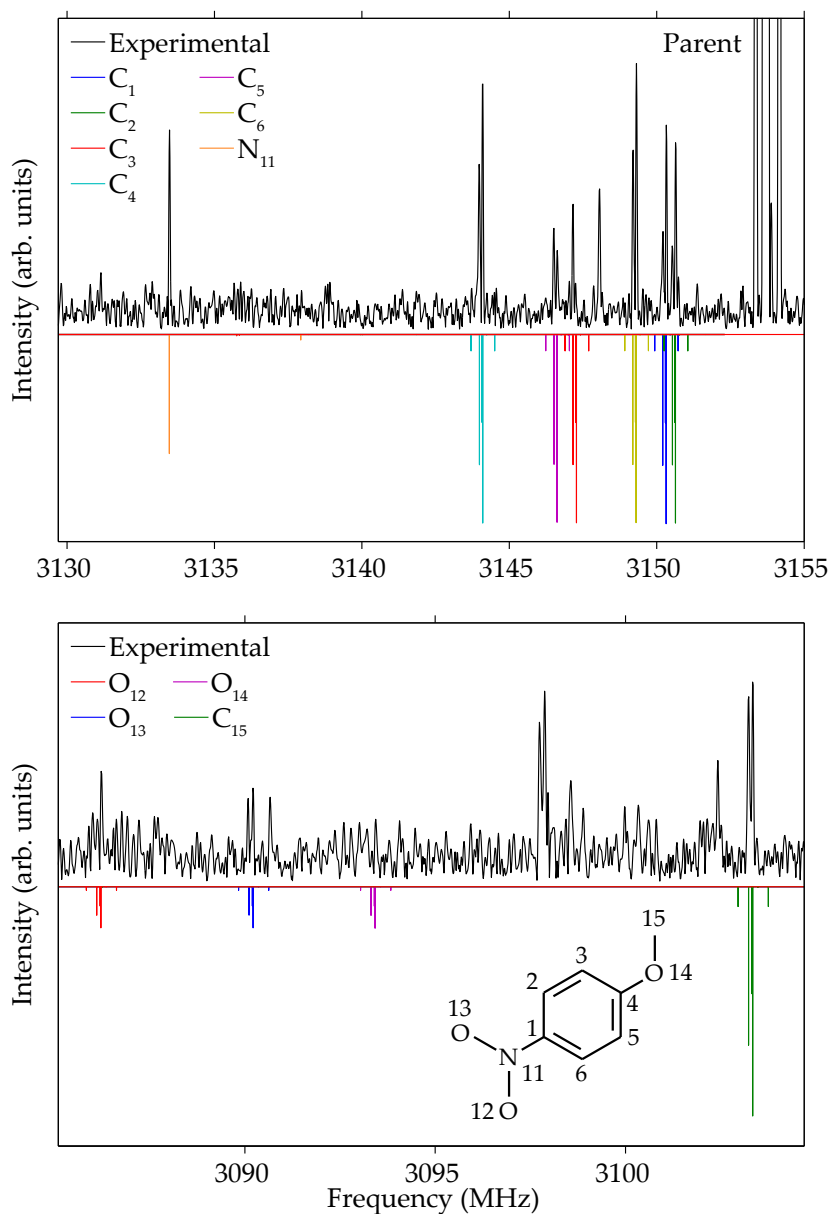


Figure 5.3: Satellite lines of singly substituted ^{13}C , ^{15}N , ^{18}O isotopologues and the parent lines for the $J'_{K_a',K_c'} \leftarrow J_{K_a,K_c} = 3_{12} \leftarrow 2_{12}$ rotational transition. The $^{18}\text{O}_{14}$ isotopologue is not assigned here as the corresponding transition intensity is too weak, but has been reliably assigned to transitions with stronger intensities. Also included is the molecular structure and atom labelling of 4-nitroanisole.

Table 5.2: Rotational constants determined from the assignment of each isotopologue. Also included are the number of lines assigned for each isotopologue (N_{lines}) and the average error of the fit (σ), which are needed for the subsequent Kraitchman calculations used to determine the substituted (r_s) molecular structure.

Parameter	Parent	C ₁	C ₂	C ₃	C ₄	C ₅
A (MHz)	3533.8097(5)	3533.39(9)	3502.06(9)	3507.38(9)	3532.35(7)	3486.44(9)
B (MHz)	587.03009(5)	586.3210(3)	586.9976(3)	586.1808(3)	585.0571(3)	586.4743(3)
C (MHz)	505.37812(5)	504.8519(3)	504.7036(3)	504.2258(2)	503.8874(3)	503.9885(2)
N_{lines}	169	45	46	41	45	39
σ (kHz)	4.9	3.7	4.0	4.2	5.0	3.2
Parameter	C ₆	C ₁₅	N ₁₁	O ₁₂	O ₁₃	O ₁₄
A (MHz)	3493.07(10)	3523.27(8)	3533.87(12)	3494.18(13)	3461.31(8)	3523.41(10)
B (MHz)	586.8905(3)	576.7990(2)	582.8467(3)	573.8157(4)	575.2556(4)	574.7626(4)
C (MHz)	504.4455(3)	497.5745(2)	502.2696(4)	494.7644(3)	495.1794(4)	496.0471(3)
N_{lines}	34	44	18	16	16	16
σ (kHz)	3.5	4.0	3.4	4.4	4.0	6.5

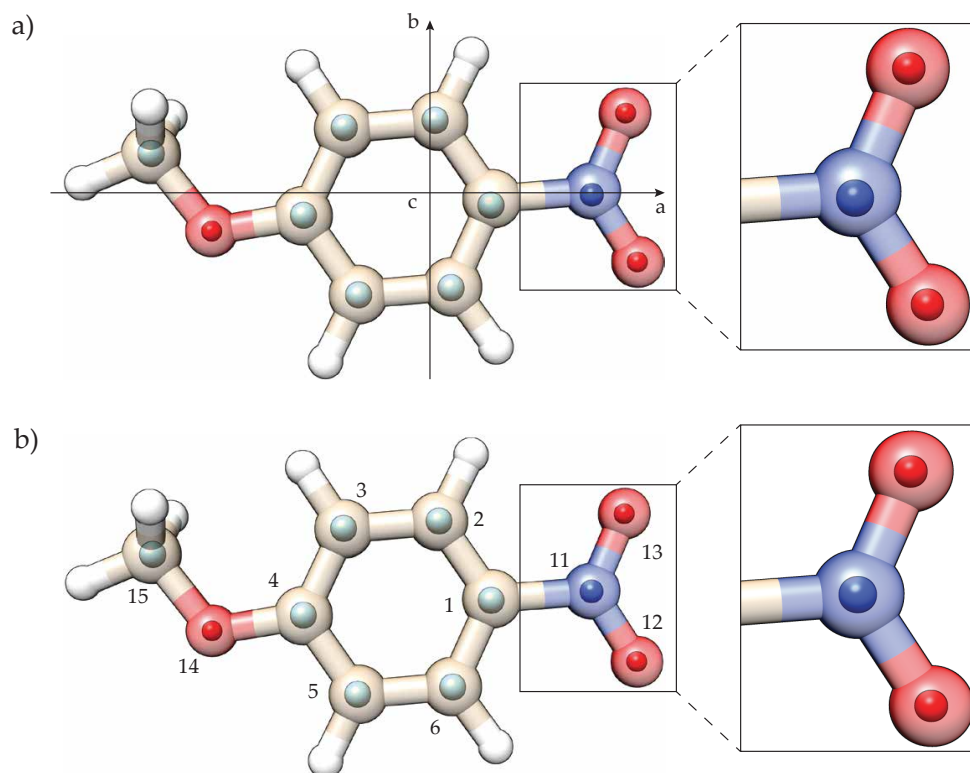


Figure 5.4: Comparison of the calculated (background) and the experimentally determined (foreground, spheres) atom positions, excluding hydrogen. Calculated atom positions obtained from B3LYP/aug-cc-pVTZ calculations. Experimental atom positions determined via (a) non-planar Kraitchman equations (r_s -structure), (b) mass-dependent least-squares fit ($r_m^{(1)}$ -structure). Also included is a reference to the inertial axis frame in (a) and the atom labels in (b).

Regardless of the approach employed, evaluation of the r_s structure for 4-nitroanisole was complicated by the closeness of several atoms to the inertial axes, refer to Figure 5.4(a). When adopting the non-planar approach, atoms N₁₁, O₁₂ and O₁₄ exhibit imaginary components along the c inertial axis. For the planar approach only the N₁₁ atom displayed an imaginary component, this time along the b inertial axis. As a result, the internal coordinates of these atoms could not be evaluated. This behaviour has also had an impact on the evaluated r_s structures of the phenyl ring, which is particularly evident for parameters that include atoms C₁, C₂ and C₆ (refer to Table 5.3). The planar approach does, however,

provide reliable structural information on the substituents of 4-nitroanisole. Although the N_{11} position could not be evaluated, the distance between the oxygen atoms of the nitro group could be determined. Similar issues arose when applying Kraitchman's equations to 4-ABN (Section 4.1), where even less r_s -coordinates could be obtained. Although similar in size and structural arrangement (compare Fig. 5.4(a) with Fig. 4.4(a)), the larger and heavier methoxy and nitro groups of 4-nitroanisole compared to the nitrile and amino groups of 4-ABN shift the principal axes so that more r_s -coordinates are attainable for 4-nitroanisole.

Table 5.3: Experimentally determined and calculated bond lengths of 4-nitroanisole; r_s -structure (Kraitchman's planar and non-planar equations), $r_m^{(1)}$ -structure (mass-dependent least-squares fit), r_e -structure (B3LYP/aug-cc-pVTZ).

Bond lengths	Planar, r_s (Å)	Non-planar, r_s (Å)	$r_m^{(1)}$ (Å)	B3LYP, r_e (Å)
C ₁ –C ₂	1.504(17)	1.474(17)	1.386(6)	1.386
C ₂ –C ₃	1.340(7)	1.326(9)	1.400(7)	1.387
C ₃ –C ₄	1.412(9)	1.406(7)	1.398(4)	1.398
C ₄ –C ₅	1.405(8)	1.408(6)	1.402(4)	1.402
C ₅ –C ₆	1.360(3)	1.353(9)	1.394(8)	1.378
C ₆ –C ₁	1.295(18)	1.344(18)	1.385(6)	1.393
C ₁ –N ₁₁	1.475(3)	1.463
N ₁₁ –O ₁₂	1.220(3)	1.225
N ₁₁ –O ₁₃	1.230(3)	1.225
O ₁₂ ···O ₁₃	2.171(3)	...	2.167(3)	2.166
C ₄ –O ₁₄	1.359(2)	...	1.356(2)	1.352
O ₁₄ –C ₁₅	1.424(5)	...	1.414(4)	1.430

Millen and Morton [168] encountered similar problems when determining the r_s structure of nitric acid. As the nitrogen atom lies so close to the molecule's centre of mass, Kraitchman calculations yielded a nitrogen position that altered

the resonance structure of the nitro group. The N–O bonds differed in length by almost 0.04 Å, and consequently the nitrogen position was readjusted to accommodate for the expected resonance structure. For comparisons to other molecules that contain a nitro group, Millen and Morton utilized the distance between the oxygen atoms, where their determined value was independent of any structural assumptions made. The O···O distance determined in this work from Kraitchman calculations is 2.171(3) Å. Although smaller than that determined for nitric acid, 2.190(3) Å [168], this matches the distance for nitrobenzene (2.171 Å) referred to by Cox and Waring in their study of the structure of nitromethane [169].

Table 5.4: Experimentally determined and calculated bond angles of 4-nitroanisole; r_s -structure (Kraitchman’s planar and non-planar equations), $r_m^{(1)}$ -structure (mass-dependent least-squares fit), r_e -structure (B3LYP/aug-cc-pVTZ).

Bond angles	Planar, r_s (°)	Non-planar, r_s (°)	$r_m^{(1)}$ (°)	B3LYP, r_e (°)
$\angle C_1C_2C_3$	117.95(48)	118.42(53)	118.94(31)	119.7
$\angle C_2C_3C_4$	118.98(24)	119.50(32)	119.29(25)	119.7
$\angle C_3C_4C_5$	120.49(13)	120.05(29)	120.57(22)	119.9
$\angle C_4C_5C_6$	120.51(27)	120.10(54)	120.16(23)	120.3
$\angle C_5C_6C_1$	120.44(44)	118.87(88)	118.30(36)	119.29
$\angle C_6C_1C_2$	121.62(29)	120.30(48)	122.74(42)	121.13
$\angle C_2C_1N_{11}$	118.25(38)	119.4
$\angle C_6C_1N_{11}$	119.01(40)	119.5
$\angle C_1N_{11}O_{12}$	117.78(25)	117.8
$\angle C_1N_{11}O_{13}$	117.90(24)	117.9
$\angle O_{12}N_{11}O_{13}$	124.31(10)	124.3
$\angle C_3C_4O_{14}$	124.08(57)	...	124.65(30)	124.7
$\angle C_4O_{14}C_{15}$	118.04(48)	...	118.07(30)	118.6
$\angle C_5C_4O_{14}$	115.43(63)	...	114.79(31)	115.4

For the methoxy group, r_s bond lengths determined via the planar approach can be directly compared to those obtained for anisole [167]. Once again, evaluation of the r_s structure was complicated by the positions of some atoms with respect to the inertial axes. To further investigate the structure of anisole, Desyatnyk *et al.* [167] performed a mass-dependent structural fit to yield the $r_m^{(1)}$ geometry, which is generally less susceptible to the effects that reduce the accuracy of the r_s -coordinates. The mass-dependent structural fit typically generates structures closer to the equilibrium structure as the method takes the inertial defect into account. This approach has been applied to a number of molecules, including the water heptamer [15] and cinnamaldehyde [160]. A least-squares fit of the structure to the rotational constants as well as an additional parameter was performed in the STRFIT program [149]. The extra parameter ($c_a = 0.0596(4) \mu^{1/2} \text{\AA}$) accounts

Table 5.5: Structural parameters determined via gas-phase electron diffraction (GED) [170] and microwave spectroscopy (r_s and $r_m^{(1)}$) for the substituents of both nitrobenzene [162, 171] and anisole [167], compared with those determined for 4-nitroanisole in this work.

Parameter ^a	Nitrobenzene		Anisole		4-Nitroanisole	
	GED	r_s	r_s	$r_m^{(1)}$	r_s	$r_m^{(1)}$
C–N	1.486(4)	1.4916(17)	1.475(3)
N–O	1.223(3)	1.2273(2)	1.225(3) ^b
O...O	...	2.171 ^c	2.171(3)	2.167(3)
∠ONO	125.3(2)	124.35(1)	124.31(10)
C–O	1.381(4)	1.372(3)	1.359(2)	1.356(2)
O–C	1.418(3)	1.417(2)	1.424(5)	1.414(4)
∠CCO	114.0(5)	114.8(3)	124.08(57)	124.65(30)
∠COC	117.2(4)	117.5(3)	118.04(48)	118.07(30)

^a Bond lengths in Å and angles in degrees.

^b Average of the two N–O bond lengths obtained.

^c Value referred to by Cox and Waring [169].

for the isotope-dependent rovibrational contribution to the moments of inertia of the molecule [138]. A direct comparison of the structural parameters obtained from each approach is given in Tables 5.3 and 5.4. The quantum-chemical theoretical predictions, which correspond to a hypothetical equilibrium structure (r_e) at a potential energy minimum without zero-point vibration, are in much better agreement with the $r_m^{(1)}$ structure than the r_s structure. This is also visible from Figure 5.4(b).

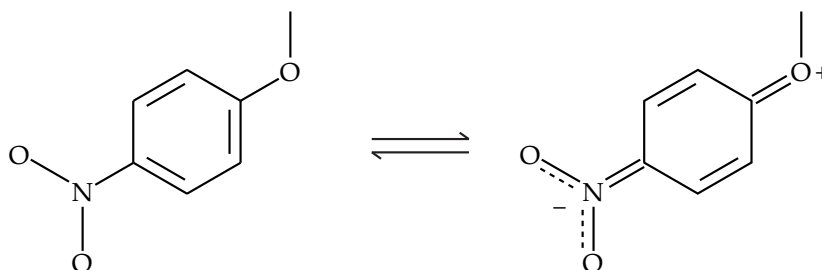


Figure 5.5: Resonant forms of 4-nitroanisole. Left is the benzoid form, right the quinoid zwitterion form.

The methoxy group of 4-nitroanisole behaves as an electron-donating group, contributing electron density to the phenyl ring. Coupled with the electron-withdrawing effect of the nitro group, a reduction in the C₄–O₁₄ bond length compared to the r_s and $r_m^{(1)}$ structures of anisole was observed, refer to Table 5.1.2. The reduction in the C–O bond length also causes the $\angle\text{CCO}$ angle to increase due to steric effects. For the reasons described earlier, the evaluation of the r_s structures for 4-nitroanisole complicates comparisons to the nitro group of nitrobenzene. The $r_s(\text{O}\cdots\text{O})$ distance of 4-nitroanisole and nitrobenzene is essentially the same, but the lack of any other r_s parameters for the nitro group of 4-nitroanisole forces us to rely more on the determined $r_m^{(1)}$ parameters. There is little variation in the N–O bond length obtained irrespective of the method used to evaluate this distance; however, there is a rather large alteration in the bond that connects the nitro group to the phenyl ring.

Here, the $r_m^{(1)}(\text{C–N})$ bond length of 4-nitroanisole is more than 0.01 Å shorter than the distances reported in gas-phase electron diffraction (GED) [170] and microwave [162, 171] studies of nitrobenzene. As the nitro group withdraws electron

density from the phenyl ring this encourages the donation of more electron density from the methoxy group. Electronic charge transfer from the methoxy to the nitro group through the π -conjugated system has been confirmed by UV absorption of 4-nitroanisole in different solvents [155]. A result of this charge transfer process is that two resonant forms of 4-nitroanisole can exist in solution; a benzenoid form and a quinoid form (Fig. 5.5). There is no noticeable effect on the $r_m^{(1)}$ bond lengths of the phenyl ring, which within the errors are very similar. The reduction of the C–O and C–N bond lengths of 4-nitroanisole compared to the same bond found in nitrobenzene and anisole, respectively, supports the migration of electron density across the phenyl ring, which is consistent with the "push-pull" picture of 4-nitroanisole.

5.2 Population transfer experiments

In addition to structural determination of 4-nitroanisole and understanding the effects of the substituents on the phenyl ring, the potential of transferring population between selected rotational states with tailored microwave pulses was investigated. For somewhat larger/heavier molecules like 4-nitroanisole the population distribution, even at temperatures between 1–3 K, covers many rotational states due to small rotational constants on the order of a few GHz and less. Here, we employ tailored microwave pulses in a double-resonance scheme to drive and then observe the transfer of population from a well populated rotational state. Double-resonance experiments are more typically used to facilitate the analysis of complex rotational spectra by identifying the connectivity of energy levels [172–177]. The aim of this study is to significantly increase the population of a particular energy level that can then be exploited in experiments, such as Stark deceleration (see Section 4.2.3).

Once the spectrum of 4-nitroanisole was assigned, three-level systems were identified so double-resonance experiments could be applied. The emission signal recorded in CP-FTMW spectroscopy is proportional to the population difference of the two energy levels involved in the transition. So the strength of the emission signal detected after the application of tailored microwave pulses indicates to what extent population is transferred between rotational states, and also reconfirms the

connectivity of the transitions under investigation.

5.2.1 Experimental details

Detailed analysis of 4-nitroanisole's rotational spectrum allowed for the identification of a candidate transition. Here the $J'_{K_a',K_c'} \leftarrow J_{K_a,K_c} = 2_{02} \leftarrow 1_{01}$ transition at 2183.17 MHz was chosen, and will henceforth be referred to as the pump transition. This transition is ideal as both the upper and lower states are involved in a number of transitions that occur within the 2–8 GHz frequency range covered by the COMPACT spectrometer. Transitions that share an upper or lower state with the pump transition are referred to as 'signal' transitions. These signal transitions can be probed with a $\pi/2$ -pulse to establish how population is redistributed after the pump transition is exposed to a tailored microwave pulse. When exciting rotational transitions with a single frequency pulse alone the effect of pulse duration on signal strength is well understood [178, 179]. A π -pulse results in a population inversion for the transition and a significant reduction of the emission signal,

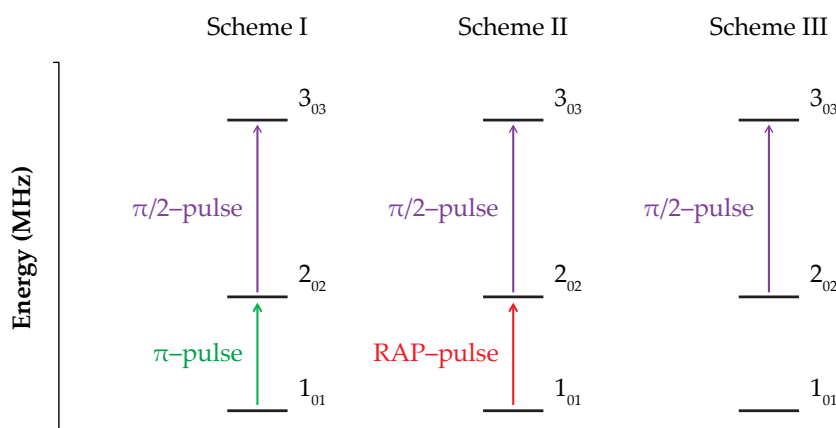


Figure 5.6: Different pulse schemes employed for the population transfer experiments. The single frequency 2-pulse scheme (scheme I), the RAP 2-pulse scheme (scheme II), and the single frequency single pulse scheme (scheme III). Changes in the population distribution, brought about by a π -pulse or RAP-pulse, affects the signal intensity for the $J'_{K_a',K_c'} \leftarrow J_{K_a,K_c} = 3_{03} \leftarrow 2_{02}$ transition recorded after the $\pi/2$ -pulse. Comparing the signal measured for schemes I and II with scheme III should indicate to what extent population is redistributed.

whereas a $\pi/2$ -pulse results in maximum coherence and thus a maximum emission signal. The emission signal is directly proportional to the population difference between the rotational states involved in a transition. This is also the case for excitation via a chirp pulse [13].

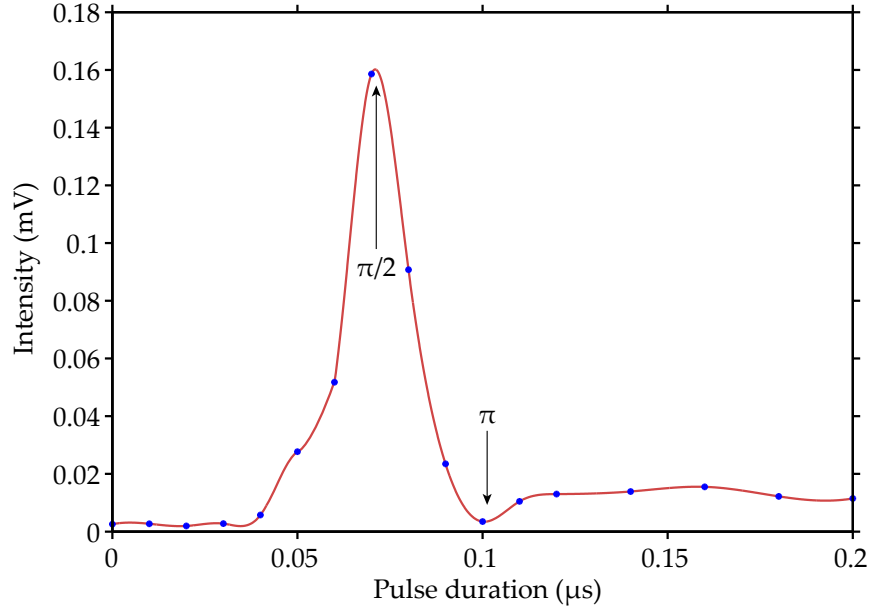


Figure 5.7: Nutation curve of the $2_{02} \leftarrow 1_{01}$ at 2183.17MHz with a step-width of 10 ns until a pulse duration of 120 ns, then a 20 ns step-width thereafter. All pulses were amplified with the TWT amplifier at 100% gain. Both the π -pulse and $\pi/2$ -pulse durations are also indicated in the plot.

The pump transition is a strong *a*-type transition observed at 2183.17 MHz. There are four signal transitions within the 2–8 GHz frequency range that were accessible and of a decent intensity: $2_{11} \leftarrow 2_{02}$, $3_{03} \leftarrow 2_{02}$, $2_{12} \leftarrow 1_{01}$ and $3_{13} \leftarrow 2_{02}$ at 3028.32, 3111.70, 3270.55, 5049.95 and 6020.53 MHz, respectively. Nutation measurements were recorded for each of the signal transitions. These measurements record the signal intensity for a transition of interest gradually increasing the pulse duration in order to determine the respective π -pulse and $\pi/2$ -pulse durations (refer to Figure 5.7). Originally all of the nutation measurements were carried out using the TWT amplifier. However, due to sideband formation [165, 180] it became necessary to work with the 2W solid-state amplifier, where such

effects are much less pronounced.

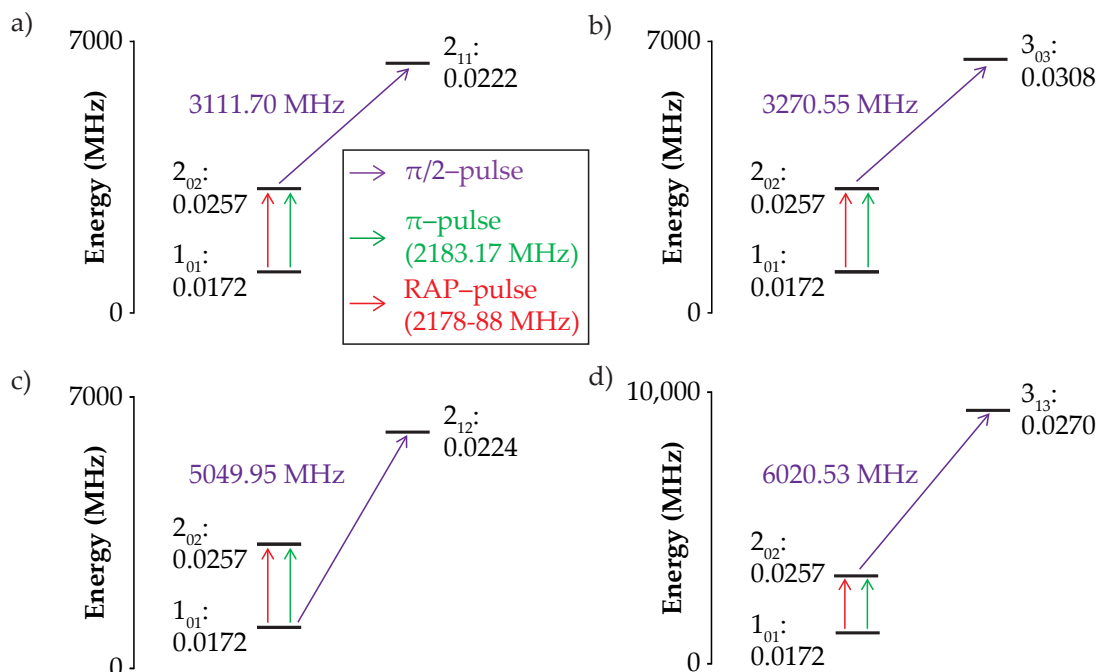


Figure 5.8: Schematic of each transition connected to the $J'_{Ka',Kc} \leftarrow J_{Ka,Kc} = 2_{02} \leftarrow 1_{01}$ transition. Approximate population numbers at 1 K follow the rotational state labels and were determined in PGOPHER. A total population of one was distributed over all the rotational levels up to $J = 30$. These numbers are included to better illustrate how a 2-pulse scheme would affect the population of rotational states involved in a signal transition. Both progressive (a, b, and d) and regressive (V-type; c) arrangements are probed.

Different pulse schemes were designed to utilise the optimized pulses (Fig. 5.6) for the observation of population transfer. Scheme I pumps the $2_{02} \leftarrow 1_{01}$ transition at 2183.17 MHz with a π -pulse that should invert the population of the two states, then probes this population inversion via a signal transition with a $\pi/2$ -pulse. Scheme II pumps the $2_{02} \leftarrow 1_{01}$ transition with a 10 MHz broad chirp centred around the resonance frequency with a fixed pulse duration of 250 ns. The experimental set-up of scheme II differed slightly from the set-up employed for the other schemes as it required the use of both the TWT and solid-state amplifiers. Here, the TWT amplified the 10 MHz chirp at 100% gain to ensure that the pulse was within the rapid adiabatic passage (RAP) regime, whilst the subsequent $\pi/2$ -

pulse was amplified by the solid state amplifier. The so-called RAP-pulses are considered a more robust method for population inversion and have been utilized to enhance the transfer of population [181, 182]. Scheme III consists of only one $\pi/2$ -pulse that probes a signal transition and was applied directly after each of the 2-pulse experiments to act as a reference.

5.2.2 Results and discussion

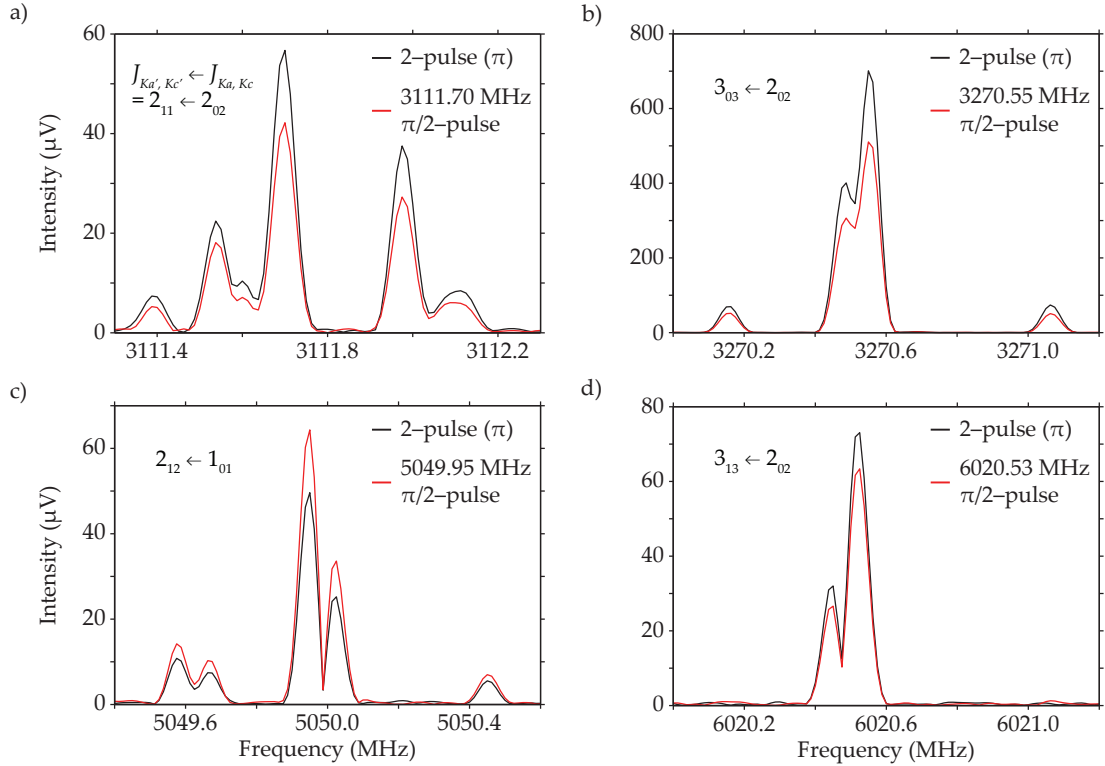


Figure 5.9: Measured intensities for each of the signal transitions using single frequency microwave pulses. The black trace is the result of scheme I and the red trace the result of scheme III.

Figure 5.8 shows each of the signal transitions probed with the different schemes described in Section 5.2.1, as well as the approximate occupation for each of the states. The signal detected after excitation of a rotational transition using a single frequency microwave pulse is directly proportional to the dipole moment, the electric field strength, and the population difference between the states involved

in the transition [13, 178, 183]. Changes in the population of rotational states involved in a signal transition, caused by the population inversion of the pump transition ($2_{02} \leftarrow 1_{01}$), alters the emission signal detected. Comparing the intensities measured at a signal transition frequency for the different schemes should indicate the extent to which population is being transferred between the pump transition's rotational states.

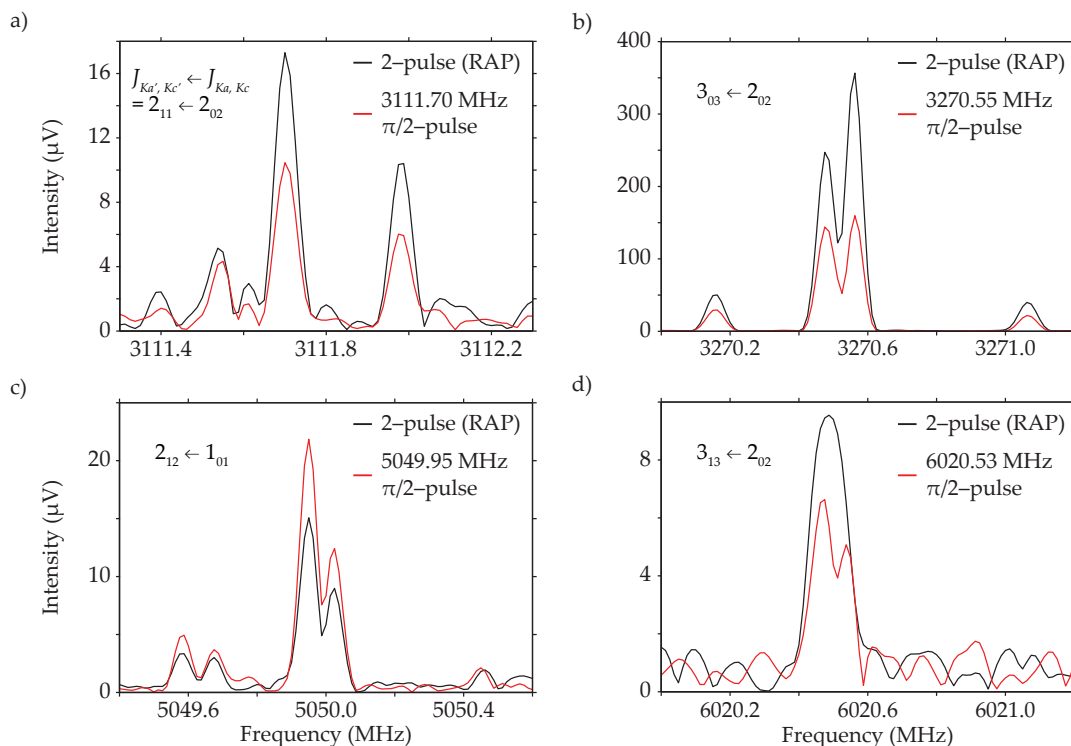


Figure 5.10: Measured intensities for each of the signal transitions using a combination of single frequency pulses and 10 MHz broad chirps. The black trace is the result of scheme II and the red trace the result of scheme III.

PGOPHER was used to calculate the population distribution of 4-nitroanisole at 1 K. This is the approximate rotational temperature of a supersonically expanded sample of 4-nitroanisole seeded with neon within the experimental set-up. The signal detected when scheme III is employed depends upon the population difference of the signal transition. Should conditions allow for population inversion, the numbers calculated with PGOPHER can be used to determine the direction of intensity change measured for each of the signal transitions. According to the

calculated population differences, when comparing the results of scheme III with I a reduction in intensity for signal transitions at 3111.70, 3270.55 and 6020.53 MHz and an increase in intensity for the signal transition at 5049.95 MHz should be observed. This is corroborated by the measurements taken, refer to Figure 5.9. Even if the π -pulse were to invert only 85% of the population for the states involved in the pump transition the same trend would be expected. The change in intensity recorded when moving from scheme II to III also follows this trend (Fig. 5.10), but results in larger intensity differences. For example, for the $3_{03} \leftarrow 2_{02}$ transition at 3270.55 MHz, scheme I results in an increase in signal of approximately 37% when compared with the measured signal from scheme III, whereas scheme II recorded a 123% increase in signal from scheme III. Figure 5.11 plots the percentage differences in intensity for each signal transition. The observed differences suggest that the RAP-pulse has enhanced the population inversion of the pump transition.

A notable difference between scheme I and scheme II is in the treatment of the M substates (M being the quantum number that describes the projection of angular momentum \mathbf{J} onto an external field axis). Strictly speaking, we only observe the average π - and $\pi/2$ -pulse durations for the manifold of M substates, which results in the broadening of the nutation curves (Fig. 5.7). The different transition dipole moments for the M components lead to different optimum durations for the excitation pulse. A π -pulse cannot address all M substates involved in a rotational transition, which is different for the RAP pulse. For the RAP-pulse all the M substates of the lower rotational state with counterparts in the upper rotational state that obey selection rules will be affected. The electric field vectors of scheme I and II differ because of experimental limitations. In scheme I the electric field vectors of the two pulses are parallel, thus transitions must obey the selection rule $\Delta M = 0$. In scheme II, both the TWT and solid-state amplifiers are used with two inputs of a dual polarization horn antenna, so the $\Delta M = \pm 1$ selection rule applies. These differences in the treatment of the M states contribute to the observed intensity differences between schemes I and II. The effect that these tailored microwave pulses have on rotational state population can be clearly observed and predicted, demonstrating their potential for selectively populating rotational states of interest.

5.3 Conclusions

The high-resolution broadband rotational spectrum of 4-nitroanisole, which is considered a typical "push-pull" molecule, was recorded. The high sensitivity of the spectrometer allowed for the assignment of all the ^{13}C , ^{15}N , ^{18}O isotopologues of 4-nitroanisole. Consequently, the position of every heavy atom within the molecule could be obtained via Kraitchman calculations. The accuracy of the rotational constants also allowed for a mass-dependent least-squares fitting method to be applied for structural determination. Results from the least-squares fitting approach provided more reliable structure with reduced errors when compared to the r_s -structure obtained from Kraitchman calculations. This structure was directly compared to nitrobenzene and anisole, where the reduction in the respective

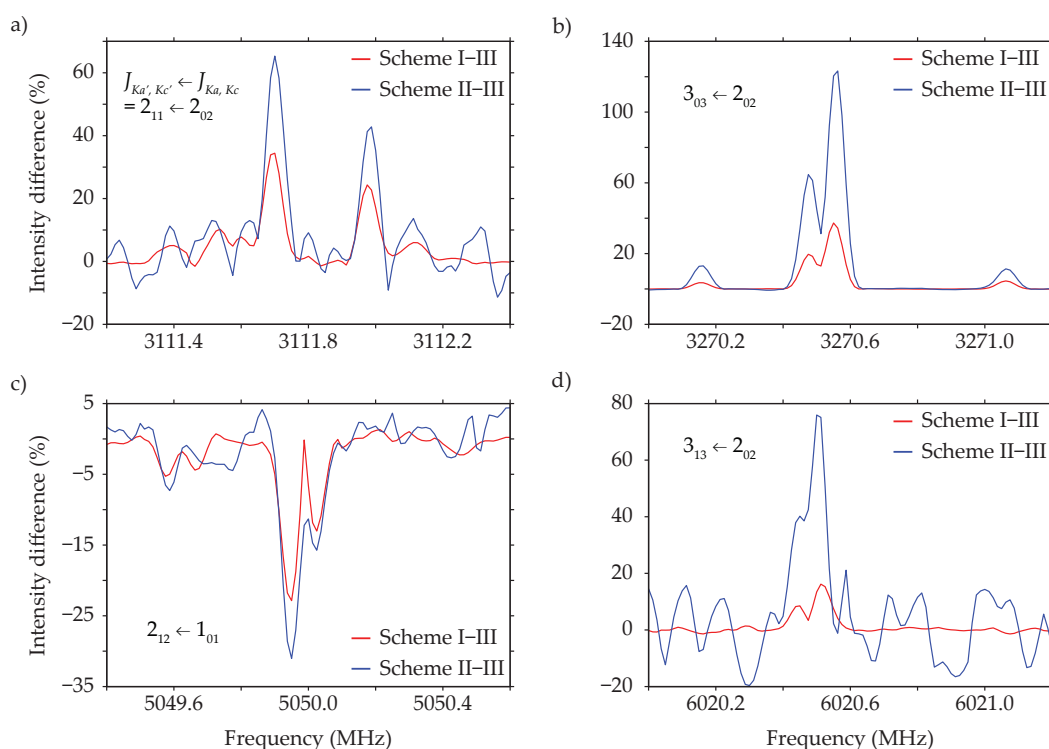
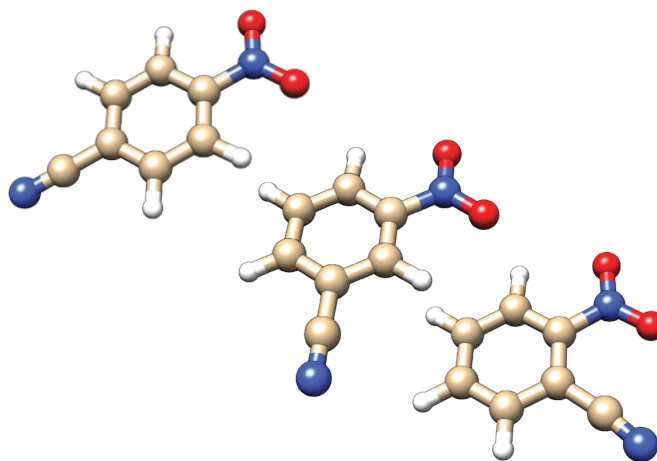


Figure 5.11: Percentage difference for each signal transition of the two different pulse schemes. Percentages determined by calculating intensity difference relative to the maximum intensity recorded using Scheme III alone.

C–N and C–O bond lengths was rationalised by the "push-pull" effect present in 4-nitroanisole.

Population transfer experiments were carried out using tailored microwave pulses. PGOPHER was used to predict the population distribution of 4-nitroanisole at 1 K. These numbers were then used to understand the changes in intensity of select rotational transitions brought about by the redistribution of population via the different pulse schemes. The population of the states involved in the pump transition were altered via a π -, or a RAP-pulse. Consequently, new population differences for the signal transitions were determined and the effect on the transition intensities predicted. The differences in the intensity recorded with the different pulse schemes confirmed the anticipated redistribution of population. This demonstrates that tailored microwave pulses can be used to populate specific rotational states of interest.

Increasing the population occupation for a state of interest would be advantageous for the motion manipulation techniques mentioned in the introduction (Sec. 1.2) and Section 4.2.3. This is especially the case for experiments that aim to guide and decelerate larger, more complex molecules with static electric fields [150] or with microwave fields [158]. For such examples, a larger density of rotational states, due to the relatively small rotational constants, reduces the effectiveness of the manipulation method applied. With increasing electric field strength the chance for the rotational state of interest to cross and/or avoid other rotational energy levels increases, increasing the potential for losses from a molecular packet. The use of microwave pulses to transfer more population to a state of interest would be a viable way to compensate for such losses.



Chapter 6

Nitrobenzonitrile

Nitrobenzonitrile (NBN) consists of two electron-withdrawing groups, both of which have negative inductive and mesomeric effects on the phenyl ring. This leads to an electron poor aromatic ring relative to benzene, which can also be described as deactivated. The position of the nitro with respect to the nitrile group produces three different molecular dipole moments varying in magnitude. The *para* position, corresponding to 4-NBN, produces the weakest molecular dipole moment as it has two electron-withdrawing groups pulling from opposite ends of the phenyl ring. Moving to the *meta* (3-NBN) and *ortho* (2-NBN) positions partly redistributes the electron density of the phenyl ring to one side, resulting in a more polar molecule. As benzonitrile and some of their derivatives display interesting biochemical and physical properties [184–186], all three NBN molecules have been previously investigated via Hartree-Fock and density functional theory methods [187]. Besides the intriguing chemistry that arises from the strongly electron-withdrawing groups present in NBN, part of our motivation stems from the potential application of deceleration and trapping techniques. The large dipole moment to mass ratios for 2-NBN (6.97 D:148.12 u), and 3-NBN (4.38 D:148.12 u), together with the ease at which they can be seeded into a molecular beam, make these molecules ideal candidates for experiments that aim to control and manipulate a molecule's motion using external electric [52], magnetic [53] or electromagnetic fields [88–90].

Owing to their polarity, these molecules can be studied using high resolution chirp-pulse Fourier transform microwave (CP-FTMW) spectroscopy. The high

sensitivity and resolution offered by this technique allows for the determination of structural parameters [160, 188, 189], as well as information on the nuclear quadrupole coupling that arises due to the presence of ^{14}N nuclei in NBN. These, in turn, can provide valuable information on the electronic environment and thus the effect on bonding with the respective nucleus. As of yet, microwave spectroscopy has not been applied to either 2- or 3-NBN. The almost negligible dipole moment of 4-NBN (0.09 D) makes the acquisition of its pure rotational spectrum difficult. Consequently, structures of 4-NBN determined via quantum-chemical calculations and X-ray crystallography [190] are utilised to compare with the structural parameters of 2- and 3-NBN determined in this investigation. Such a comparison provides insight into how the arrangement of the electron-withdrawing substituents on the phenyl ring impacts upon the molecular structures of NBN.

6.1 Experimental details

The broadband rotational spectrum of 2- and 3-NBN was recorded using the COMPACT spectrometer, for a detailed description of the set-up refer to Section 3.2. Both samples were purchased from Sigma-Aldrich ($\geq 98\%$) and were used without further purification. For both measurements the separate samples were placed into the reservoir of the nozzle and heated to approximately 130°C . Neon was used as the carrier gas, at a backing pressure of 2.5 bar. Each mixture was supersonically expanded into the vacuum chamber via a pulsed nozzle at a repetition rate of 9 Hz. After supersonic expansion the ensembles were excited by a $4\ \mu\text{s}$ long microwave chirp spanning 2–8 GHz, which was amplified by the TWT amplifier at 50% gain corresponding to an output power of approximately 75 W.

The molecular responses in the form of FIDs were recorded for $40\ \mu\text{s}$ resulting in a spectral resolution of 25 kHz. In the case of 2-NBN, approximately 5 million acquisitions were recorded over approximately 19 hours, and after Fourier transformation a rotational spectrum with a signal to noise (S:N) ratio of 4000:1 was produced. For 3-NBN, approximately 3.1 million acquisitions were recorded over approximately 12 hours, and after Fourier transformation a similar S:N ratio was produced. The S:N ratios of both spectra were fully sufficient to observe the singly substituted ^{13}C -, ^{15}N -, and ^{18}O -isotopologues in their natural abundances of 1.1%,

0.36%, and 0.2%, respectively.

6.2 Results and discussion

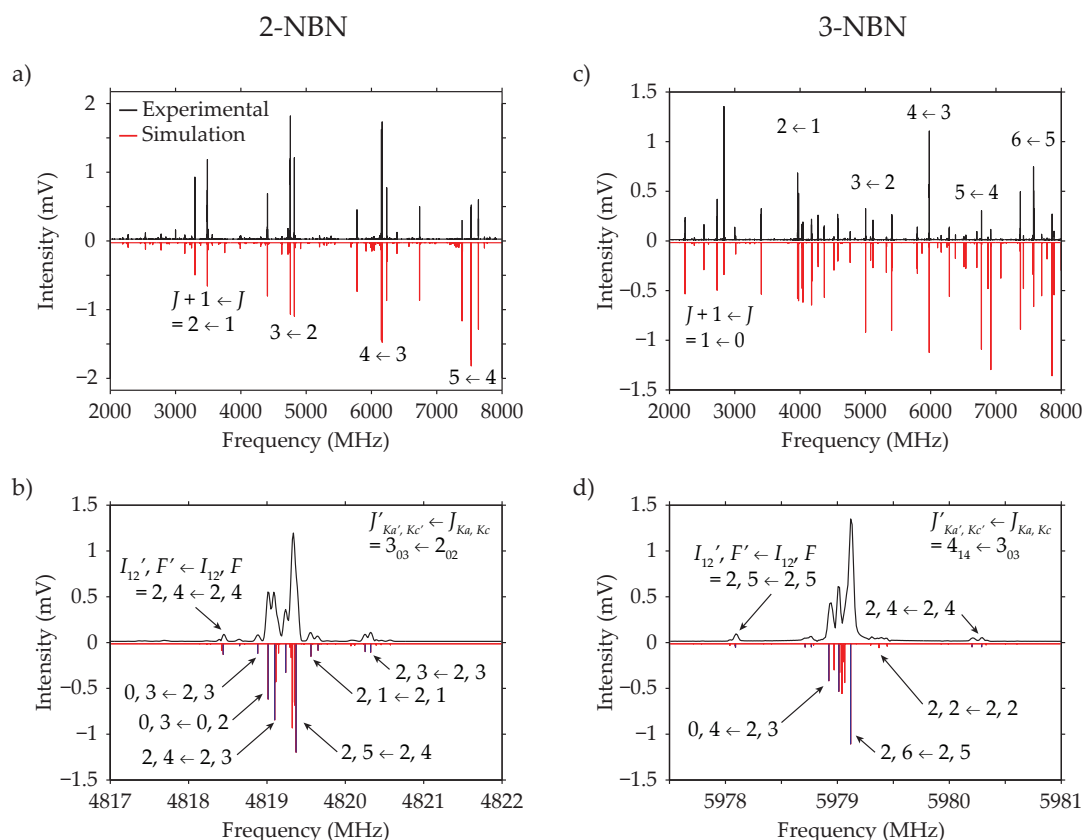


Figure 6.1: Broadband rotational spectra of (a) 2-NBN and (c) 3-NBN. Nuclear quadrupole coupling splitting due to the N_{11} (nitro) and N_{15} (nitrile) atoms of (b) 2-NBN and (d) 3-NBN. The F and I_{12} quantum numbers for the $J'_{Ka', Kc'} \leftarrow J_{Ka, Kc} = 3_{03} \leftarrow 2_{02}$ (b) and $4_{14} \leftarrow 3_{03}$ (d) transitions are also displayed. For each plot the lower trace (red/blue) represents a simulation of the fitted spectroscopic parameters reported in Table 6.1 and has been given an offset for better visibility of the S:N ratio of the experimental spectrum (black). Blue lines included in plots (b) and (d) indicate which lines were assigned, due to the high line density the red lines of these plots were not assigned.

The broadband rotational spectra of 2- and 3-NBN measured with the TWT

amplifier at 50% gain and the corresponding fits to the asymmetric-rotor Hamiltonian operators are displayed in Fig. 6.1(a) and 6.1(c), respectively. Structure optimization calculations were carried out in Gaussian09 for all three NBN molecules using the aug-cc-pVTZ basis set with the B3LYP hybrid functional including and excluding Grimme's empirical dispersion (GD3BJ). Including Grimme's empirical dispersion resulted in only minor differences to the parameters obtained when it was excluded, thus the following discussion relies on the information obtained via the B3LYP/aug-cc-pVTZ calculations for comparison purposes. The obtained rotational parameters, including the nuclear quadrupole coupling constants, of each NBN molecule are listed in Table 6.1. After assignment of the strong *a*- and *b*-type transitions for 2- and 3-NBN, respectively, the quantum-chemical rotational parameters could be directly compared to those determined experimentally. This assignment was performed with the program PGOPHER [119]. It is important to note that for comparison purposes later the quantum-chemical calculations employed do not consider zero-point vibration. The rotational quantum numbers involved in the assigned transitions range from $J = 1$ up to $J = 9$ for 2-NBN, and from $J = 1$ up to $J = 10$ for 3-NBN. In total 295 lines were assigned for the main isotopologue, the parent molecule, of 2-NBN with an average error of the fit of 3.3 kHz. For the parent molecule of 3-NBN, 256 lines were assigned with an average error of the fit of 3.2 kHz.

Table 6.1: Spectroscopic constants of 2-, 3-, 4-nitrobenzonitrile (NBN) determined experimentally and via quantum-chemical calculations. N₁₁ refers to the nitrogen atom of the nitro group and N₁₅ to the nitrogen atom of the nitrile group. For a detailed labelling of the atoms refer to Figures 6.2(b), 6.2(d), and 6.2(e).

Parameter	Experiment		B3LYP/aug-cc-pVTZ			B3LYP(GD3BJ)/aug-cc-pVTZ		
	2-NBN	3-NBN	2-NBN	3-NBN	4-NBN	2-NBN	3-NBN	4-NBN
A [MHz]	1506.54905(6)	2269.92862(9)	1499.04	2282.75	3985.67	1504.33	2285.42	3986.58
B [MHz]	1240.80389(6)	749.97847(4)	1254.69	751.43	593.84	1256.42	752.90	595.16
C [MHz]	685.25294(5)	563.99011(3)	683.01	565.33	516.84	684.62	566.33	517.85
D _K [kHz]	0.483(7)
D _{JK} [kHz]	0.173(4)
D _J [kHz]	0.060(1)
χ_{aa} (N ₁₁) [MHz]	-0.779(1)	-0.727(2)	-0.9335	-0.8777	-1.1533	-0.9390	-0.8832	-1.1619
χ_{bb-cc} (N ₁₁) [MHz]	-0.470(3)	-0.766(3)	-1.0777	-1.2983	-1.0238	-1.0794	-1.3006	-1.0233
χ_{aa} (N ₁₅) [MHz]	-0.401(1)	-2.518(1)	-0.2163	-2.8007	-4.8451	-0.2691	-2.8040	-4.8479
χ_{bb-cc} (N ₁₅) [MHz]	-4.197(2)	-1.528(2)	-5.2325	-1.7141	0.1309	-5.2073	-1.7158	0.1286
$\mu_a/\mu_b/\mu_c$ [D]	6.69/1.94/0	0.14/4.38/0	0.09/0/0	6.70/1.90/0	0.14/4.38/0	0.09/0/0
N _{lines}	295	256
σ [kHz]	3.3	3.2

A 50% gain of the TWT amplifier (corresponding to an output power of approximately 75 W) is utilized in this study to prevent population transfer/inversion and stepwise multi-resonance effects, which have been previously observed for other molecules with large dipole moments and high excitation powers (see Section 5.1.2). A lower gain can prevent these population-altering effects and lead to a better agreement of transition intensities with those predicted by PGOPHER, thus simplifying the assignment. The rotational temperature of the simulated spectra was set to 1 K, which is the approximate temperature of a supersonically expanded sample of NBN seeded with neon in the experimental set-up. The recorded spectra differ noticeably for each NBN molecule. 2-NBN, a near-oblate molecule with a large μ_a , produces a clear *a*-type spectrum (Fig. 6.1(a)), whereas 3-NBN, a near-prolate molecule with a large μ_b , produces a more congested *b*-type spectrum that is harder to recognize (Fig. 6.1(c)). For 2-NBN, the measured transition intensities agree reasonably well with those predicted, which is not the case for 3-NBN. The measured transition intensities between 5 and 8 GHz for 3-NBN are clearly weaker than those predicted with PGOPHER. This cannot be a temperature effect, as adjusting the temperature within the range of what is normal for a supersonically expanded sample seeded in neon (1–2 K) offers no improvement to the agreement of transition intensities of 3-NBN. As 3-NBN has a smaller dipole moment (4.38 D) compared to 2-NBN (6.97 D), and the TWT amplifier is less intense at the edges of this frequency range compared to the centre, a larger gain might have been more appropriate. Irrespective of the mismatch in transition intensities a large number of the transitions within the 5–8 GHz frequency range could be reliably assigned, because of the high frequency resolution offered by CP-FTMW spectroscopy.

A closer look at the hyperfine structure of 2-NBN due to the nitrogen nuclei of the nitro and nitrile groups can be found in Figure 6.1(b). Note for the spectra that display hyperfine structure (Fig. 6.1(b) and (d)) both the red and blue lines represent the simulated spectra, and only the lines in blue were assigned. The observed hyperfine structure in Figures 6.1(b) and 6.1(d) arises from the coupling of the two nitrogen atom's nuclear charge density with the electric potential generated by the electrons and other nuclei present in the molecule. Similar to the approach described in Section 4.1.2, the most convenient scheme to describe the coupling of two nuclei that have the same, or comparable, coupling strength is the

($I_1 I_2 I_{12} J F M_F$) representation [146]. In this scheme the combined nuclear spins (I) of the nitrogen nuclei ($I_1 + I_2 = I_{12}$) couple with the molecular rotational angular momentum \mathbf{J} to give a total angular momentum of \mathbf{F} , and the new angular momentum quantum numbers are

$$I_{12} = I_1 + I_2,$$

$$F = J + I_{12}$$

Figures 6.1(b) and 6.1(d) use this coupling scheme to label the quantum numbers

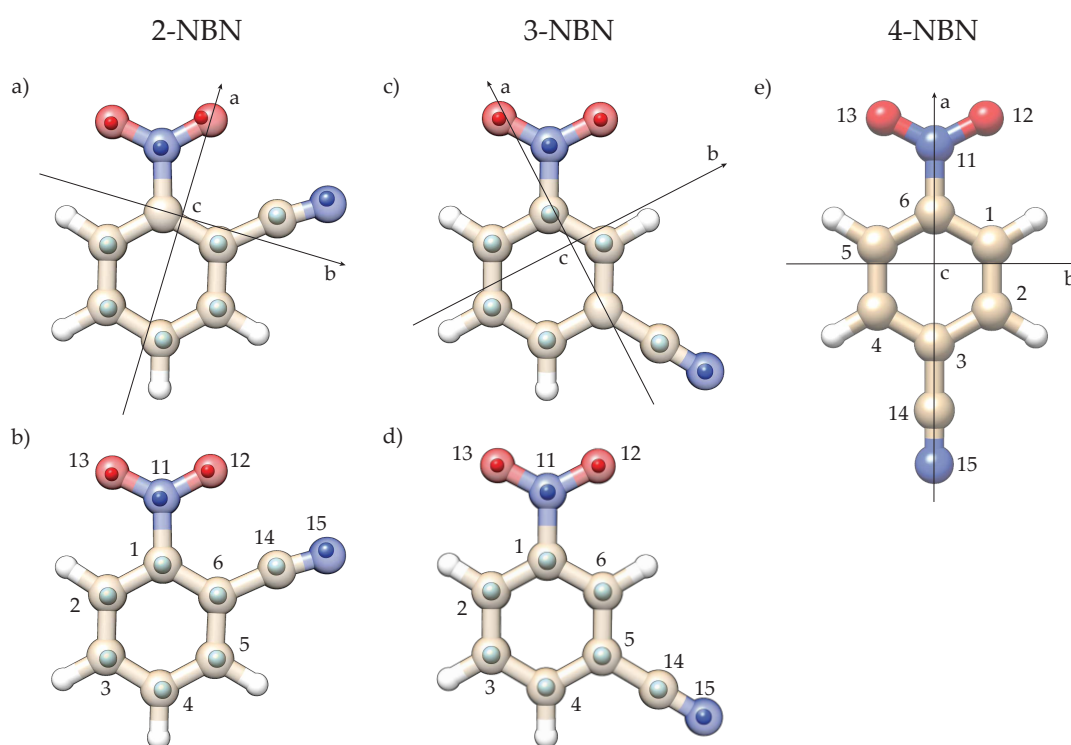


Figure 6.2: Comparison of the calculated (background) and the experimentally determined (spheres, foreground) atom positions, excluding hydrogen, for 2-NBN (a, b), and 3-NBN (c, d). The calculated molecular structure of 4-NBN is also included in (e). All calculated atom positions are obtained from B3LYP/aug-cc-pVTZ geometry optimizations. Experimental atom positions determined via the planar Kraitchman equations (r_s -structure) are given in (a) and (c), and via the mass-dependent least-squares fit approach ($r_m^{(1)}$ -structure) in (b) and (d). Also included is a reference to the inertial axis frames in (a), (c) and (e) and the atom labels in (b), (d) and (e).

involved in the observed transitions.

Nuclear quadrupole coupling constants are not only sensitive to the local electronic environment of the nucleus, but also to the orientation of the principal axis system of the molecule. Figures 6.2(a), 6.2(c), and 6.2(e) show the orientation of the principal axis system for 2-, 3-, and 4-NBN, respectively. Calculations have mostly predicted more negative values for the quadrupole coupling constants compared to those determined experimentally. The exception being the experimental χ_{aa} value of the N₁₅ atom for 2-NBN, which is almost 200 kHz more negative than the predicted value (refer to Table 6.1). For the atom labelling of 2-, 3-, and 4-NBN refer to Figures 6.2(b), 6.2(d) and 6.2(e), respectively. Note that N₁₁ and N₁₅ consistently refer to the nitrogen atoms of the respective nitro and nitrile groups.

Focusing on the experimental quadrupole coupling constants and comparing those obtained for 2-NBN with 3-NBN, the differences observed for the N₁₁ atom relative to the N₁₅ atom are much less significant. Changes to the molecular arrangement of NBN causes the principal axis system to reposition accordingly (Fig. 6.2(a, c, e)). For both 2- and 3-NBN, the N₁₁ atom lies close to the *a* inertial axis and is positioned a similar distance away from the centre of mass. The N₁₅ atom of 2-NBN lies close to the *b* inertial axis, whereas for 3-NBN, the N₁₅ atom is now positioned further away from the centre of mass and closer to the *a*-axis. Compared to the nitrile group, the nitro group of 2- and 3-NBN experiences only a slight repositioning of the principal axis system, which results in the more comparable quadrupole coupling constants of the N₁₁ atom. This repositioning can also be used to rationalise the more significant differences observed in the quadrupole coupling constants of the N₁₅ atom for 2- and 3-NBN. Changes to the structure of these molecules will also have an effect on the local electronic environment of the nitrogen nuclei and thus their respective quadrupole coupling constants. Evaluation of the structural parameters of each molecule should provide more insight into how the local electronic environments of the substituents change according to their position on the phenyl ring.

The high sensitivity of CP-FTMW spectroscopy facilitates the observation of singly substituted ¹³C-, ¹⁵N-, and ¹⁸O-isotopologues in their natural abundance for both 2- and 3-NBN. For 2-NBN the lines attributed to the isotopologues of the $J'_{K'a',K'c} \leftarrow J_{Ka,Kc} = 5_{15} \leftarrow 4_{14}$ and the $5_{05} \leftarrow 4_{04}$ transitions are displayed

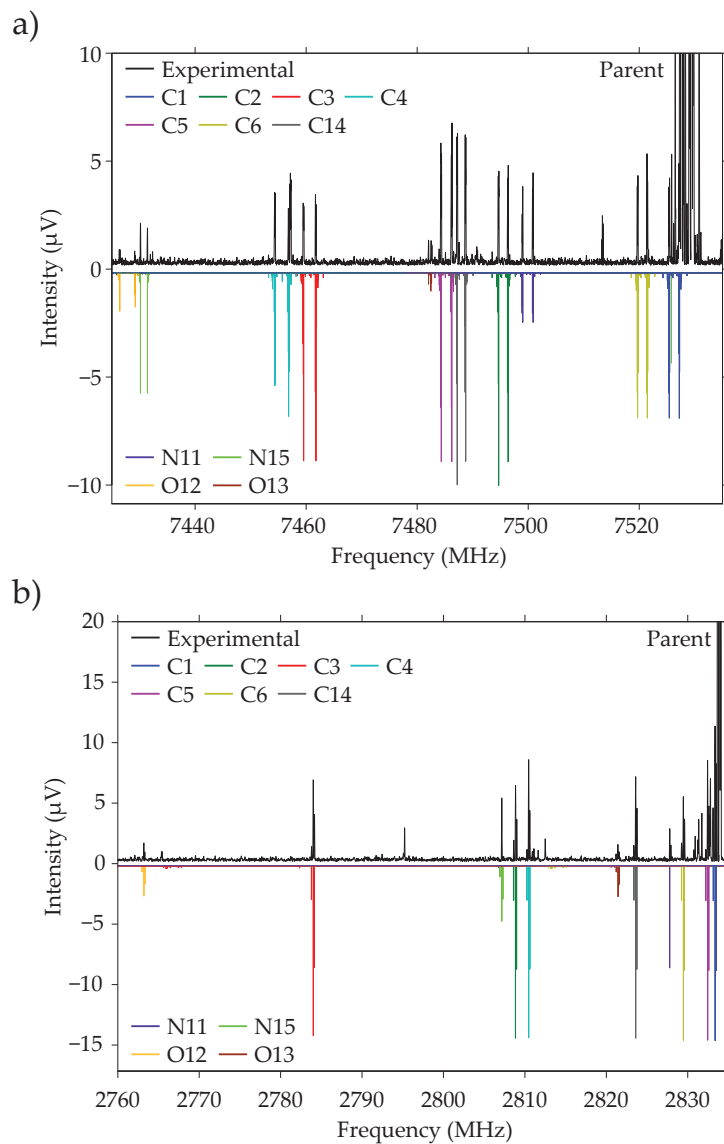


Figure 6.3: Satellite lines of singly substituted ^{13}C , ^{15}N , ^{18}O isotopologues of (a) 2-NBN and (b) 3-NBN. Displayed in (a) are the $J'_{K'a',Kc'} \leftarrow J_{Ka,Kc} = 5_{15} \leftarrow 4_{14}$ and $5_{05} \leftarrow 4_{04}$ transitions, and displayed in (b) is the $1_{11} \leftarrow 0_{00}$ transition.

Table 6.2: Rotational constants determined from the assignment for each isotopologue of 2-NBN. Also included are the number of lines assigned for each isotopologue (N_{lines}) and the average error of the assignments (σ), which are needed for the subsequent Kraitchman calculations used to determine the substituted structure (r_s).

Parameter	Parent	C ₁	C ₂	C ₃	C ₄	C ₅
A [MHz]	1506.54905(6)	1505.4258(7)	1497.068(1)	1502.033(1)	1506.133(2)	1499.774(2)
B [MHz]	1240.80389(6)	1240.8079(4)	1237.3824(5)	1223.6301(4)	1219.4405(4)	1232.4606(6)
C [MHz]	685.0571(4)	685.0565(1)	682.2410(4)	679.0555(3)	678.5957(3)	681.3052(5)
D _K [kHz]	0.483(7)	0.42(1)	1.2(2)	1.4(1)	0.7(1)	0.8(2)
D _{JK} [kHz]	0.173(4)	-0.16(5)	-0.4(1)	-0.08(5)	0.2(1)	-0.2(1)
D _J [kHz]	0.060(1)	0.08(1)	0.03(1)	0.03(1)	0.01(2)	0.004(16)
χ_{aa} (N ₁₁) [MHz]	-0.779(1)	-0.797(7)	-0.77(1)	-0.799(8)	-0.773(8)	-0.78(1)
χ_{bb-cc} (N ₁₁) [MHz]	-0.470(3)	-0.44(2)	-0.47(2)	-0.43(1)	-0.49(1)	-0.39(3)
χ_{aa} (N ₁₅) [MHz]	-0.401(1)	-0.399(9)	-0.55(1)	-0.593(7)	-0.341(6)	-0.34(2)
χ_{bb-cc} (N ₁₅) [MHz]	-4.197(2)	-4.21(1)	-4.03(2)	-4.025(9)	-4.255(8)	-4.29(2)
N _{lines}	295	84	68	101	80	70
σ [kHz]	3.3	6.3	6.1	6.4	5.9	7.9
Parameter	C ₆	N ₁₁	O ₁₂	O ₁₃	C ₁₄	N ₁₅
A [MHz]	1503.4163(8)	1502.084(1)	1505.435(2)	1466.815(2)	1490.982(1)	1473.158(1)
B [MHz]	1240.5469(4)	1235.2349(5)	1210.8082(3)	1224.6715(4)	1239.2795(3)	1234.3832(4)
C [MHz]	684.5293(1)	682.6453(2)	676.1214(2)	672.2632(2)	681.5582(2)	676.3543(2)
D _K [kHz]	1(2)	0.2(3)	3.3(2)	2.3(8)	6.2(9)	-0.7(1)
D _{JK} [kHz]	-0.61(8)	-0.06(6)	-0.44(8)	-0.2(2)	-1.6(3)	0.42(5)
D _J [kHz]	0.06(1)	0.05(1)	0.05(1)	0.00(1)	0.05(2)	0.03(1)
χ_{aa} (N ₁₁) [MHz]	-0.79(1)	...	-0.796(6)	-0.793(8)	-0.75(1)	-0.735(6)
χ_{bb-cc} (N ₁₁) [MHz]	-0.45(2)	...	-0.43(1)	-0.43(2)	-0.49(2)	-0.50(1)
χ_{aa} (N ₁₅) [MHz]	-0.384(9)	-0.295(5)	-0.359(7)	-0.19(1)	-0.503(9)	...
χ_{bb-cc} (N ₁₅) [MHz]	-4.22(1)	-4.305(9)	-4.25(9)	-4.68(2)	-4.11(1)	...
N _{lines}	65	52	44	40	66	47
σ [kHz]	5.6	5.2	3.4	3.9	6.9	5.6

Table 6.3: Rotational constants determined from the assignment for each isotopologue of 3-NBN. Also included are the number of lines assigned for each isotopologue (N_{lines}) and the average error of the assignments (σ), which are needed for the subsequent Kraitchman calculations used to determine the substituted structure (r_s).

Parameter	Parent	C ₁	C ₂	C ₃	C ₄	C ₅
A [MHz]	2269.92862(9)	2269.8100(5)	2246.7476(4)	2223.0867(4)	2249.3747(3)	2269.9558(3)
B [MHz]	749.97847(4)	749.2439(2)	749.2355(2)	749.7859(3)	747.1401(2)	747.3525(2)
C [MHz]	563.99011(3)	563.5674(2)	562.1295(2)	560.9442(2)	561.1126(2)	562.5056(2)
χ_{aa} (N_{11}) [MHz]	-0.727(2)	-0.720(9)	-0.718(9)	-0.679(9)	-0.73(1)	-0.718(7)
χ_{bb-cc} (N_{11}) [MHz]	-0.766(3)	-0.77(1)	-0.77(1)	-0.79(1)	-0.77(1)	-0.769(8)
χ_{aa} (N_{15}) [MHz]	-2.518(1)	-2.521(8)	-2.521(7)	-2.498(6)	-2.483(6)	-2.506(5)
χ_{bb-cc} (N_{15}) [MHz]	-1.528(2)	-1.496(9)	-1.501(8)	-1.533(8)	-1.544(7)	-1.524(6)
N_{lines}	262	67	99	93	86	87
σ [kHz]	3.2	6.4	7.6	7.3	6.2	5.6
Parameter	C ₆	N ₁₁	O ₁₂	O ₁₃	C ₁₄	N ₁₅
A [MHz]	2265.7923(3)	2266.8347(3)	2208.6543(6)	2269.5166(6)	2264.7342(3)	2252.9016(3)
B [MHz]	749.8961(2)	744.9908(2)	740.0299(2)	728.8255(3)	741.5529(2)	734.6684(2)
C [MHz]	563.6895(2)	560.9750(2)	554.5656(2)	551.9265(2)	558.8962(2)	554.2600(1)
χ_{aa} (N_{11}) [MHz]	-0.723(8)	...	-0.80(2)	-0.70(1)	-0.721(8)	-0.717(6)
χ_{bb-cc} (N_{11}) [MHz]	-0.79(1)	...	-0.71(1)	-0.75(2)	-0.767(9)	-0.765(7)
χ_{aa} (N_{15}) [MHz]	-2.521(5)	-2.496(8)	-2.40(2)	-2.51(1)	-2.541(5)	...
χ_{bb-cc} (N_{15}) [MHz]	-1.511(7)	-1.559(8)	-1.58(1)	-1.50(1)	-1.500(6)	...
N_{lines}	90	63	43	45	106	51
σ [kHz]	6.2	5.5	5.8	6.5	6.2	4.5

in Fig. 6.3(a). Lines for the isotopologues of the $1_{11} \leftarrow 0_{00}$ transition for 3-NBN are displayed in Fig. 6.3(b). The number of lines assigned and the rotational constants derived from the fits of each isotopologue for 2- and 3-NBN are summarized in Tables 6.2 and 6.3, respectively. With this information, like in Sections 4.1 and 5.1, both the substituted (r_s) and mass-dependent ($r_m^{(1)}$) coordinates for each of the listed atoms could be determined and compared with the equilibrium (r_e) coordinates obtained via quantum-chemical calculations and with each other. The r_e -structure corresponds to a hypothetical equilibrium structure at a potential energy minimum without zero-point vibration.

Table 6.4: Experimentally determined and calculated bond lengths of 2-NBN; r_s -structure (Kraitchman's planar equations), $r_m^{(1)}$ -structure (mass-dependent least-square fit), r_e -structures (B3LYP/aug-cc-pVTZ including and excluding GD3BJ).

Bond lengths	Planar r_s (Å)	$r_m^{(1)}$ (Å)	B3LYP r_e (Å)	B3LYP(GD3BJ) r_e (Å)
C ₁ –C ₂	...	1.386(4)	1.386	1.385
C ₂ –C ₃	1.398(2)	1.387(5)	1.387	1.386
C ₃ –C ₄	1.397(5)	1.390(8)	1.390	1.390
C ₄ –C ₅	1.391(3)	1.386(5)	1.386	1.385
C ₅ –C ₆	1.419(5)	1.401(3)	1.401	1.400
C ₆ –C ₁	...	1.402(1)	1.402	1.401
C ₁ –N ₁₁	...	1.471(3)	1.479	1.477
N ₁₁ –O ₁₂	1.110(2)	1.205(7)	1.218	1.218
N ₁₁ –O ₁₃	1.220(2)	1.203(7)	1.221	1.221
O ₁₂ ···O ₁₃	1.985(4)	2.137(9)	2.166	2.166
C ₆ –C ₁₄	1.431(4)	1.439(4)	1.430	1.429
C ₁₄ –N ₁₅	1.159(2)	1.152(6)	1.152	1.151

The r_s -coordinates for 2-NBN were calculated with the KRA program [149] using Kraitchman's equations [14]. For a molecule that displays a large inertial

defect ($\Delta = I_c - I_a - I_b$), it is normal protocol to employ the non-planar approach when applying Kraitchman's equations. Inertial defects are usually a result of out-of-plane hydrogens or low-lying out-of-plane vibrations, or even a combination of both [167, 191]. Although 2-NBN has an inertial defect of $-5.24 \mu\text{\AA}^2$ the majority of the r_s -coordinates generated with the non-planar approach produce imaginary components. For this reason, only the r_s -structure determined via the planar approach is reported here (refer to Tables 6.4 and 6.5). It has been previously reported that the position of an atom with respect to the molecule's centre of mass or the molecule's inertial axes can impact upon the reliability of the r_s -coordinates determined [167, 192]. Similar issues have also been encountered in Sections 4.1.2 and 5.1.2. In spite of this behaviour and the large inertial defect,

Table 6.5: Experimentally determined and calculated bond angles of 2-NBN; r_s -structure (Kraitchman's planar equations), $r_m^{(1)}$ -structure (mass-dependent least-square fit), r_e -structure (B3LYP/aug-cc-pVTZ including and excluding GD3BJ).

Bond angles	Planar r_s ($^\circ$)	$r_m^{(1)}$ ($^\circ$)	B3LYP r_e ($^\circ$)	B3LYP(GD3BJ) r_e ($^\circ$)
$\angle C_1C_2C_3$...	119.8(2)	119.78	119.72
$\angle C_2C_3C_4$	120.1(1)	119.9(3)	119.91	119.93
$\angle C_3C_4C_5$	120.1(1)	120.2(3)	120.18	120.20
$\angle C_4C_5C_6$	120.5(2)	120.9(3)	120.93	120.84
$\angle C_5C_6C_1$...	117.8(2)	117.83	117.91
$\angle C_6C_1C_2$...	121.4(2)	121.37	121.41
$\angle C_2C_1N_{11}$...	117.5(2)	117.52	117.60
$\angle C_1N_{11}O_{12}$...	117.5(2)	117.54	117.51
$\angle C_1N_{11}O_{13}$...	117.3(4)	117.34	117.33
$\angle O_{12}N_{11}O_{13}$	116.8(2)	125.1(5)	125.12	125.15
$\angle C_5C_6C_{14}$	116.1(2)	116.6(2)	116.66	116.71
$\angle C_6C_{14}N_{15}$	173.4(2)	171.7(5)	171.70	171.65

the planar approach only generates an imaginary component for the C_1 atom of 2-NBN. Thus structural parameters that rely on the position of the C_1 atom could not be evaluated, whereas all the other r_s coordinates for heavy atoms could be evaluated. The determined r_s -structure of 2-NBN produces some unexpected behaviour, especially for the nitro group where the $r_s(N_{11}-O_{13})$ bond length is over 0.1 \AA larger than the $N_{11}-O_{12}$ bond length. Although some degree of steric interaction between the nitrile and nitro group of 2-NBN might be expected, it is unlikely to be to the extent that the r_s -structure indicates. Instead of only one bond reducing in length, it is more plausible that both reduce in length in order to maintain the symmetry of the resonance structure for the nitro group. Differences in the determined $r_s(N-O)$ bond lengths for molecules with a nitro group are not uncommon, especially for molecules similar in size to NBN where the mass of the nitro group plays a significant role in determining the orientation of the molecule's inertial axis system. When comparing the structural parameters of a nitro group between molecules, the $O \cdots O$ distances are often used instead of the $N-O$ distances [168, 169, 189].

For 2-NBN, a value of $1.985(4) \text{ \AA}$ is determined for the $r_s(O \cdots O)$ distance. Although this distance has a relatively small uncertainty value, it should be considered with care as it does not follow any logical trend when considering the $O \cdots O$ distances reported for other nitro containing molecules [169]. More importantly, the $r_s(O \cdots O)$ distance deviates significantly from the determined $r_m^{(1)}$ ($2.137(9) \text{ \AA}$) and calculated r_e (2.166 \AA) $O \cdots O$ distances of this investigation. Cox and Waring [169] list the structural parameters reported for a series of molecules containing a nitro group ($R-NO_2$), and discuss how the electronegativity of the attached group (R) affects these parameters. One of the largest $O \cdots O$ distances reported was 2.188 \AA for NO_2F [193], where the R group (fluorine) is extremely electronegative. At the opposite end of the scale, the smallest $O \cdots O$ distance of 2.090 \AA was reported for NO_2^- and determined via a neutron diffraction study [194]. The electronegativity of benzonitrile falls between these two extremes, yet the $r_s(O \cdots O)$ distance determined for 2-NBN is considerably smaller than the distance reported for NO_2^- .

A mass-dependent structural fit is less susceptible to the effects that reduce the accuracy of the r_s -coordinates as it takes into account the inertial defect. This

approach can be employed to yield the $r_m^{(1)}$ geometry. For 2-NBN, a least-squares fit of the structure to the rotational constants and additional parameters was performed in the STRFIT program [149]. The additional parameters ($c_a = 0.05(2)$ and $c_b = 0.32(2) \mu^{1/2} \text{Å}$) account for the isotope-dependent rovibrational contribution to the molecule's moments of inertia [138]. From the least-squares fit method we obtain a complete set of reliable structural parameters, which can be directly compared to those determined via quantum-chemical calculations (refer to Tables 6.4 and 6.5). The $r_m^{(1)}$ -coordinates produce the expected resonance structure for the nitro group, as both the N–O bonds are essentially equivalent within the errors, and also a more realistic O \cdots O distance of 2.137(9) Å. Interestingly, the more reasonable $r_m^{(1)}$ (O \cdots O) value determined here is still considerably smaller than those reported for other nitrobenzene derivatives. For example, 4-nitroanisole (NO₂C₆H₄OCH₃) displays an $r_m^{(1)}$ (O \cdots O) distance of 2.167(3) Å [189], which is larger than the distance determined for 2-NBN by approximately 0.03 Å. Considering that benzonitrile is a more electronegative moiety than anisole, a larger O \cdots O might be expected for 2-NBN. However, the steric interaction of the nitro and nitrile substituents restricts the O \cdots O distance in 2-NBN, this is made especially clear by the increase in the $r_m^{(1)}$ (O \cdots O) distance observed for 3-NBN (2.185(6) Å).

A recent gas electron diffraction study of nitroxoline reports an alternative consequence of steric interaction between a nitro group and the hydrogen atom of a neighbouring aromatic ring in the form of dihedral angle [195]. The nitro group of nitroxoline is twisted by an angle of $8 \pm 3^\circ$ with respect to the plane of the aromatic ring it is bonded too. For 2-NBN, there is no such twisting of the nitro group observed, instead it is the bond lengths and angles of the respective substituents that are most affected. The quantum-chemical calculations applied in this investigation predict the structural parameters of the phenyl ring quite accurately, but appear limited when considering the influence of these highly electronegative, neighbouring substituents. Calculations have overestimated each of the bond lengths and distances of the nitro group (including C₁–N₁₁, N₁₁–O₁₂, N₁₁–O₁₃ and O₁₂ \cdots O₁₃, refer to Table 6.4) for 2-NBN.

In the case of 3-NBN these limitations are less apparent, although there are still discrepancies observed for the nitro group (see Table 6.6). According to the

experimentally determined rotational constants of 3-NBN, the magnitude of its inertial defect ($-0.42 \mu\text{\AA}^2$) is significantly smaller than that of 2-NBN. The smaller inertial defect, however, does not prevent the planar approach of Kraitchman's equations from producing an imaginary component for the C_5 atom. Thus, structural parameters that involve the C_5 atom could not be evaluated. When performing the least-squares fit method for 3-NBN the additional parameter included was $c_a = 0.030(4) \mu^{1/2}\text{\AA}$. Both methods used to provide experimentally determined structures for 3-NBN produce structural parameters that adhere to the expected resonance structure of the nitro group. Although the nitro groups of the experimentally determined structures are very similar, the structures of the phenyl ring differ quite significantly. The determined r_s -coordinates for the phenyl ring

Table 6.6: Experimentally determined and calculated bond lengths of 3-NBN; r_s -structure (Kraitchman's planar equations), $r_m^{(1)}$ -structure (mass-dependent least-square fit), r_e -structure (B3LYP/aug-cc-pVTZ including and excluding GD3BJ).

Bond lengths	Planar r_s (Å)	$r_m^{(1)}$ (Å)	B3LYP r_e (Å)	B3LYP(GD3BJ) r_e (Å)
C ₁ –C ₂	1.41(1)	1.387(3)	1.387	1.386
C ₂ –C ₃	1.393(4)	1.389(3)	1.389	1.388
C ₃ –C ₄	1.395(3)	1.387(3)	1.387	1.387
C ₄ –C ₅	...	1.400(2)	1.400	1.399
C ₅ –C ₆	...	1.396(1)	1.396	1.395
C ₆ –C ₁	1.318(9)	1.384(2)	1.384	1.383
C ₁ –N ₁₁	1.477(7)	1.483(4)	1.480	1.478
N ₁₁ –O ₁₂	1.228(3)	1.232(5)	1.220	1.220
N ₁₁ –O ₁₃	1.231(6)	1.230(6)	1.221	1.221
O ₁₂ ···O ₁₃	2.183(9)	2.185(6)	2.166	2.167
C ₅ –C ₁₄	...	1.431(2)	1.431	1.429
C ₁₄ –N ₁₅	1.157(1)	1.152(3)	1.152	1.151

produces an incomplete structure with larger errors. Similar to 2-NBN, the $r_m^{(1)}$ -structure of the phenyl ring is closely matched by the predicted equilibrium (r_e) structure, and it is now the nitro group alone where discrepancies arise. For a direct comparison between the experimentally determined and calculated atom positions for 2-NBN and 3-NBN refer to Figure 6.2.

Comparing the structural parameters for the phenyl rings of the different NBN molecules can provide information on the electron-withdrawing strength of the respective substituents. As previously mentioned the experimental $r_m^{(1)}$ parameters of the phenyl ring for both 2- and 3-NBN are in good agreement with the calculated parameters. Thus, the parameters predicted for the phenyl ring of 4-NBN with quantum-chemical calculations (Table 6.8) can be used to validate the observation

Table 6.7: Experimentally determined and calculated bond angles of 3-NBN; r_s -structure (Kraitchman's planar equations), $r_m^{(1)}$ -structure (mass-dependent least-square fit), r_e -structure (B3LYP/aug-cc-pVTZ including and excluding GD3BJ).

Bond angles	Planar r_s ($^\circ$)	$r_m^{(1)}$ ($^\circ$)	B3LYP r_e ($^\circ$)	B3LYP(GD3BJ) r_e ($^\circ$)
$\angle C_1C_2C_3$	117.7(2)	118.6(2)	118.66	118.66
$\angle C_2C_3C_4$	120.3(1)	120.4(1)	120.38	120.36
$\angle C_3C_4C_5$...	120.1(2)	120.06	120.03
$\angle C_4C_5C_6$...	120.1(1)	120.14	120.21
$\angle C_5C_6C_1$...	118.4(1)	118.35	118.27
$\angle C_6C_1C_2$	124.6(5)	122.4(1)	122.42	122.47
$\angle C_2C_1N_{11}$	116.6(5)	119.0(2)	118.96	118.94
$\angle C_1N_{11}O_{12}$	116.4(5)	117.5(4)	117.50	117.47
$\angle C_1N_{11}O_{13}$	118.5(7)	117.4(3)	117.36	117.36
$\angle O_{12}N_{11}O_{13}$	125.4(4)	125.1(5)	125.14	125.17
$\angle C_4C_5C_{14}$...	120.0(1)	119.97	119.93
$\angle C_5C_{14}N_{15}$...	179.6(3)	179.57	179.57

of possible trends. The carbon-carbon (C–C) bond lengths of the phenyl ring differ noticeable for each NBN molecule (refer to Tables 6.4, 6.6 and 6.8). For each NBN molecule, the longest of the C–C bonds for the phenyl ring are consistently bonded to the nitrile group. This is a strong indicator that the nitro group is the most electron-withdrawing of the two substituents.

When comparing the structures of 2-, 3-, and 4-NBN we consider the structures obtained via the least-squares fitting method as well as those obtained via quantum-chemical calculations (Table 6.2). The calculated structural parameters of both substituents are almost unchanged regardless of their respective positions on the phenyl ring. However, this is contradictory to the experimental structures. The nitro group of NBN is what exhibits the most noticeable structural changes according to its position. For the nitrile group, the most revealing difference is in

Table 6.8: Calculated r_e bond lengths and angles of 4-NBN using the aug-cc-pVTZ basis set with the B3LYP hybrid functional including and excluding Grimme’s empirical dispersion (GD3BJ).

Bond lengths	B3LYP r_e (Å)	B3LYP(GD3BJ) r_e (Å)	Bond angles	B3LYP r_e (°)	B3LYP(GD3BJ) r_e (°)
C ₁ –C ₂	1.385	1.383	∠C ₁ C ₂ C ₃	119.91	119.85
C ₂ –C ₃	1.399	1.399	∠C ₂ C ₃ C ₄	120.30	120.40
C ₃ –C ₄	1.399	1.399	∠C ₃ C ₄ C ₅	119.91	119.85
C ₄ –C ₅	1.385	1.383	∠C ₄ C ₅ C ₆	118.78	118.74
C ₅ –C ₆	1.387	1.386	∠C ₅ C ₆ C ₁	122.32	122.41
C ₆ –C ₁	1.387	1.386	∠C ₆ C ₁ C ₂	118.78	118.74
C ₆ –N ₁₁	1.478	1.478	∠C ₅ C ₆ N ₁₁	118.84	118.80
N ₁₁ –O ₁₂	1.221	1.221	∠C ₆ N ₁₁ O ₁₂	117.45	117.44
N ₁₁ –O ₁₃	1.221	1.221	∠C ₆ N ₁₁ O ₁₃	117.45	117.44
O ₁₂ ···O ₁₃	2.167	2.167	∠O ₁₂ N ₁₁ O ₁₃	125.09	125.12
C ₃ –C ₁₄	1.430	1.429	∠C ₄ C ₃ C ₁₄	119.85	119.80
C ₁₄ –N ₁₅	1.152	1.152	∠C ₃ C ₁₄ N ₁₅	180.00	180.00

the $\angle\text{CCN}$ value. Here, 2-NBN exhibits a significant deviation from 180° for the $\angle\text{CCN}$ angle, where 3- and 4-NBN display the opposite behaviour (see Table 6.2). This observation is attributed to the steric interaction with the neighbouring nitro group. The experimental value for the $\angle\text{CCN}$ angle of 3-NBN ($179.6(3)^\circ$) is essentially the same as the $\angle\text{CCN}$ angle reported for 4-NBN ($179(1)^\circ$) in the X-ray crystallography study [190]. Thus, the *meta* position is already a sufficient distance away from the nitro group to prevent this steric interaction. Another consequence of the steric interaction is the restricting effect it has on the structure of the nitro group.

For the nitro group it is important to note that its structural parameters are especially sensitive to changes in its local electron density [169, 189]. In general, increasing the electronegativity of the species connected to the nitro group re-

Table 6.9: Comparison of selected structural parameters determined experimentally for 2- and 3-NBN with those determined via quantum-chemical calculations for 4-NBN, as well as a selection taken from an X-ray crystallography study [190]. All quantum chemical calculations utilize the B3LYP hybrid functional with the aug-cc-pVTZ basis set.

Parameter ^a	2-NBN		3-NBN		4-NBN	
	$r_m^{(1)}$	B3LYP	$r_m^{(1)}$	B3LYP	X-ray [190]	B3LYP
C–NO ₂	1.471(3)	1.479	1.483(4)	1.480	1.483(13)	1.480
N–O ^b	1.204(6)	1.220	1.231(6)	1.220	1.214(15)	1.220
O···O	2.137(9)	2.166	2.185(6)	2.166	...	2.167
$\angle\text{ONO}$	125.1(5)	123.12	125.1(5)	125.14	124(1)	125.09
C–CN	1.439(4)	1.430	1.431(2)	1.431	1.438(12)	1.430
C–N	1.152(6)	1.152	1.152(3)	1.152	1.155(15)	1.152
$\angle\text{CCN}$	171.7(5)	171.70	179.6(3)	179.57	179(1)	180.00

^a Bond lengths in Å and angles in degrees.

^b Average of the two N–O bond lengths obtained.

sults in changes to its structure, such as a decrease in the N–O bond length and an increase in the ONO angle and the O···O distance. The smaller $r_m^{(1)}(\text{N–O})$ bond length of 2-NBN (1.204(6) Å) compared to 3-NBN (1.231(6) Å) suggests this change to the structural arrangement of NBN could be considered as equivalent to an increase in electronegativity of the benzonitrile moiety. A smaller $r_m^{(1)}(\text{O···O})$ distance of 2-NBN (2.137(9) Å) compared to 3-NBN (2.185(6) Å) would seem to negate this. However, considering the magnitude of the decrease in $r_m^{(1)}(\text{N–O})$ bond lengths and the constant $r_m^{(1)}(\angle\text{ONO})$ angle observed (125.1(5)°), it is likely that the aforementioned steric interaction prevents an increase in the O···O distance of 2-NBN. Thus, the observed changes can still be rationalised by an effective increase in electronegativity moving from the *meta*- to the *ortho*-benzonitrile configuration, which forces the nitro and nitrile substituents to compete more directly for the electron density of the phenyl ring.

6.3 Conclusions

The high-resolution broadband spectra of 2- and 3-NBN were recorded. For both molecules singly substituted ^{13}C , ^{15}N , and ^{18}O isotopologues in their natural abundance were observed and subsequently assigned. The accurate rotational parameters obtained for the isotopologues meant that both the substituted (r_s) and mass-dependent least-squares fit ($r_m^{(1)}$) structures could be obtained. Results from the least-squares fitting approach provided a complete set of structural parameters for both molecules, and with reduced errors the structures were also considered more reliable. The experimentally determined structures were then compared with each other and the structures obtained via quantum-chemical calculations. Differences in the experimentally determined nuclear quadrupole coupling constants were the first indication that the local electronic environments of the nitrogen nuclei were affected by the change in the structural arrangement of NBN. After further analysis of the substituents' structural parameters, it became clear that the structure of the nitro group of NBN was sensitive to the position of the nitrile group on the phenyl ring. Significant differences in the structural parameters of the nitro group were observed when comparing 2-NBN to 3-NBN. A degree of steric interaction between the nitrile and nitro groups was detected within 2-NBN as a $\angle\text{CCN}$ angle

significantly smaller than 180° was observed. In addition to this steric interaction, having the substituents bonded to adjacent carbons on the phenyl ring also appeared to increase competition for the electron density. The consequent changes to the structure of the nitro group were then rationalised as being comparable to an increase in the electronegativity of the benzonitrile moiety when moving from the *meta* to the *ortho* configuration.

Chapter 7

Summary and Outlook

Within this thesis a series of molecules with large dipole moments (4-aminobenzonitrile, 4-nitroanisole, 2- and 3-nitrobenzonitrile) have been investigated using chirped-pulse Fourier transform microwave (CP-FTMW) spectroscopy. The high sensitivity and resolution offered by this technique facilitated the determination of the molecular structures of each molecule under investigation, which allowed for reliable and insightful analysis into the structure of the molecule. The original motivation for investigating molecules with large dipole moments was the potential application of motion manipulation techniques using AC-electric fields. Focusing, guiding, and deceleration of polar molecules in high-field-seeking states using microwave fields had already been previously demonstrated on ammonia [90–92]. To extend this technique to larger polyatomic molecules, such as the ones investigated in this thesis, would provide new and interesting possibilities for the field of cold molecules. The search for the magnitude of the electron’s electric dipole moment, parity-violations in chiral molecules, as well as the study of chemistry at ultra cold temperatures or within the interstellar medium are all examples of current research fields that would benefit from the continuing development of such techniques.

In Chapter 3 the potential experimental set-ups for each of the motion manipulation techniques discussed in Section 4.2 were described in detail, along with the set-up for the CP-FTMW (COMPACT) spectrometer. Assignment of the high-resolution broadband spectrum obtained for 4-aminobenzonitrile (4-ABN) in Chapter 4 allowed for the determination of its molecular structure. Analysis of the

data obtained confirmed a non-planar structure with two non-zero dipole moment components. Reliable assignment of the rotational spectrum also produced accurate field free rotational energy levels, which were extracted from PGOPHER [119]. The energies and dipole moment components were then used to determine the AC-Stark shifts, and later DC-Stark shifts, of 4-ABN's rotational energy levels with increasing electric field strength. The calculated AC-Stark shifts were then used in simulations that determined the feasibility of extending microwave focusing and deceleration experiments to 4-ABN. Simulations showed that such techniques would require a pre-decelerated packet ($v_z \leq 50$ m/s) of 4-ABN molecules in order to observe any focusing or decelerating effect of the microwave fields on the packet. The calculated DC-Stark shifts were also used in simulations, this time to investigate the possible application of the Stark decelerator to a specific ($J_{K_a K_c} = J_{J_0}$) rotational state of 4-ABN. Although simulations produced promising results in the form of longitudinal bunching, the total number of molecules that successfully travel the length of the Stark decelerator was limited. Practical application of the Stark decelerator to 4-ABN would therefore require some method that can increase population in the rotational state of interest.

Other potential candidates for such motion manipulation experiments include 4-nitroanisole, 2- and 3-nitrobenzotrile (NBN) as each, like 4-ABN, display favourable dipole moment to mass ratios and can be easily seeded into a molecular beam. Furthermore, neither of these molecules had been previously investigated using the CP-FTMW spectroscopy technique before this work, which allowed for unique insight into their respective structural properties and chemistry. For 4-nitroanisole (Ch. 5), the structural parameters obtained could be directly compared to the parameters of nitrobenzene and anisole in order to determine the effect that the bonded substituents have on the phenyl ring. Analysis then confirmed the presence of a "push-pull" effect in 4-nitroanisole. In addition to the spectroscopic analysis, experiments using tailored microwave pulses to transfer population between the rotational states of 4-nitroanisole were carried out. Double resonance pulse schemes were designed to transfer population as well as observe the effect this change in population had on a transition's intensity. The measured changes in intensity confirmed the successful transfer of population between rotational states, which is particularly promising when considering the need for well

populated rotational states for most forms of focusing, decelerating, and/or trapping experiments.

In Chapter 6, both 2-NBN and 3-NBN were the focus of a solely spectroscopic investigation. The experimental structures were compared with one another, as well as the calculated structure of 4-NBN. This study highlighted the structural changes to the substituents, a nitro (NO_2) and a nitrile (CN) group, brought about by changing their respective positions on the phenyl ring. A steric interaction between the nitro and nitrile group of 2-NBN encouraged changes in the structural parameters of each substituent. The observed differences were rationalized as being comparable to changes in the electronegativity of the benzonitrile moiety when moving from the *meta* to the *ortho* configuration.

Generally, CP-FTMW spectroscopy has allowed for a much more detailed understanding of the structural properties and rotational energy level structure of the molecules under investigation. Simulations have shown that the rotational energy level structure for a polar molecule of interest obtained via CP-FTMW spectroscopy can be utilised to determine the feasibility for the application of microwave or Stark deceleration techniques. The more information learned about such systems increases their viability as candidates in future motion manipulation experiments. Further work could include the practical development of alternative experimental set-ups that would be applicable to the molecules investigated throughout this thesis. The combination of a buffer-gas cell, used to produce an effusive beam of 4-ABN molecules with longitudinal velocities below 100 m/s, and a high-quality cylindrically symmetric microwave resonator would be ideal for testing the effectiveness of decelerating AC-fields on more complex systems. In addition, to confirm the feasibility of using the Stark decelerator with large polyatomic molecules, boosting the population of a J_{J_0} rotational state with tailored microwave pulses before Stark deceleration would also prove interesting. Such experimental set-ups would help to open up the ultra-cold temperature regime to a large variety of polyatomic asymmetric-top molecules.

Bibliography

- [1] W. Gordy, “Microwave spectroscopy”, *Rev. Mod. Phys.* **20**, 668 (1948) (cit. on p. 1).
- [2] C. H. Townes, “The ammonia spectrum and line shapes near 1.25 cm wavelength”, *Phys. Rev.* **70**, 665–671 (1946) (cit. on p. 1).
- [3] G. W. E., “The inversion spectrum of ammonia”, *Phys. Rev.* **70** (1946) (cit. on pp. 1, 26).
- [4] B. P. Dailey, R. L. Kyhl, M. W. P. Strandberg, J. H. Van Vleck, and E. B. W. Jr., “The hyperfine structure of the microwave spectrum of ammonia and the existence of a quadrupole moment in N^{14} ”, *Phys. Rev.* **70**, 984 (1946) (cit. on pp. 1, 26).
- [5] J. P. Gordon, H. J. Zeiger, and C. H. Townes, “Molecular microwave oscillator and new hyperfine structure in the microwave spectrum of NH_3 ”, *Phys. Rev.* **95**, 282–284 (1954) (cit. on pp. 1, 38).
- [6] J. P. Gordon, H. J. Zeiger, and C. H. Townes, “The MASER - New type of microwave amplifier, frequency standard, and spectrometer”, *Phys. Rev.* **99**, 1264–1274 (1955) (cit. on pp. 1, 38).
- [7] T. J. Balle and W. H. Flygare, “Fabry–Perot cavity pulsed Fourier transform microwave spectrometer with a pulsed nozzle particle source”, *Rev. Sci. Instrum.* **52**, 33–45 (1981) (cit. on p. 1).
- [8] J.-U. Grabow, W. Stahl, and H. Dreizler, “A multioctave coaxially oriented beam-resonator arrangement Fourier-transform microwave spectrometer”, *Rev. Sci. Instrum.* **67**, 4072–4084 (1996) (cit. on p. 2).

- [9] A. Lesarri, S. Mata, J. C. López, and J. L. Alonso, “A laser-ablation molecular-beam Fourier-transform microwave spectrometer: The rotational spectrum of organic solids”, *Rev. Sci. Instrum.* **74**, 4799 (2003) (cit. on p. 2).
- [10] E. J. Cocinero, A. Lesarri, P. Écija, F. J. Basterretxea, J.-U. Grabow, J. A. Fernández, and F. Castaño, “Ribose found in the gas phase”, *Angew. Chem. Int. Ed.* **51**, 3119–3124 (2012) (cit. on p. 2).
- [11] A. Lesarri, S. Mata, E. J. Cocinero, S. Blanco, J. C. López, and J. L. Alonso, “The structure of neutral proline”, *Angew. Chem. Int. Ed.* **41**, 4673–4676 (2002) (cit. on p. 2).
- [12] A. Lesarri, E. J. Cocinero, J. C. López, and J. L. Alonso, “The shape of neutral valine”, *Angew. Chem. Int. Ed.* **43**, 605–610 (2004) (cit. on p. 2).
- [13] G. G. Brown, B. C. Dian, K. O. Douglass, S. M. Geyer, S. T. Shipman, and B. H. Pate, “A broadband Fourier transform microwave spectrometer based on chirped pulse excitation”, *Rev. Sci. Instrum.* **79** (2008) (cit. on pp. 2, 51, 102, 105).
- [14] J. Kraitchman, “Determination of molecular structure from microwave spectroscopic data”, *Amer. J. Phys.* **21**, 17–24 (1953) (cit. on pp. 2, 54, 64, 92, 120).
- [15] C. Pérez, S. Lobsiger, N. A. Seifert, D. P. Zaleski, B. Temelso, G. C. Shields, Z. Kisiel, and B. H. Pate, “Broadband Fourier transform rotational spectroscopy for structure determination: the water heptamer”, *J. Chem. Phys. Lett.* **571**, 1–15 (2013) (cit. on pp. 2, 51, 53, 98).
- [16] Y. Zhou, D. D. Grimes, T. J. Barnum, D. Patterson, S. L. Coy, E. Klein, J. S. Muentner, and R. W. Field, “Direct detection of rydberg–rydberg millimeter-wave transitions in a buffer gas cooled molecular beam”, *Chem. Phys. Lett.* **640**, 124–136 (15) (cit. on p. 2).
- [17] S. E. Maxwell, N. Brahms, R. DeCarvalho, D. R. Glenn, J. S. Helton, S. V. Nguyen, D. Patterson, J. Petricka, D. DeMille, and J. M. Doyle, “High-flux beam source for cold, slow atoms or molecules”, *Phys. Rev. Lett.* **95** (2005) (cit. on pp. 2, 7).

- [18] J. van Veldhoven, J. Küpper, H. L. Bethlem, B. Sartakov, A. J. A. van Roij, and G. Meijer, “Decelerated molecular beams for high-resolution spectroscopy”, *Eur. Phys. J. D* **31**, 337–349 (2004) (cit. on pp. 2, 4, 11).
- [19] E. R. Hudson, H. J. Lewandowski, B. C. Sawyer, and J. Ye, “Cold molecule spectroscopy for constraining the evolution of the fine structure constant”, *Phys. Rev. Lett.* **96** (2006) (cit. on pp. 2, 4).
- [20] M. Quack, “How important is parity violation for molecular and biomolecular chirality?”, *Angew. Chem. Int. Ed.* **41**, 4618–4630 (2002) (cit. on pp. 2, 4).
- [21] H. K. Onnes, “The resistance of pure mercury at helium temperatures”, *Comm. Leiden.* (1911) (cit. on p. 2).
- [22] P. Kapitza, “Viscosity of liquid helium below the λ -point”, *Nature* **141**, 74 (1938) (cit. on p. 3).
- [23] W. Ketterle, “When atoms behave as waves: bose-einstein condensation and the atom laser (nobel lecture)”, *ChemPhysChem.* **3**, 736–753 (2002) (cit. on p. 3).
- [24] E. A. Cornell and C. E. Wieman, “Nobel lecture: bose-einstein condensation in a dilute gas, the first 70 years and some recent experiments”, *Rev. Mod. Phys.* **74**, 875–893 (2002) (cit. on p. 3).
- [25] S. Bose, “Plancks Gestz und Lichtquantenhypothese”, *Z. Phys.* **26**, 178–181 (1924) (cit. on p. 3).
- [26] I. W. M. Smith, *Low temperatures and cold molecules* (Imperial College Press, London, 2008) (cit. on p. 3).
- [27] J. J. Hudson, D. M. Kara, I. J. Smallman, M. R. Sauer, B. E. Tarbutt, and E. A. Hinds, “Improved measurement of the shape of the electron”, *Nature* **473**, 493–496 (2011) (cit. on p. 4).
- [28] I. B. Khriplovich and S. K. Lamoreaux, *CP-violation without strangeness: electric dipole moments of particles, atoms, and molecules* (Springer-Verlag, Berlin, 1997) (cit. on p. 4).

- [29] E. A. Hinds, “Testing time reversal symmetry using molecules”, *Phys. Scr.* **T70**, 34–41 (1997) (cit. on p. 4).
- [30] J. Ginges and V. Flambaum, “Violations of fundamental symmetries in atoms and tests of unification theories of elementary particles”, *Phys. Rep.* **397**, 63–154 (2004) (cit. on p. 4).
- [31] V. A. Dzuba and V. V. Flambaum, “Current trends in searches for new physics using measurements of parity violation and electric dipole moments in atoms and molecules”, *arXiv.* (2010) (cit. on p. 4).
- [32] S. Ospelkaus, K. K. Ni, D. Wang, M. H. G. de Miranda, B. Neyenhuis, G. Quémener, P. S. Julienne, J. L. Bohn, D. S. Jin, and J. Ye, “Quantum-state controlled chemical reactions of ultracold potassium-rubidium molecules”, *Science* **327**, 853–857 (2010) (cit. on pp. 4, 5).
- [33] K. K. Ni, S. Ospelkaus, D. Wang, G. Quémener, B. Neyenhuis, M. H. G. de Miranda, J. L. Bohn, J. Ye, and J. D. S., “Dipolar collisions of polar molecules in the quantum regime”, *Nature* **464**, 1324–1328 (2010) (cit. on p. 4).
- [34] M. Schnell and G. Meijer, “Cold molecules: preparation, applications, and challenges”, *Angew. Chem. Int. Ed.* **48**, 6010–6031 (2009) (cit. on p. 4).
- [35] M. Hummon, W. Campbell, H. I. Lu, E. Tsikata, Y. Wang, and J. M. Doyle, “Magnetic trapping of atomic nitrogen (^{14}N) and cotrapping of NH ($X^3\Sigma^-$)”, *Phys. Rev. A* **78** (2008) (cit. on p. 4).
- [36] E. R. Meyer, J. L. Bohn, and M. P. Deskevich, “Candidate molecular ions for an electron electric dipole moment experiment”, *Phys. Rev. A* **73**, 062108 (2006) (cit. on p. 5).
- [37] T. A. collaboration, J. Baron, W. C. Campbell, D. DeMille, J. M. Doyle, G. Gabrielse, Y. V. Gurevich, P. W. Hess, N. R. Hutzler, E. Kirilov, I. Kozyryev, B. R. O’Leary, C. D. Panda, M. F. Parsons, E. S. Petrik, B. Spaun, A. C. Vutha, and A. D. West, “Order of magnitude smaller limit on the electric dipole moment of the electron”, **343**, 269–272 (2014) (cit. on p. 5).

- [38] B. Gadway and B. Yan, “Strongly interacting ultracold polar molecules”, *J. Phys. B: At. Mol. Opt. Phys.* **49**, 152002 (2016) (cit. on p. 5).
- [39] S. Guo, M. Bajdich, L. Mitas, and P. J. Reynolds, “Study of dipole moments of LiSr and KRb molecules by quantum Monte Carlo methods”, *Mol. Phys.* **111**, 1744–1752 (2013) (cit. on p. 5).
- [40] D. DeMille, “Quantum computation with trapped polar molecules”, *Phys. Rev. Lett.* **88** (2002) (cit. on p. 5).
- [41] W. Phillips and H. Metcalf, “Laser deceleration of an atomic beam”, *Phys. Rev. Lett.* **48**, 596–599 (1982) (cit. on p. 6).
- [42] E. S. Shuman, J. F. Barry, D. R. Glenn, and D. DeMille, “Radiative force from optical cycling on a diatomic molecule”, *Phys. Rev. Lett.* **103** (2009) (cit. on p. 6).
- [43] E. S. Shuman, J. F. Barry, and D. DeMille, “Laser cooling of a diatomic molecule”, *Nature* **467**, 820–823 (2010) (cit. on p. 6).
- [44] N. R. Hutzler, H. Lu, and J. M. Doyle, “The buffer gas beam: an intense, cold, and slow source for atoms and molecules”, *Chem. Rev.* **112**, 4803–4827 (2012) (cit. on pp. 6, 7).
- [45] D. R. Willey, D. N. Bittner, and F. C. De Lucia, “Collisional cooling of the NO-He system. the pressure broadening cross sections between 4.3 and 1.8 K”, *Mol. Phys.* **67**, 455–463 (1989) (cit. on p. 6).
- [46] J. M. Doyle, B. Friedrich, J. Kim, and D. Patterson, “Buffer-gas loading of atoms and molecules into a magnetic trap”, *Phys. Rev. A* **52**, R2515–R2518 (1995) (cit. on p. 6).
- [47] D. Patterson, E. Tsikata, and J. M. Doyle, “Cooling and collisions of large gas phase molecules”, *Phys. Chem. Chem. Phys.* **12**, 9736–9741 (2010) (cit. on p. 6).
- [48] J. Piskorski, D. Patterson, S. Eibenberger, and J. M. Doyle, “Cooling, spectroscopy and non-sticking of trans-stilbene and Nile Red”, *ChemPhysChem.* **15**, 3800–3804 (2014) (cit. on p. 7).

-
- [49] D. H. Levy, “The spectroscopy of very cold gases”, *Science* **214**, 263–269 (1981) (cit. on p. 8).
- [50] S. Y. T. van de Meerakker, H. L. Bethlem, and G. Meijer, “Taming molecular beams”, *Nat. Phys.* **4**, 595–602 (2008) (cit. on p. 8).
- [51] W. Christen and K. Rademann, “Cooling and slowing in high-pressure jet expansions”, *Phys. Rev. A* **77** (2008) (cit. on p. 9).
- [52] H. L. Bethlem, G. Berden, and G. Meijer, “Decelerating neutral dipolar molecules”, *Phys. Rev. Lett.* **83**, 1558–1561 (1999) (cit. on pp. 10, 11, 109).
- [53] N. Vanhaecke, U. Meier, M. Andrist, B. H. Meier, and F. Merkt, “Multistage Zeeman deceleration of hydrogen atoms”, *Phys. Rev. A* **75** (2007) (cit. on pp. 10, 11, 109).
- [54] R. Fulton, A. I. Bishop, M. N. Shneider, and P. F. Barker, “Controlling the motion of cold molecules with deep periodic optical potentials”, *Nat. Phys.* **2**, 465–468 (2006) (cit. on pp. 10, 13).
- [55] H. Kallmann and F. Z. Reiche, “Über den Durchgang bewegter Moleküle durch inhomogene Kraftfelder”, *Physik* **6**, 352–375 (1921) (cit. on p. 10).
- [56] W. Gerlach and O. Z. Stern, “Der experimentelle Nachweis der Richtungsquantelung im Magnetfeld”, *Phys.* **9**, 349–352 (1922) (cit. on p. 10).
- [57] S. Y. T. van de Meerakker, H. L. Bethlem, N. Vanhaecke, and G. Meijer, “Manipulation and control of molecular beams”, *Chem. Rev.* **112**, 4828–4878 (2012) (cit. on p. 11).
- [58] G. E. Chamberlain and J. C. Zorn, “Alkali polarizabilities by the atomic beam electrostatic deflection method”, *Phys. Rev.* **129**, 677 (1963) (cit. on p. 11).
- [59] R. Antoine, P. Dugourd, D. Rayane, E. Benichou, M. Broyer, F. Chandezon, and C. Guet, “On the evaluation of the van der Waals potentials in ionic crystals”, *J. Chem. Phys.* **110** (1999) (cit. on p. 11).
- [60] R. Moro, R. Rabinovitch, C. Xia, and V. V. Kresin, “Electric dipole moments of water clusters from a beam deflection measurement”, *Phys. Rev. Lett.* **97** (2006) (cit. on p. 11).

- [61] F. Filsinger, J. Küpper, G. Meijer, J. L. Hansen, J. Maurer, J. H. Nielsen, L. Holmegaard, and H. Stapelfeldt, “Pure samples of individual conformers: the separation of stereoisomers of complex molecules using electric fields”, *Angew. Chem., Int. Ed.* **48**, 6900 (2009) (cit. on p. 11).
- [62] L. Holmegaard, J. H. Nielsen, I. Nevo, H. Stapelfeldt, F. Filsinger, J. Küpper, and G. Meijer, “Laser-induced alignment and orientation of quantum-state-selected large molecules”, *Phys. Rev. Lett.* **102** (2009) (cit. on p. 11).
- [63] H. L. Bethlem, G. Berden, F. M. H. Crompvoets, R. T. Jongma, A. J. A. van Roij, and G. Meijer, “Electrostatic trapping of ammonia molecules”, *Nature* **406**, 491–494 (2000) (cit. on pp. 11, 15).
- [64] H. L. Bethlem, F. M. H. Crompvoets, R. T. Jongma, S. Y. T. van de Meerakker, and G. Meijer, “Deceleration and trapping of ammonia using time-varying electric fields”, *Phys. Rev. A* **65** (2002) (cit. on p. 11).
- [65] X. Wang, M. Kirste, G. Meijer, and S. Y. T. van de Meerakker, “Stark deceleration of NO radicals”, *ArXiv e-prints* (2013) (cit. on p. 11).
- [66] S. Y. T. van de Meerakker, I. Labazan, S. Hoekstra, J. Küpper, and G. Meijer, “Production and deceleration of a pulsed beam of metastable NH ($a^1\Delta$) radicals”, *Journal of Physics B: Atomic, Molecular and Optical Physics* **39**, S1077 (2006) (cit. on p. 11).
- [67] J. Riedel, S. Hoekstra, W. Jäger, J. J. Gilijamse, S. Y. T. van de Meerakker, and G. Meijer, “Accumulation of stark-decelerated NH molecules in a magnetic trap”, *Eur. Phys. J. D* **65**, 161–166 (2011) (cit. on p. 11).
- [68] J. R. Bochinski, E. R. Hudson, H. J. Lewandowski, G. Meijer, and J. Ye, “Phase space manipulation of cold free radical OH molecules”, *Phys. Rev. Lett.* **91**, 243001 (2003) (cit. on p. 11).
- [69] J. R. Bochinski, E. R. Hudson, H. J. Lewandowski, and J. Ye, “Cold free-radical molecules in the laboratory frame”, *Phys. Rev. A* **70**, 043410 (2004) (cit. on p. 11).
- [70] S. Y. T. van de Meerakker, P. H. M. Smeets, N. Vanhaecke, R. T. Jongma, and G. Meijer, “Deceleration and electrostatic trapping of OH radicals”, *Phys. Rev. Lett.* **94**, 023004 (2005) (cit. on pp. 11, 80).

-
- [71] L. Scharfenberg, H. Haak, G. Meijer, and S. Y. T. van de Meerakker, “Operation of a Stark decelerator with optimum acceptance”, *Phys. Rev. A* **79**, 023410 (2009) (cit. on p. 11).
- [72] M. Kirste, X. Wang, G. Meijer, K. B. Gubbels, G. C. van der Avoird A. Groenenboom, and S. Y. T. van de Meerakker, “Magnetic dipole transitions in the OH $A^2\Sigma^2 \leftarrow X^2\Pi$ system”, *J. Chem. Phys.* **137**, 101102 (2012) (cit. on p. 11).
- [73] S. Hoekstra, J. J. Gilijamse, B. Sartakov, N. Vanhaecke, L. Scharfenberg, S. Y. T. van de Meerakker, and G. Meijer, “Optical pumping of trapped neutral molecules by blackbody radiation”, *Phys. Rev. Lett.* **98**, 133001 (2007) (cit. on p. 11).
- [74] E. R. Hudson, C. Ticknor, B. C. Sawyer, C. A. Taatjes, H. J. Lewandowski, J. R. Bochinski, J. L. Bohn, and J. Ye, “Production of cold formaldehyde molecules for study and control of chemical reaction dynamics with hydroxyl radicals”, *Phys. Rev. A* **73**, 063404 (2006) (cit. on p. 11).
- [75] S. Jung, E. Tiemann, and C. Lisdat, “Cold atoms and molecules from fragmentation of decelerated SO_2 ”, *Phys. Rev. A* **74**, 040701 (2006) (cit. on p. 11).
- [76] S. K. Tokunaga, J. M. Dyne, E. A. Hinds, and M. R. Tarbutt, “Stark deceleration of lithium hydride molecules”, *New J. Phys.* **11**, 055038 (2009) (cit. on p. 11).
- [77] T. E. Wall, S. K. Tokunaga, E. A. Hinds, and M. R. Tarbutt, “Nonadiabatic transitions in a Stark decelerator”, *Phys. Rev. A* **81**, 033414 (2010) (cit. on p. 11).
- [78] N. E. Bulleid, R. J. Hendricks, E. A. Hinds, S. A. Meek, G. Meijer, A. Osterwalder, and M. R. Tarbutt, “Traveling-wave deceleration of heavy polar molecules in low-field-seeking states”, *Phys. Rev. A* **86**, 021404 (2012) (cit. on pp. 11, 13).
- [79] J. E. van den Berg, S. H. Turkesteen, E. B. Prinsen, and S. Hoekstra, “Deceleration and trapping of heavy diatomic molecules using a ring-decelerator”, *Eur. Phys. J. D* **66**, 235 (2012) (cit. on pp. 11, 13).

- [80] A. Osterwalder, S. A. Meek, G. Hammer, H. Haak, and G. Meijer, “Deceleration of neutral molecules in macroscopic traveling traps”, *Phys. Rev. A* **81**, 051401 (2010) (cit. on p. 12).
- [81] M. R. Tarbutt, H. L. Bethlem, J. L. Hudson, V. L. Ryabov, V. A. Ryzhov, B. E. Sauer, G. Meijer, and E. A. Hinds, “Slowing heavy, ground-state molecules using an alternating gradient decelerator”, *Phys. Rev. Lett.* **92**, 173002 (2004) (cit. on p. 13).
- [82] K. Wohlfart, F. Grätz, F. Filsinger, H. Haak, G. Meijer, and J. Küpper, “Alternating-gradient focusing and deceleration of large molecules”, *Phys. Rev. A* **77**, 031404 (2008) (cit. on p. 13).
- [83] K. Wohlfart, F. Filsinger F.and Grätz, J. Küpper, and G. Meijer, “Stark deceleration of OH radicals in low-field-seeking and high-field-seeking quantum states”, *Phys. Rev. A* **78**, 033421 (2008) (cit. on p. 13).
- [84] H. Stapelfeldt, H. Sakai, E. Constant, and P. B. Corkum, “Deflection of neutral molecules using the nonresonant dipole force”, *Phys. Rev. Lett.* **79**, 2787–2790 (1997) (cit. on p. 13).
- [85] B. S. Zhao et al., “Molecular lens of the nonresonant dipole force”, *Phys. Rev. Lett.* **85**, 2705–2708 (2000) (cit. on p. 13).
- [86] R. Fulton, A. I. Bishop, and P. F. Barker, “Optical Stark decelerator for molecules”, *Phys. Rev. Lett.* **93**, 243004 (2004) (cit. on p. 13).
- [87] R. Fulton, A. I. Bishop, M. N. Schneider, and P. F. Barker, “Optical Stark deceleration of nitric oxide and benzene molecules using optical lattices”, *J. Phys. B: At. Mol. Opt. Phys.* **39**, S1097 (2006) (cit. on p. 13).
- [88] D. DeMille, D. R. Glenn, and J. Petricka, “Microwave traps for cold polar molecules”, *Eur. Phys. J. D* **31**, 375–384 (2004) (cit. on pp. 14, 66, 71, 109).
- [89] K. Enomoto and T. Momose, “Microwave Stark decelerator for polar molecules”, *Phys. Rev. A* **72**, 061403 (2005) (cit. on pp. 14, 66, 109).
- [90] H. Odashima, K. Merz S.and Enomoto, M. Schnell, and G. Meijer, “Microwave lens for polar molecules”, *Phys. Rev. Lett.* **104**, 253001 (2010) (cit. on pp. 14, 38, 46, 47, 66, 72, 82, 109, 131).

- [91] S. Merz, C. Brieger, N. Vanhaecke, G. Meijer, and M. Schnell, “Manipulating the motion of polar molecules with microwave radiation”, *Mol. Phys.* **111**, 1855–1864 (2013) (cit. on pp. 14, 29, 38, 47, 66, 72, 82, 131).
- [92] S. Merz, N. Vanhaecke, W. Jäger, M. Schnell, and G. Meijer, “Decelerating molecules with microwave fields”, *Phys. Rev. A* **85**, 063411 (2012) (cit. on pp. 14, 29, 38, 47, 66, 71, 72, 82, 131).
- [93] S. Spieler, W. Zhong, P. Djuricanin, O. Nourbakhsh, I. Gerhardt, K. Enomoto, F. Stienkemeier, and T. Momose, “Microwave lens effect for the $J = 0$ rotational state of CH_3CN ”, *Molecular Physics* **111**, 1823–1834 (2013) (cit. on pp. 14, 67, 82).
- [94] D. P. Dunseith, S. Truppe, R. J. Hendricks, B. E. Sauer, E. A. Hinds, and M. R. Tarbutt, “A high quality, efficiently coupled microwave cavity for trapping cold molecules”, *J. Phys. B* **48** (2015) (cit. on p. 14).
- [95] J. D. Weinstein, R. deCarvalho, T. Guillet, B. Friedrich, and J. M. Doyle, “Magnetic trapping of calcium monohydride molecules at millikelvin temperatures”, *Nature* **395**, 148–150 (1998) (cit. on p. 15).
- [96] W. H. Wing, “Electrostatic trapping of neutral atomic particles”, *Phys. Rev. Lett.* **45**, 631–634 (1980) (cit. on p. 15).
- [97] J. van Veldhoven, H. L. Bethlem, M. Schnell, and G. Meijer, “Versatile electrostatic trap”, *Phys. Rev. A* **73** (2006) (cit. on p. 15).
- [98] F. M. H. Cromptoets, H. L. Bethlem, R. T. Jongma, and G. Meijer, “A prototype storage ring for neutral molecules”, *Nature* **441**, 174–176 (2001) (cit. on p. 15).
- [99] F. M. H. Cromptoets, H. L. Bethlem, J. Küpper, A. J. A. van Roij, and G. Meijer, “Dynamics of neutral molecules stored in a ring”, *Phys. Rev. A* **69** (2004) (cit. on p. 15).
- [100] P. C. Zieger, S. Y. T. van de Meerakker, C. E. Heiner, H. L. Bethlem, A. J. A. van Roij, and G. Meijer, “Multiple packets of neutral molecules revolving for over a mile”, *Phys. Rev. Lett.* **105**, 173001 (2010) (cit. on p. 15).

- [101] M. Kirste, B. G. Sartakov, M. Schnell, and G. Meijer, “Nonadiabatic transitions in electrostatically trapped ammonia molecules”, *Phys. Rev. A* **79** (2009) (cit. on p. 15).
- [102] D. E. Pritchard, “Cooling neutral atoms in a magnetic trap for precision spectroscopy”, *Phys. Rev. Lett.* **51**, 1336–1339 (1983) (cit. on p. 16).
- [103] J. van Veldhoven, H. L. Bethlem, and G. Meijer, “ac electric trap for ground-state molecules”, *Phys. Rev. Lett.* **94** (2005) (cit. on p. 16).
- [104] S. K. Tokunaga, W. Skomorowski, P. S. Żuchowski, R. Moszynski, J. M. Hutson, E. A. Hinds, and M. R. Tarbutt, “Prospects for sympathetic cooling of molecules in electrostatic, ac and microwave traps”, *Eur. Phys. J. D* **65**, 141–149 (2011) (cit. on pp. 16, 82).
- [105] A. Prehn, M. Ibrügger, R. Glockner, G. Rempe, and M. Zeppenfeld, “Opto-electrical cooling of polar molecules to submillikelvin temperatures”, *Phys. Rev. Lett.* **116** (2016) (cit. on pp. 16, 82).
- [106] M. Born and R. Oppenheimer, “Zur Quantentheorie der Molekeln”, *Ann. Phys.* **389**, 457–484 (1927) (cit. on p. 17).
- [107] R. N. Zare, *Angular momentum: understanding spatial aspects in chemistry and physics* (John Wiley and Sons, New York, 1988) (cit. on p. 20).
- [108] A. R. Edmonds, *Angular momentum in quantum mechanics* (Princeton University Press, Princeton, 1996) (cit. on p. 20).
- [109] A. Bauder, *Handbook of high-resolution spectroscopy, Fundamentals of rotational spectroscopy*, edited by M. Quack and F. Merkt, Vol. 1 (John Wiley and Sons, New York, 2011), pp. 57–116 (cit. on p. 22).
- [110] G. W. King, R. M. Hainer, and P. C. Cross, “The asymmetric rotor i. calculation and symmetry classification of energy levels”, *J. Chem. Phys.* **11**, 27–42 (1943) (cit. on p. 23).
- [111] W. Gordy and R. L. Cook, *Microwave molecular spectra* (John Wiley and Sons, New York, 1984) (cit. on pp. 25, 36, 68).
- [112] J. K. G. Watson, “Determination of centrifugal distortion coefficients of asymmetric top molecules”, *J. Chem. Phys.* **46** (1967) (cit. on p. 26).

- [113] J. K. G. Watson, "Simplification of the molecular vibration-rotation Hamiltonian", *Mol. Phys.* **15** (1968) (cit. on p. 26).
- [114] J. K. G. Watson, *Vibrational spectra and structure*, edited by J. R. Durig, Vol. 6 (Marcel Dekker, 1977) Chap. 1 (cit. on p. 26).
- [115] H. B. G. Casimir, *Physica* **2** (1935) (cit. on p. 26).
- [116] D. K. Coles and G. W. E., "Stark and Zeeman effects in the inversion spectrum of ammonia", *Phys. Rev.* **70** (1946) (cit. on p. 26).
- [117] J. K. Bragg, "The interaction of the nuclear electric quadrupole moments with molecular rotation in asymmetric-top molecules. I", *Phys. Rev.* **74**, 533 (1948) (cit. on p. 26).
- [118] J. K. Bragg and S. Golden, "The interaction of the nuclear electric quadrupole moments with molecular rotation in asymmetric-top molecules. II. Approximate methods for first order coupling", *Phys. Rev.* **75**, 735 (1949) (cit. on p. 26).
- [119] C. M. Western, *PGOPHER, a program for simulating rotational structure*, <http://pgopher.chm.bris.ac.uk>. (cit. on pp. 28, 59, 68, 78, 89, 112, 132).
- [120] H. L. Bethlem, "Deceleration and trapping of polar molecules using time-varying electric fields", Ph.D. Thesis (Radboud Universiteit Nijmegen, 2002) (cit. on p. 34).
- [121] C. H. Townes and A. L. Schawlow, *Microwave spectroscopy* (Dover Publications, Inc., Mineola, New York, 1975) (cit. on pp. 35, 37, 38, 68).
- [122] S. R. Gandhi and R. B. Bernstein, "Focusing and state selection of NH₃ and OCS by the electrostatic hexapole via first and second-order Stark effects", *J. Chem. Phys.* **87**, 6457 (1987) (cit. on p. 35).
- [123] S. C. Wang, "On the asymmetrical top in quantum mechanics", *Phys. Rev.* **34**, 243 (1929) (cit. on p. 36).

- [124] Y. P. Chang, F. Filsinger, B. G. Sartakov, and J. Küpper, “CMISTARK: Python package for the Stark-effect calculation and symmetry classification of linear, symmetric and asymmetric top wavefunctions in dc electric fields”, *Comput. Phys. Commun.* **185**, 339–349 (2014) (cit. on p. 36).
- [125] J. D. Jackson, *Classical electrodynamics*, 3rd (John Wiley and Sons, New York, 1962) (cit. on pp. 38, 43).
- [126] W. Greiner, *Classical electrodynamics* (Springer, New York, 1998) (cit. on p. 38).
- [127] C. Cohen-Tannoudji, J. Dupont-Roc, and G. Grynberg, *Atom-photon interactions: Basic processes and applications* (Wiley-VCH, Weinheim, 2004) (cit. on pp. 45, 67).
- [128] H. J. Metcalf and P. van der Straten, *Laser cooling and trapping* (Springer, Berlin, 2002) (cit. on pp. 45, 67).
- [129] M. N. R. Ashfold, R. N. Dixon, N. Little, R. J. Stickland, and C. M. Western, “The \tilde{B}^1E' state of ammonia: Sub-Doppler spectroscopy at vacuum ultraviolet energies”, *J. Chem. Phys.* **89**, 1754–1761 (1988) (cit. on p. 48).
- [130] W. C. Wiley and I. H. McLaren, “Time-of-flight mass spectrometer with improved resolution”, *Rev. Sci. Instrum.* **26**, 1150–1157 (1955) (cit. on p. 48).
- [131] E. M. Gibson, A. C. Jones, A. G. Taylor, W. G. Bouwman, D. Phillips, and J. Sandell, “Laser-induced fluorescence spectroscopy of 4-aminobenzonitrile, 4-(N,N-dimethylamino)benzonitrile, and their van der Waals complexes in a supersonic jet”, *J. Phys. Chem.* (1988) (cit. on p. 50).
- [132] H. Yu, E. Joslin, B. Crystall, T. Smith, W. Sinclair, and D. Phillips, “Spectroscopy and dynamics of jet-cooled 4-aminobenzonitrile (4-ABN)”, *J. Phys. Chem.* **97**, 8146–8151 (1993) (cit. on p. 50).
- [133] G. Varsányi and L. Láng, *Assignments for vibrational spectra of seven hundred benzene derivatives* (Wiley, New York, 1974) (cit. on p. 50).
- [134] T. Betz, S. Zinn, J. B. Graneek, and M. Schnell, “Nuclear quadrupole coupling constants of two chemically distinct nitrogen atoms in 4-aminobenzonitrile”, *J. Phys. Chem. A* **118**, 5164–5169 (2014) (cit. on pp. 50, 56, 58, 60, 62).

- [135] A. L. Steber, B. J. Harris, J. L. Neill, and B. H. Pate, “An arbitrary waveform generator based chirped pulse Fourier transform spectrometer operating from 260 to 295GHz”, *J. Mol. Spectrosc.* **280**, 3–10 (2012) (cit. on p. 51).
- [136] J. L. Alonso, C. Pérez, M. Eugenia Sanz, J. C. Lopez, and S. Blanco, “Seven conformers of l-threonine in the gas phase: a LA-MB-FTMW study”, *Phys. Chem. Chem. Phys.* **11**, 617–627 (2009) (cit. on p. 53).
- [137] C. Pérez, M. T. Muckle, D. P. Zaleski, N. A. Seifert, B. Temelso, G. C. Shields, Z. Kisiel, and B. H. Pate, “Structures of cage, prism, and book isomers of water hexamer from broadband rotational spectroscopy”, *Science* **336**, 897–901 (2012) (cit. on p. 53).
- [138] J. K. G. Watson, A. Roytburg, and W. Ulrich, “Least-squares mass-dependence molecular structures”, *J. Mol. Spectrosc.* **196** (1999) (cit. on pp. 54, 99, 123).
- [139] D. R. Borst, T. M. Korter, and D. W. Pratt, “On the additivity of bond dipole moments. Stark effect studies of the rotationally resolved electronic spectra of aniline, benzonitrile, and aminobenzonitrile”, *Chem. Phys. Lett.* **350**, 485–490 (2001) (cit. on pp. 55, 59, 60, 81).
- [140] M. J. Frisch, G. W. Trucks, H. B. Schlegel, G. E. Scuseria, M. A. Robb, J. R. Cheeseman, G. Scalmani, V. Barone, B. Mennucci, G. A. Petersson, H. Nakatsuji, M. Caricato, X. Li, H. P. Hratchian, A. F. Izmaylov, J. Bloino, G. Zheng, J. L. Sonnenberg, M. Hada, M. Ehara, K. Toyota, R. Fukuda, J. Hasegawa, M. Ishida, T. Nakajima, Y. Honda, O. Kitao, H. Nakai, T. Vreven, J. A. Montgomery, J. E. Peralta, F. Ogliaro, M. Bearpark, J. J. Heyd, E. Brothers, K. N. Kudin, V. N. Staroverov, R. Kobayashi, J. Normand, K. Raghavachari, A. Rendell, J. C. Burant, S. S. Iyengar, J. Tomasi, M. Cossi, N. Rega, J. M. Millam, M. Klene, J. E. Knox, J. B. Cross, V. Bakken, C. Adamo, J. Jaramillo, R. Gomperts, R. E. Stratmann, O. Yazyev, A. J. Austin, R. Cammi, C. Pomelli, J. W. Ochterski, R. L. Martin, K. Morokuma, V. G. Zakrzewski, G. A. Voth, P. Salvador, J. J. Dannenberg, S. Dapprich, A. D. Daniels, Farkas, J. B. Foresman, J. V. Ortiz, J. Cioslowski, and D. J. Fox, *Gaussian 09*, Wallingford CT, 2009 (cit. on pp. 58, 89).

- [141] G. Berden, J. van Rooy, W. L. Meerts, and K. A. Zachariasse, “Rotationally resolved electronic spectroscopy of 4-aminobenzonitrile”, *Chem. Phys. Lett.* **278**, 373–379 (1997) (cit. on pp. 59, 60).
- [142] D. G. Lister and J. K. Tyler, “The microwave spectrum, structure and dipole moment of aniline”, *J. Mol. Struct.* **23**, 253–264 (1974) (cit. on pp. 59, 60).
- [143] B. Kleibömer and D. H. Sutter, “The vibrational state dependence of the ^{14}N quadrupole coupling tensor in aniline. A microwave Fourier-transform study combined with semirigid bender calculations.”, *Z. Naturforsch.* **43a**, 561–571 (1988) (cit. on p. 59).
- [144] M. Quack and M. Stockburger, “Resonance fluorescence of aniline vapour”, *J. Mol. Spectrosc.* **43**, 87–116 (1972) (cit. on p. 59).
- [145] A. Heine, R. Herbst-Irmer, and D. Stalke, “Structure and crystal packing of 4-aminobenzonitrile and 4-amino-3,5-dimethylbenzonitriles at various temperatures”, *Acta Cryst.* **B50**, 363–373 (1994) (cit. on pp. 59, 81).
- [146] H. M. Foley, “Note on the nuclear electric quadrupole spectrum of a homonuclear diatomic molecule in a magnetic field”, *Phys. Rev.* **71**, 747–751 (1947) (cit. on pp. 61, 115).
- [147] R. G. Bird, J. L. Neill, V. J. Alstadt, J. W. Young, B. H. Pate, and D. W. Pratt, “Ground state ^{14}N quadrupole couplings in the microwave spectra of N,N'-dimethylaniline and 4,4'-dimethylaminobenzonitrile”, *J. Phys. Chem. A* **115**, 9392–9398 (2011) (cit. on p. 63).
- [148] K. Wohlfart, M. Schnell, J. U. Grabow, and J. Küpper, “Precise dipole moment and quadrupole coupling constants of benzonitrile”, *J. Mol. Spectrosc.* **247**, 119–121 (2008) (cit. on p. 63).
- [149] Z. Kisiel, *PROSPE. programs for rotational spectroscopy*, <http://info.ifpan.edu.pl/~kisiel/prospe.htm> (cit. on pp. 64, 92, 98, 120, 123).
- [150] D. Patterson, “Decelerating and trapping large polar molecules”, *ChemPhysChem.* **17**, 3790–3794 (2016) (cit. on pp. 77, 78, 80, 108).

- [151] S. Cupp, C. Y. Lee, D. McWhorter, and B. H. Pate, “Doorway state enhanced intramolecular vibrational energy redistribution in the asymmetric $=\text{CH}_2$ hydride stretch of methyl vinyl ether”, *J. Chem. Phys.* **109**, 4302–4315 (1998) (cit. on p. 77).
- [152] J. C. Keske and B. H. Pate, “Decoding the dynamical information embedded in highly mixed quantum states”, *Annu. Rev. Phys. Chem.* **51**, 323–353 (2000) (cit. on p. 77).
- [153] J. Lim, M. D. Frye, J. M. Hutson, and M. R. Tarbutt, “Modeling sympathetic cooling of molecules by ultracold atoms”, *Phys. Rev. A* **92**, 053419 (2015) (cit. on p. 82).
- [154] M. Muniz-Miranda and N. Neto, “Surface-enhanced Raman scattering of π -conjugated “push–pull” molecules: Part I. p-nitroaniline adsorbed on silver nanoparticles”, *Colloids Surf. A* **249**, 79–84 (2004) (cit. on p. 85).
- [155] M. Muniz-Miranda, “SERS investigation on the adsorption and photoreaction of 4-nitroanisole in Ag hydrosols”, *J. Raman Spectrosc.* **44**, 1416–1421 (2013) (cit. on pp. 85, 100).
- [156] D. M. Burland, R. D. Miller, and C. A. Walsh, “Second-order nonlinearity in poled-polymer systems”, *Chem. Rev.* **94**, 1 (1994) (cit. on p. 85).
- [157] N. P. Prasad and D. J. Williams, *Introduction to nonlinear optical effects in molecules and polymers* (Wiley, New York, 1991) (cit. on p. 85).
- [158] J. B. Graneek, S. Merz, D. Patterson, T. Betz, and M. Schnell, “Simulating spatial microwave manipulation of polyatomic asymmetric-top molecules using a multi-level approach”, *ChemPhysChem.* **17**, 3624–3630 (2016) (cit. on pp. 85, 108).
- [159] W. E. Steinmetz, “The application of low-resolution microwave spectroscopy to conformational analysis”, *J. Am. Chem. Soc.* **96**, 685–692 (1974) (cit. on p. 86).
- [160] S. Zinn, T. Betz, C. Medcraft, and M. Schnell, “Structure determination of trans-cinnamaldehyde by broadband microwave spectroscopy”, *Phys. Chem. Chem. Phys.* **17** (2015) (cit. on pp. 86, 98, 110).

- [161] S. R. Domingos, C. Pérez, and M. Schnell, “Communication: Structural locking mediated by a water wire: A high-resolution rotational spectroscopy study on hydrated forms of a chiral biphenyl derivative”, *J. Chem. Phys.* **145** (2016) (cit. on p. 86).
- [162] J. H. Høg, L. Nygaard, and G. O. Sørensen, “Microwave spectrum and planarity of nitrobenzene”, *J. Mol. Structure* **7**, 111–121 (1970) (cit. on pp. 86, 92, 98, 99).
- [163] O. V. Dorofeeva et al., “Molecular structure and conformation of nitrobenzene reinvestigated by combined analysis of gas-phase electron diffraction, rotational constants, and theoretical calculations”, *Struct. Chem.* **18**, 739–753 (2007) (cit. on p. 86).
- [164] M. Onda, A. Toda, S. Mori, and I. Yamaguchi, “Microwave spectrum of anisole”, *J. Mol. Spectrosc.* **144**, 47–51 (1986) (cit. on p. 86).
- [165] D. Schmitz, A. Shubert, T. Betz, and M. Schnell, “Multi-resonance effects within a single chirp in broadband rotational spectroscopy: The rapid adiabatic passage regime for benzonitrile”, *J. Mol. Spectrosc.* **280**, 77–84 (2012) (cit. on pp. 89, 102).
- [166] N. Heineking and H. Dreizler, “Nitrogen quadrupole coupling constants of nitrobenzene and o-nitrophenol”, *Ber. Bunsenges. Phys. Chem.* **97** (1993) (cit. on p. 90).
- [167] O. Desyatnyk, L. Pszczólkowski, S. Thorwirth, T. M. Krygowski, and Z. Kisiel, “The rotational spectra, electric dipole moments and molecular structures of anisole and benzaldehyde”, *Phys. Chem. Chem. Phys.* **7** (2005) (cit. on pp. 92, 98, 121).
- [168] D. J. Millen and J. R. Morton, “The microwave spectrum of nitric acid”, *J. Chem. Soc.*, 1523–1528 (1960) (cit. on pp. 96, 97, 122).
- [169] A. P. Cox and S. Waring, “Microwave spectrum and structure of nitromethane”, *J. Chem. Soc., Faraday Trans. 2* **68**, 1060–1071 (1972) (cit. on pp. 97, 98, 122, 127).

- [170] A. Domenicano, G. Schultz, I. Hargittai, M. Colapietro, G. Portalone, P. George, and C. W. Bock, "Molecular structure of nitrobenzene in the planar and orthogonal conformations a concerted study by electron diffraction, X-ray crystallography, and molecular orbital calculations", *Struct. Chem.* **1**, 107–122 (1990) (cit. on pp. 98, 99).
- [171] J. H. Høg, "A study of nitrobenzene", Ph.D. Thesis (University of Copenhagen, 1971) (cit. on pp. 98, 99).
- [172] T. Oka, "High-power microwave double-resonance experiments", *Can. J. Phys.* **47**, 2343–2350 (1969) (cit. on p. 100).
- [173] F. Wodarczyk and E. Wilson, "Radio frequency-microwave double resonance as a tool in the analysis of microwave spectra", *J. Mol. Spectrosc.* **37**, 445–463 (1971) (cit. on p. 100).
- [174] B. Vogelsanger, M. Andrist, and A. Bauder, "Two-dimensional correlation experiments in microwave Fourier transform spectroscopy", *Chem. Phys. Lett.* **144**, 180–186 (1988) (cit. on p. 100).
- [175] B. Vogelsanger and A. Bauder, "Two-dimensional microwave Fourier transform spectroscopy", *J. Chem. Phys.* **92**, 4101–4114 (1990) (cit. on p. 100).
- [176] U. Wötzel, W. Stahl, and H. Mäder, "The influence of an off-resonant pump radiation in Fourier transform microwave spectroscopy", *Can. J. Phys.* **75**, 821–830 (1997) (cit. on p. 100).
- [177] D. Schmitz, A. V. Shubert, D. Patterson, A. Krin, and M. Schnell, "Phase dependence of double-resonance experiments in rotational spectroscopy", *J. Phys. Chem. Lett.* **6**, 1493–1498 (2015) (cit. on p. 100).
- [178] J. C. McGurk, T. G. Schmalz, and W. H. Flygare, "Fast passage in rotational spectroscopy: Theory and experiment", *J. Chem. Phys.* **60**, 4181–4188 (1974) (cit. on pp. 101, 105).
- [179] J. C. McGurk, T. G. Schmalz, and W. H. Flygare, *A density matrix, Bloch equation description of infrared and microwave transient phenomena* (John Wiley and Sons, Inc., 1974) (cit. on p. 101).

- [180] J. L. Neill, S. T. Shipman, L. Alvarez-Valtierra, A. Lesarri, Z. Kisiel, and B. H. Pate, “Rotational spectroscopy of iodobenzene and iodobenzene–neon with a direct digital 2–8 GHz chirped-pulse Fourier transform microwave spectrometer”, *J. Mol. Spec.* **269**, 21–29 (2011) (cit. on p. 102).
- [181] J. S. Melinger, S. R. Gandhi, A. Hariharan, J. X. Tull, and W. S. Warren, “Generation of narrowband inversion with broadband laser pulses”, *Phys. Rev. Lett.* **68**, 2000–2003 (1992) (cit. on p. 104).
- [182] J. S. Melinger, S. R. Gandhi, A. Hariharan, D. Goswami, and W. S. Warren, “Adiabatic population transfer with frequency-swept laser pulses”, *J. Chem. Phys.* **101**, 6439–6454 (1994) (cit. on p. 104).
- [183] J. Grabow, *Handbook of high-resolution spectroscopy, Fourier transform microwave spectroscopy measurement and instrumentation*, edited by M. Quack and F. Merkt, Vol. 2 (John Wiley and Sons, New York, 2011), pp. 723–801 (cit. on p. 105).
- [184] J. Raap, S. Nieuwenhuis, A. Creemers, S. Hexspoor, U. Kragl, and J. Lugtenburg, “Synthesis of isotopically labelled l-phenylalanine and l-tyrosine”, *Eur. J. Org. Chem.* **10**, 2609–2621 (1999) (cit. on p. 109).
- [185] D. Dini, F. Decker, F. Andreani, E. Salatelli, and P. Hapiot, “A comparative study of isomeric polydialkylterthiophenes with regular regiochemistry of substitution. Electrochemical synthesis”, *Polymer* **41**, 6473–6480 (2000) (cit. on p. 109).
- [186] V. Krishnakumar, G. Keresztury, T. Sundius, and R. Ramasamy, “Simulation of IR and Raman spectra based on scaled DFT force fields: a case study of 2-(methylthio)benzotrile, with emphasis on band assignment”, *J. Mol. Struct.* **702**, 9–21 (2004) (cit. on p. 109).
- [187] Y. Sert and F. Ucun, “Vibrational spectroscopic investigation of p-, m- and o-nitrobenzotrile by using Hartree-Fock and density functional theory”, *Indian J. Phys.* **87**, 809–818 (2013) (cit. on p. 109).

- [188] S. R. Domingos, C. Pérez, C. Medcraft, P. Pinacho, and M. Schnell, “Flexibility unleashed in acyclic monoterpenes: Conformational space of citronellal revealed by broadband rotational spectroscopy”, *Phys. Chem. Chem. Phys.* **18** (2016) (cit. on p. 110).
- [189] J. B. Graneek, C. Pérez, and M. Schnell, “Structural determination and population transfer of 4-nitroanisole by broadband microwave spectroscopy and tailored microwave pulses”, *J. Chem. Phys.* **147**, 154306 (2017) (cit. on pp. 110, 122, 123, 127).
- [190] T. Higashi and K. Osaki, “p-Nitrobenzotrile”, *Acta Cryst.* **33**, 2337–2339 (1977) (cit. on pp. 110, 127).
- [191] T. Oka, “On negative inertial defect”, *J. Mol. Struct.* **352-353**, 225–233 (1995) (cit. on p. 121).
- [192] J. Demaison and H. D. Rudolph, “When is the substitution structure not reliable?”, *J. Mol. Spectrosc.* **215**, 78–84 (2002) (cit. on p. 121).
- [193] A. C. Legon and D. J. Millen, “The microwave spectrum, structure, and dipole moment of nitril fluoride”, *J. Chem. Soc. A* **0**, 1736–1740 (1968) (cit. on p. 122).
- [194] M. I. Kay and B. C. Frazer, “A neutron diffraction study of the low temperature phase of NaNO_2 ”, *Acta Cryst.* **14**, 56–57 (1961) (cit. on p. 122).
- [195] D. S. Tikhonov, D. I. Sharapa, A. A. Otlyotov, P. M. Solyankin, A. N. Rykov, A. P. Shkurinov, O. E. Grikina, and L. S. Khaikin, “Nitroxoline molecule: planar or not? A story of battle between $\pi - \pi$ conjugation and interatomic repulsion”, *J. Phys. Chem. A* (2018) (cit. on p. 123).

Appendix

Hazardous substances according to the Global Harmonised System (GHS) within the EU:

Substance	Hazard statement(s)	Precautionary statement(s)	Pictogram
Ammonia (NH ₃)	221-280-314-331-410	210-280-304+340+310-305+351+338-377-403	
4-Aminobenzonitrile (C ₆ H ₄ NH ₂ CN)	301-319	301+310-305+351+338	
4-Nitroanisole (C ₆ H ₄ OCH ₃ NO ₂)	R52/53 S61
2-Nitrobenzonitrile (C ₆ H ₄ NO ₂ CN)	302-332	...	
3-Nitrobenzonitrile (C ₆ H ₄ NO ₂ CN)	302+312+332	280	
DCM	228-315-319-332-335	210-261-305+351+338	
Pyromethene 597
Ethanol (C ₂ H ₅ OH)	225	210	

Acknowledgements

I've spent a total of five years working on my PhD in Melanie Schnell's CoCoMol (now: FS-SMP) group and have seen many people come and go in this time. I would like to thank each and every one of them for making this experience as enjoyable as it was. The biggest thanks have to go to Melanie Schnell, not just for giving me this amazing opportunity, but also for the patience and understanding she has shown me throughout this period, especially considering the practical challenges that arose. Thank you to Prof. Weller for co-supervising my PhD project and to the Universität Hamburg for accepting my admission.

Another big thank you to Simon Merz, whose knowledge of the set-up for the motion manipulation experiment and the field of cold molecules in general proved invaluable. Working closely with Simon in the lab meant I learnt a lot on the subject of cold molecules, and also a lot of useless information of questionable factuality, all of which added to a great working environment. I would also like to thank Thomas Betz and David Patterson for fruitful discussions related to the development of the code for the AC-Stark calculations. Thomas in particular helped me transform from a Matlab rookie into a Matlab pro. The mechanical workshop at DESY also deserves a very big thank you. Without the work they did on polishing the steel rods of the Stark decelerator, the Stark decelerator would most likely still be out-of-order.

When working with the COMPACT spectrometer, there were a few members of the group that were particularly helpful in introducing me to the technique. Anna Krin, Mariyam Fatima and Cristóbal Pérez deserve thanks for this reason, owing to their instruction I was able to work confidently with the spectrometer. Cristóbal's expertise was also especially helpful when designing the double-resonance experiments. I'd also like to thank both Ben Arenas and Mariyam Fatima (again)

for proof reading my dissertation, and Sabrina Zinn for help in translating my abstract.

In addition to the people that contributed directly to the work I was doing throughout my PhD, there are those that have not yet been thanked who contributed more to my overall experience. Sérgio Domingos for his sci-fi and footy banter. Sabrina Zinn (again) and Chris Medcraft for improving my alcohol tolerance. David Schmitz for being my kicker partner, I still haven't found a better replacement. Sebastien Gruet for improving my already fluent french, and Alvin Schubert and Amanda Steber for the good-natured American-British rivalry.

Next thanks go to the coolest gang alive. This group of friends helped distract me from all things related to my PhD and also provided moral support in times of frustration. My family have also been incredibly supportive throughout this time, I'll make sure they get personal copies of this thesis, I'm sure they'll appreciate it. Last, but never least, a big thank you to Jenna. I really couldn't have done any of this without you and I'll always appreciate everything you've done to make this possible. Because of this I would like to dedicate this work to Jenna, it's also a pretty romantic thing to do.

Declaration

I hereby declare on oath, that this thesis is my original work and it has been written by me in its entirety. I have duly acknowledged all the sources of information which have been used in the thesis.

Hamburg, August 1, 2018

Signature: